Journal of Computational Physics 228 (2009) 8481–8524

Contents lists available at ScienceDirect

Journal of Computational Physics

journal homepage: www.elsevier.com/locate/jcp

Very-high-order WENO schemes

G.A. Gerolymos *, D. Sénéchal, I. Vallet

Institut d'Alembert, Case 161, Université Pierre et Marie Curie (UPMC), 4 place Jussieu, 75005 Paris, France

ARTICLE INFO

Article history:
Received 12 January 2009
Received in revised form 2 July 2009
Accepted 11 July 2009
Available online 24 September 2009

Keywords:
High-order schemes
WENO schemes
Smoothness indicators
Euler equations
Hyperbolic conservation laws

ABSTRACT

We study WENO$(2r-1)$ reconstruction [D.S. Balsara, C.W. Shu, Monotonicity prserving WENO schemes with increasingly high-order of accuracy, J. Comput. Phys. 160 (2000) 405–452], with the mapping (WENOM) procedure of the nonlinear weights [A.K. Henrick, T.D. Aslam, J.M. Powers, Mapped weighted-essentially-non-oscillatory schemes: achieving optimal order near critical points, J. Comput. Phys. 207 (2005) 542–567], which we extend up to WENO17 ($r=9$). We find by numerical experiment that these procedures are essentially nonoscillatory without any stringent CFL limitation ($\text{CFL} \in [0.8, 1]$), for scalar hyperbolic problems (both linear and scalar conservation laws), provided that the exponent p_β in the definition of the Jiang–Shu [G.S. Jiang, C.W. Shu, Efficient implementation of weighted ENO schemes, J. Comput. Phys. 126 (1996) 202–228] nonlinear weights be taken as $p_\beta = r$, as originally proposed by Liu et al. [X.D. Liu, S. Osher, T. Chan, Weighted essentially nonoscillatory schemes, J. Comput. Phys. 115 (1994) 200–212], instead of $p_\beta = 2$ (this is valid both for WENO and WENOM reconstructions), although the optimal value of the exponent is probably $p_\beta(r) \in [2, r]$. Then, we apply the family of very-high-order WENOM$_{p_\beta=r}$ reconstructions to the Euler equations of gasdynamics, by combining local characteristic decomposition [A. Harten, B. Engquist, S. Osher, S.R. Chakravarthy, Uniformly high-order accurate essentially nonoscillatory schemes III, J. Comput. Phys. 71 (1987) 231–303], with recursive-order-reduction (ROR) aiming at aleviating the problems induced by the nonlinear interactions of characteristic fields within the stencil. The proposed ROR algorithm, which generalizes the algorithm of Titarev and Toro [V.A. Titarev, E.F. Toro, Finite-volume WENO schemes for 3-D conservation laws, J. Comput. Phys. 201 (2004) 238–260], is free of adjustable parameters, and the corresponding RORWENOM$_{p_\beta=r}$ schemes are essentially nonoscillatory, as $\Delta x \to 0$, up to $r=9$, for all of the test-cases studied. Finally, the unsplit linewise 2-D extension of the schemes is evaluated for several test-cases.

1. Introduction

The WENO$(2r-1)$ (weighted essentially nonoscillatory $(2r-1)$-order) reconstruction procedure introduced by Liu et al. [1], and further developed by Jiang and Shu [2], has become the method of choice in high-resolution/high-order methods for the computation of hyperbolic systems of conservation laws [3–7]. They are widely used for the direct numerical simulation (DNS) of compressible flows containing shock-waves [8–11].

Liu et al. [1] put forward the idea of replacing the choice of the smoothest possible stencil of the ENO schemes [12] by a convex combination of the reconstructions on all stencils, using nonlinear weights designed to achieve the highest possible order-of-accuracy in smooth regions, and to weight out nonsmooth stencils in regions containing discontinuities, and studied WENO schemes for $r=2$ (WENO3) and for $r=3$ (WENO5). Jiang and Shu [2] introduced an improved definition of the

* Corresponding author. Tel.: +33 1 44 27 23 74.
E-mail addresses: georges.gerolymos@upmc.fr (G.A. Gerolymos), isabelle.vallet@upmc.fr (I. Vallet).

0021-9991/$ - see front matter
doi:10.1016/j.jcp.2009.07.039

smoothness indicators, used to evaluate the nonlinear weights, and further studied the WENO3 and WENO5 schemes. Balsara and Shu [3] extended the WENO family up to $r = 6$ (WENO11). However, the WENO5 scheme is the most widely used [4,13,10,11], with the WENO7 scheme being also used [5], e.g. in compressible DNS studies [9,10]. Recently, Henrick et al. [4] have presented a thorough study of the WENO5 scheme, and have in particular introduced a mapping procedure which aims at maintaining the nonlinear weights of the WENO convex combination of stencils as near as possible to the optimal weights, except at highly nonsmooth regions. This is achieved through a mapping function, and can be easily applied to WENO$(2r-1)$ schemes of arbitrary order, resulting in the WENOM$(2r-1)$ schemes. Even more recently, Borges et al. [7], exploited the structure of the Taylor-expansions of the smoothness indicators of the WENO5 scheme to develop improved nonlinear weights, which obtain the increased accuracy of the WENOM5 procedure directly (without mapping).

Balsara and Shu [3] have also examined the possibility of using the monotonicity-preserving (MP) procedure of Suresh and Huynh [14], coupled with the UW schemes (central WENO schemes or WENO schemes with optimal weights). They named these schemes MPWENOs, but MPUW is probably a more precise term, since the nonlinear mechanism does not operate through a redefinition of the weights of the r stencils used in the construction of the WENO$(2r-1)$ scheme, but rather as a curvature-based correction (if necessary) of the UW scheme. Working schemes, up to MPWENO11, were constructed in this way [3], but these schemes do not, in general, preserve the order of the underlying UW scheme (often being limited to only $O(\Delta x^4)$ or $O(\Delta x^3)$), while they require somewhat smaller time-steps than the corresponding WENO schemes. In this respect, Balsara and Shu [3] state that they "*therefore see that the monotonicity-preserving bounds do not live up to the full extent of the claim made in Suresh and Huynh* [14] *that they do not damage the order property of smooth solutions at all*".

It seems that, with the present state-of-the-art, the relatively computationally expensive WENO(M) procedure is the price to pay for combining high-order with monotonicity. Notice however, that the use of hermitian WENO (HWENO) schemes [15–18] is an interesting possibility for maintaining high-order with reduced stencils, at the price, however, of resolving supplementary equations for the spatial derivatives of the variables in the context of derivative Riemann solvers [19–21].

The purpose of the present work is to further develop and investigate very-high-order WENO schemes for the computation of hyperbolic conservation laws. In Section 2, we extend the family of progressively higher-order WENO$(2r-1)$ schemes [2,3] up to $r = 9$, and tabulate the coefficients of the WENO13 ($r = 7$), WENO15 ($r = 8$), WENO17 ($r = 9$) scalar reconstructions (Tables 1–6). We also give the Taylor-expansions of the smootheness indicators, up to $r = 9$, demonstrating that they satisfy the sufficient [1–4,7] conditions for the schemes to be $O(\Delta x^{2r-1})$ accurate at smooth regular points ($f'(x_i) \neq 0$). In Section 3, we apply the WENO$(2r-1)$ and WENOM$(2r-1)$ (with the mapping procedure of Henrick et al. [4]) schemes, to the linear advection equation. Numerical experiments indicate that, as r increases, the exponent p_β in the definition of the Jiang–Shu [2] nonlinear weights, must be increased, from the recommended value of $p_\beta = 2$ [2], to ensure ENO (essentially nonoscillatory) behaviour. Without seeking the optimal (lowest) value of p_β, we find that $p_\beta = r$ [1] is sufficient. Standard test-cases [2,4] for the advection equation are computed to study the order-of-accuracy, rate-of-convergence, and ENO behaviour of the WENO$(2r-1)$ and WENOM$(2r-1)$ reconstructions (for $p_\beta = 2$ and for $p_\beta = r$). In Section 4, we apply the scalar WENOM$(2r-1)$ reconstruction to a standard problem [22,23,1] for the Burgers equation, and verify that the results obtained for the linear advection equation carry on to the nonlinear scalar conservation law case, as well. In Section 5, we study the extension of the scalar WENOM$(2r-1)$ reconstructions to the 1-D Euler equations of gasdynamics (system of nonlinear hyperbolic conservation laws), by combining local characteristic reconstruction [12] with a new algorithm for recursive-order-reduction (ROR) to

Table 1
Coefficients $a_{r,uw,\ell}$ for the UW$(2r-1)$ reconstruction (6), for $r \in \{1,\ldots,9\}$.

ℓ	$r = 9$	$r = 8$	$r = 7$	$r = 6$	$r = 5$	$r = 4$	$r = 3$	$r = 2$	$r = 1$
−8	$\frac{56}{12{,}252{,}240}$								
−7	$\frac{-1015}{12{,}252{,}240}$	$\frac{-7}{360{,}360}$							
−6	$\frac{8777}{12{,}252{,}240}$	$\frac{113}{360{,}360}$	$\frac{30}{360{,}360}$						
−5	$\frac{-48{,}343}{12{,}252{,}240}$	$\frac{-867}{360{,}360}$	$\frac{-425}{360{,}360}$	$\frac{-1}{2772}$					
−4	$\frac{191{,}561}{12{,}252{,}240}$	$\frac{4229}{360{,}360}$	$\frac{2851}{360{,}360}$	$\frac{61}{13{,}860}$	$\frac{1}{630}$				
−3	$\frac{-588{,}127}{12{,}252{,}240}$	$\frac{-14{,}881}{360{,}360}$	$\frac{-12{,}164}{360{,}360}$	$\frac{-703}{27{,}720}$	$\frac{-41}{2520}$	$\frac{-1}{140}$			
−2	$\frac{1{,}491{,}041}{12{,}252{,}240}$	$\frac{41{,}175}{360{,}360}$	$\frac{37{,}886}{360{,}360}$	$\frac{371}{3960}$	$\frac{199}{2520}$	$\frac{5}{84}$	$\frac{1}{30}$		
−1	$\frac{-3{,}409{,}855}{12{,}252{,}240}$	$\frac{-98{,}965}{360{,}360}$	$\frac{-97{,}249}{360{,}360}$	$\frac{-7303}{27{,}720}$	$\frac{-641}{2520}$	$\frac{-101}{420}$	$\frac{-13}{60}$	$\frac{-1}{6}$	
0	$\frac{8{,}842{,}385}{12{,}252{,}240}$	$\frac{261{,}395}{360{,}360}$	$\frac{263{,}111}{360{,}360}$	$\frac{20{,}417}{27{,}720}$	$\frac{1879}{2520}$	$\frac{319}{420}$	$\frac{47}{60}$	$\frac{5}{6}$	1
+1	$\frac{7{,}481{,}025}{12{,}252{,}240}$	$\frac{216{,}350}{360{,}360}$	$\frac{211{,}631}{360{,}360}$	$\frac{15{,}797}{27{,}720}$	$\frac{275}{504}$	$\frac{107}{210}$	$\frac{9}{20}$	$\frac{1}{3}$	
+2	$\frac{-2{,}320{,}767}{12{,}252{,}240}$	$\frac{-63{,}930}{360{,}360}$	$\frac{-58{,}639}{360{,}360}$	$\frac{-4003}{27{,}720}$	$\frac{-61}{504}$	$\frac{-19}{210}$	$\frac{-1}{20}$		
+3	$\frac{797{,}985}{12{,}252{,}240}$	$\frac{20{,}154}{360{,}360}$	$\frac{16{,}436}{360{,}360}$	$\frac{947}{27{,}720}$	$\frac{11}{504}$	$\frac{1}{105}$			
+4	$\frac{-241{,}599}{12{,}252{,}240}$	$\frac{-5326}{360{,}360}$	$\frac{-3584}{360{,}360}$	$\frac{-17}{3080}$	$\frac{-1}{504}$				
+5	$\frac{58{,}281}{12{,}252{,}240}$	$\frac{1044}{360{,}360}$	$\frac{511}{360{,}360}$	$\frac{1}{2310}$					
+6	$\frac{-10{,}263}{12{,}252{,}240}$	$\frac{-132}{360{,}360}$	$\frac{-35}{360{,}360}$						
+7	$\frac{1161}{12{,}252{,}240}$	$\frac{8}{360{,}360}$							
+8	$\frac{-63}{12{,}252{,}240}$								

Table 2
Coefficients $a_{r,k_s,\ell}$ appearing in the definition of the reconstructions for the various stencils of the WENO$(2r-1)$ schemes (9), for $r \in \{1,\ldots,9\}$.

r	ℓ	$k_s=0$	$k_s=1$	$k_s=2$	$k_s=3$	$k_s=4$	$k_s=5$	$k_s=6$	$k_s=7$	$k_s=8$
9	8	$\frac{280}{2520}$	$\frac{-35}{2520}$	$\frac{10}{2520}$	$\frac{-5}{2520}$	$\frac{4}{2520}$	$\frac{-5}{2520}$	$\frac{10}{2520}$	$\frac{-35}{2520}$	$\frac{280}{2520}$
	7	$\frac{-2555}{2520}$	$\frac{325}{2520}$	$\frac{-95}{2520}$	$\frac{49}{2520}$	$\frac{-41}{2520}$	$\frac{55}{2520}$	$\frac{-125}{2520}$	$\frac{595}{2520}$	$\frac{4609}{2520}$
	6	$\frac{10{,}405}{2520}$	$\frac{-1355}{2520}$	$\frac{409}{2520}$	$\frac{-221}{2520}$	$\frac{199}{2520}$	$\frac{-305}{2520}$	$\frac{955}{2520}$	$\frac{3349}{2520}$	$\frac{-5471}{2520}$
	5	$\frac{-24{,}875}{2520}$	$\frac{3349}{2520}$	$\frac{-1061}{2520}$	$\frac{619}{2520}$	$\frac{-641}{2520}$	$\frac{1375}{2520}$	$\frac{2509}{2520}$	$\frac{-2531}{2520}$	$\frac{6289}{2520}$
	4	$\frac{38{,}629}{2520}$	$\frac{-5471}{2520}$	$\frac{1879}{2520}$	$\frac{-1271}{2520}$	$\frac{1879}{2520}$	$\frac{1879}{2520}$	$\frac{-1271}{2520}$	$\frac{1879}{2520}$	$\frac{-5471}{2520}$
	3	$\frac{-40{,}751}{2520}$	$\frac{6289}{2520}$	$\frac{-2531}{2520}$	$\frac{2509}{2520}$	$\frac{1375}{2520}$	$\frac{-641}{2520}$	$\frac{619}{2520}$	$\frac{-1061}{2520}$	$\frac{3349}{2520}$
	2	$\frac{29{,}809}{2520}$	$\frac{-5471}{2520}$	$\frac{3349}{2520}$	$\frac{955}{2520}$	$\frac{-305}{2520}$	$\frac{199}{2520}$	$\frac{-221}{2520}$	$\frac{409}{2520}$	$\frac{-1355}{2520}$
	1	$\frac{-15{,}551}{2520}$	$\frac{4609}{2520}$	$\frac{595}{2520}$	$\frac{-125}{2520}$	$\frac{55}{2520}$	$\frac{-41}{2520}$	$\frac{49}{2520}$	$\frac{-95}{2520}$	$\frac{325}{2520}$
	0	$\frac{7129}{2520}$	$\frac{280}{2520}$	$\frac{-35}{2520}$	$\frac{10}{2520}$	$\frac{-5}{2520}$	$\frac{4}{2520}$	$\frac{-5}{2520}$	$\frac{10}{2520}$	$\frac{-35}{2520}$
8	7	$\frac{-105}{840}$	$\frac{15}{840}$	$\frac{-5}{840}$	$\frac{3}{840}$	$\frac{-3}{840}$	$\frac{5}{840}$	$\frac{-15}{840}$	$\frac{105}{840}$	
	6	$\frac{855}{840}$	$\frac{-125}{840}$	$\frac{43}{840}$	$\frac{-27}{840}$	$\frac{29}{840}$	$\frac{-55}{840}$	$\frac{225}{840}$	$\frac{1443}{840}$	
	5	$\frac{-3065}{840}$	$\frac{463}{840}$	$\frac{-167}{840}$	$\frac{113}{840}$	$\frac{-139}{840}$	$\frac{365}{840}$	$\frac{1023}{840}$	$\frac{-1497}{840}$	
	4	$\frac{6343}{840}$	$\frac{-1007}{840}$	$\frac{393}{840}$	$\frac{-307}{840}$	$\frac{533}{840}$	$\frac{743}{840}$	$\frac{-657}{840}$	$\frac{1443}{840}$	
	3	$\frac{-8357}{840}$	$\frac{1443}{840}$	$\frac{-657}{840}$	$\frac{743}{840}$	$\frac{533}{840}$	$\frac{-307}{840}$	$\frac{393}{840}$	$\frac{-1007}{840}$	
	2	$\frac{7323}{840}$	$\frac{-1497}{840}$	$\frac{1023}{840}$	$\frac{365}{840}$	$\frac{-139}{840}$	$\frac{113}{840}$	$\frac{-167}{840}$	$\frac{463}{840}$	
	1	$\frac{-4437}{840}$	$\frac{1443}{840}$	$\frac{225}{840}$	$\frac{-55}{840}$	$\frac{29}{840}$	$\frac{-27}{840}$	$\frac{43}{840}$	$\frac{-125}{840}$	
	0	$\frac{2283}{840}$	$\frac{105}{840}$	$\frac{-15}{840}$	$\frac{5}{840}$	$\frac{-3}{840}$	$\frac{3}{840}$	$\frac{-5}{840}$	$\frac{15}{840}$	
7	6	$\frac{60}{420}$	$\frac{-10}{420}$	$\frac{4}{420}$	$\frac{-3}{420}$	$\frac{4}{420}$	$\frac{-10}{420}$	$\frac{60}{420}$		
	5	$\frac{-430}{420}$	$\frac{74}{420}$	$\frac{-31}{420}$	$\frac{25}{420}$	$\frac{-38}{420}$	$\frac{130}{420}$	$\frac{669}{420}$		
	4	$\frac{1334}{420}$	$\frac{-241}{420}$	$\frac{109}{420}$	$\frac{-101}{420}$	$\frac{214}{420}$	$\frac{459}{420}$	$\frac{-591}{420}$		
	3	$\frac{-2341}{420}$	$\frac{459}{420}$	$\frac{-241}{420}$	$\frac{319}{420}$	$\frac{319}{420}$	$\frac{-241}{420}$	$\frac{459}{420}$		
	2	$\frac{2559}{420}$	$\frac{-591}{420}$	$\frac{459}{420}$	$\frac{214}{420}$	$\frac{-101}{420}$	$\frac{109}{420}$	$\frac{-241}{420}$		
	1	$\frac{-1851}{420}$	$\frac{669}{420}$	$\frac{130}{420}$	$\frac{-38}{420}$	$\frac{25}{420}$	$\frac{-31}{420}$	$\frac{74}{420}$		
	0	$\frac{1089}{420}$	$\frac{60}{420}$	$\frac{-10}{420}$	$\frac{4}{420}$	$\frac{-3}{420}$	$\frac{4}{420}$	$\frac{-10}{420}$		
6	5	$\frac{-1}{6}$	$\frac{1}{30}$	$\frac{-1}{60}$	$\frac{1}{60}$	$\frac{-1}{30}$	$\frac{1}{6}$			
	4	$\frac{31}{30}$	$\frac{-13}{60}$	$\frac{7}{60}$	$\frac{-2}{15}$	$\frac{11}{30}$	$\frac{29}{20}$			
	3	$\frac{-163}{60}$	$\frac{37}{60}$	$\frac{-23}{60}$	$\frac{37}{60}$	$\frac{19}{20}$	$\frac{-21}{20}$			
	2	$\frac{79}{20}$	$\frac{-21}{20}$	$\frac{19}{20}$	$\frac{37}{60}$	$\frac{-23}{60}$	$\frac{37}{60}$			
	1	$\frac{-71}{20}$	$\frac{29}{20}$	$\frac{11}{30}$	$\frac{-2}{15}$	$\frac{7}{60}$	$\frac{-13}{60}$			
	0	$\frac{49}{20}$	$\frac{1}{6}$	$\frac{-1}{30}$	$\frac{1}{60}$	$\frac{-1}{60}$	$\frac{1}{30}$			
5	4	$\frac{1}{5}$	$\frac{-1}{20}$	$\frac{1}{30}$	$\frac{-1}{20}$	$\frac{1}{5}$				
	3	$\frac{-21}{20}$	$\frac{17}{60}$	$\frac{-13}{60}$	$\frac{9}{20}$	$\frac{77}{60}$				
	2	$\frac{137}{60}$	$\frac{-43}{60}$	$\frac{47}{60}$	$\frac{47}{60}$	$\frac{-43}{60}$				
	1	$\frac{-163}{60}$	$\frac{77}{60}$	$\frac{9}{20}$	$\frac{-13}{60}$	$\frac{17}{60}$				
	0	$\frac{137}{60}$	$\frac{1}{5}$	$\frac{-1}{20}$	$\frac{1}{30}$	$\frac{-1}{20}$				
4	3	$\frac{-1}{4}$	$\frac{1}{12}$	$\frac{-1}{12}$	$\frac{1}{4}$					
	2	$\frac{13}{12}$	$\frac{-5}{12}$	$\frac{7}{12}$	$\frac{13}{12}$					
	1	$\frac{-23}{12}$	$\frac{13}{12}$	$\frac{7}{12}$	$\frac{-5}{12}$					
	0	$\frac{25}{12}$	$\frac{1}{4}$	$\frac{-1}{12}$	$\frac{1}{12}$					
3	2	$\frac{1}{3}$	$\frac{-1}{6}$	$\frac{1}{3}$						
	1	$\frac{-7}{6}$	$\frac{5}{6}$	$\frac{5}{6}$						
	0	$\frac{11}{6}$	$\frac{1}{3}$	$\frac{-1}{6}$						
2	1	$\frac{-1}{2}$	$\frac{1}{2}$							
	0	$\frac{3}{2}$	$\frac{1}{2}$							
1	0	1								

circumvent the problems of interacting characteristic fields and/or of absence of smooth stencils at a given point [5]. The ROR algorithm developed in the present work, generalizes previous work by Titarev and Toro [5], and is free of adjustable parameters. Several standard test-cases for the 1-D Euler equations [24–27,5,10] are computed, on progressively refined grids, using the RORWENOM$(2r-1)$ procedure. The results demonstrate that the resulting schemes are ENO, and, most importantly remain ENO when the grid is refined ($\Delta x \to 0$). In Section 6, we breifly discuss various possiblities for the extension of the UW$(2r-1)$ and WENOM$(2r-1)$ reconstructions to multidimensional problems. In Section 7, we apply the unsplit linewise multidimensional extension of the schemes to the linear 2-D advection equation, and verify that the accuracy results obtained for the 1-D case (Section 3) are also valid in 2-D. Finally, in Section 8, we investigate the performance of the unsplit linewise extension of the schemes for various standard test-cases for the 2-D Euler equations [26,28,29,3].

Table 3
Optimal weights C_{r,k_s} for the linear convex combination of the various stencils of the WENO$(2r-1)$ reconstructions yielding the UW$(2r-1)$ scheme (14), for $r \in \{1,\dots,9\}$.

r	$k_s=0$	$k_s=1$	$k_s=2$	$k_s=3$	$k_s=4$	$k_s=5$	$k_s=6$	$k_s=7$	$k_s=8$
9	$\frac{1}{24{,}310}$	$\frac{36}{12{,}155}$	$\frac{504}{12{,}155}$	$\frac{2352}{12{,}155}$	$\frac{882}{2431}$	$\frac{3528}{12{,}155}$	$\frac{1176}{12{,}155}$	$\frac{144}{12{,}155}$	$\frac{9}{24{,}310}$
8	$\frac{1}{6435}$	$\frac{56}{6435}$	$\frac{196}{2145}$	$\frac{392}{1287}$	$\frac{490}{1287}$	$\frac{392}{2145}$	$\frac{196}{6435}$	$\frac{8}{6435}$	
7	$\frac{1}{1716}$	$\frac{7}{286}$	$\frac{105}{572}$	$\frac{175}{429}$	$\frac{175}{572}$	$\frac{21}{286}$	$\frac{7}{1716}$		
6	$\frac{1}{462}$	$\frac{5}{77}$	$\frac{25}{77}$	$\frac{100}{231}$	$\frac{25}{154}$	$\frac{1}{77}$			
5	$\frac{1}{126}$	$\frac{10}{63}$	$\frac{10}{21}$	$\frac{20}{63}$	$\frac{5}{126}$				
4	$\frac{1}{35}$	$\frac{12}{35}$	$\frac{18}{35}$	$\frac{4}{35}$					
3	$\frac{1}{10}$	$\frac{6}{10}$	$\frac{3}{10}$						
2	$\frac{1}{3}$	$\frac{2}{3}$							
1	1								

Table 4
Coefficients $\sigma_{r,k_s,\ell,m}$ appearing in the definition of the smoothness indicators $\beta_{r,k_s,i+\frac{1}{2}}$ (16) for the WENO13 $(r=7)$ reconstruction.

ℓ	m	$k_s=0$	$k_s=1$	$k_s=2$	$k_s=3$	$k_s=4$	$k_s=5$	$k_s=6$
6	6	$\frac{62{,}911{,}297}{2{,}993{,}760}$	$\frac{64{,}361{,}771}{14{,}968{,}800}$	$\frac{2{,}627{,}203}{1{,}871{,}100}$	$\frac{2{,}627{,}203}{1{,}871{,}100}$	$\frac{64{,}361{,}771}{14{,}968{,}800}$	$\frac{62{,}911{,}297}{2{,}993{,}760}$	$\frac{897{,}207{,}163}{7{,}484{,}400}$
	5	$\frac{-5{,}556{,}669{,}277}{19{,}958{,}400}$	$\frac{-377{,}474{,}689}{6{,}652{,}800}$	$\frac{-359{,}321{,}429}{19{,}958{,}400}$	$\frac{-323{,}333{,}323}{19{,}958{,}400}$	$\frac{-295{,}455{,}983}{6{,}652{,}800}$	$\frac{-4{,}074{,}544{,}787}{19{,}958{,}400}$	$\frac{-22{,}763{,}092{,}357}{19{,}958{,}400}$
	4	$\frac{15{,}476{,}926{,}351}{19{,}958{,}400}$	$\frac{3{,}126{,}718{,}481}{19{,}958{,}400}$	$\frac{105{,}706{,}999}{2{,}217{,}600}$	$\frac{761{,}142{,}961}{19{,}958{,}400}$	$\frac{1{,}894{,}705{,}391}{19{,}958{,}400}$	$\frac{2{,}811{,}067{,}067}{6{,}652{,}800}$	$\frac{46{,}808{,}583{,}631}{19{,}958{,}400}$
	3	$\frac{-17{,}425{,}032{,}203}{14{,}968{,}800}$	$\frac{-3{,}465{,}607{,}493}{14{,}968{,}800}$	$\frac{-995{,}600{,}723}{14{,}968{,}800}$	$\frac{-701{,}563{,}133}{14{,}968{,}800}$	$\frac{-1{,}618{,}284{,}323}{14{,}968{,}800}$	$\frac{-7{,}124{,}638{,}253}{14{,}968{,}800}$	$\frac{-39{,}645{,}439{,}643}{14{,}968{,}800}$
	2	$\frac{4{,}964{,}771{,}899}{4{,}989{,}600}$	$\frac{320{,}782{,}183}{1{,}663{,}200}$	$\frac{256{,}556{,}849}{4{,}989{,}600}$	$\frac{158{,}544{,}319}{4{,}989{,}600}$	$\frac{115{,}524{,}053}{1{,}663{,}200}$	$\frac{1{,}531{,}307{,}249}{4{,}989{,}600}$	$\frac{8{,}579{,}309{,}749}{4{,}989{,}600}$
	1	$\frac{-9{,}181{,}961{,}959}{19{,}958{,}400}$	$\frac{-341{,}910{,}757}{3{,}991{,}680}$	$\frac{-15{,}401{,}629}{739{,}200}$	$\frac{-225{,}623{,}953}{19{,}958{,}400}$	$\frac{-95{,}508{,}139}{3{,}991{,}680}$	$\frac{-712{,}745{,}603}{6{,}652{,}800}$	$\frac{-2{,}416{,}885{,}043}{3{,}991{,}680}$
	0	$\frac{5{,}391{,}528{,}799}{59{,}875{,}200}$	$\frac{945{,}155{,}329}{59{,}875{,}200}$	$\frac{8{,}279{,}479}{2{,}395{,}008}$	$\frac{99{,}022{,}657}{59{,}875{,}200}$	$\frac{8{,}279{,}479}{2{,}395{,}008}$	$\frac{945{,}155{,}329}{59{,}875{,}200}$	$\frac{5{,}391{,}528{,}799}{59{,}875{,}200}$
5	5	$\frac{2{,}047{,}941{,}883}{2{,}217{,}600}$	$\frac{1{,}250{,}007{,}643}{6{,}652{,}800}$	$\frac{130{,}013{,}563}{2{,}217{,}600}$	$\frac{108{,}444{,}169}{2{,}217{,}600}$	$\frac{806{,}338{,}417}{6{,}652{,}800}$	$\frac{127{,}942{,}497}{246{,}400}$	$\frac{6{,}182{,}612{,}731}{2{,}217{,}600}$
	4	$\frac{-3{,}809{,}437{,}823}{739{,}200}$	$\frac{-6{,}932{,}480{,}657}{6{,}652{,}800}$	$\frac{-2{,}096{,}571{,}887}{6{,}652{,}800}$	$\frac{-176{,}498{,}513}{739{,}200}$	$\frac{-3{,}573{,}798{,}407}{6{,}652{,}800}$	$\frac{-14{,}684{,}933{,}057}{6{,}652{,}800}$	$\frac{-8{,}623{,}431{,}623}{739{,}200}$
	3	$\frac{38{,}683{,}385{,}051}{4{,}989{,}600}$	$\frac{857{,}838{,}469}{554{,}400}$	$\frac{2{,}224{,}538{,}011}{4{,}989{,}600}$	$\frac{1{,}506{,}944{,}981}{4{,}989{,}600}$	$\frac{1{,}042{,}531{,}337}{1{,}663{,}200}$	$\frac{12{,}601{,}009{,}501}{4{,}989{,}600}$	$\frac{66{,}440{,}049{,}371}{4{,}989{,}600}$
	2	$\frac{-14{,}734{,}178{,}999}{2{,}217{,}600}$	$\frac{-8{,}619{,}440{,}987}{6{,}652{,}800}$	$\frac{-773{,}749{,}439}{2{,}217{,}600}$	$\frac{-464{,}678{,}369}{2{,}217{,}600}$	$\frac{-2{,}725{,}575{,}317}{6{,}652{,}800}$	$\frac{-405{,}382{,}961}{246{,}400}$	$\frac{-19{,}308{,}505{,}679}{2{,}217{,}600}$
	1	$\frac{3{,}417{,}057{,}367}{1{,}108{,}800}$	$\frac{1{,}924{,}032{,}511}{3{,}326{,}400}$	$\frac{475{,}321{,}093}{3{,}326{,}400}$	$\frac{84{,}263{,}749}{1{,}108{,}800}$	$\frac{475{,}321{,}093}{3{,}326{,}400}$	$\frac{1{,}924{,}032{,}511}{3{,}326{,}400}$	$\frac{3{,}417{,}057{,}367}{1{,}108{,}800}$
	0	$\frac{-2{,}416{,}885{,}043}{3{,}991{,}680}$	$\frac{-712{,}745{,}603}{6{,}652{,}800}$	$\frac{-95{,}508{,}139}{3{,}991{,}680}$	$\frac{-225{,}623{,}953}{19{,}958{,}400}$	$\frac{-15{,}401{,}629}{739{,}200}$	$\frac{-341{,}910{,}757}{3{,}991{,}680}$	$\frac{-9{,}181{,}961{,}959}{19{,}958{,}400}$
4	4	$\frac{199{,}730{,}921}{27{,}720}$	$\frac{53{,}678{,}683}{36{,}960}$	$\frac{143{,}270{,}957}{332{,}640}$	$\frac{16{,}790{,}707}{55{,}440}$	$\frac{34{,}187{,}317}{55{,}440}$	$\frac{796{,}358{,}777}{332{,}640}$	$\frac{1{,}369{,}404{,}749}{110{,}880}$
	3	$\frac{-21{,}693{,}002{,}767}{997{,}920}$	$\frac{-4{,}330{,}640{,}057}{997{,}920}$	$\frac{-412{,}424{,}029}{332{,}640}$	$\frac{-790{,}531{,}177}{997{,}920}$	$\frac{-1{,}476{,}618{,}887}{997{,}920}$	$\frac{-616{,}410{,}313}{110{,}880}$	$\frac{-28{,}364{,}892{,}607}{997{,}920}$
	2	$\frac{8{,}290{,}771{,}913}{443{,}520}$	$\frac{4{,}868{,}089{,}189}{1{,}330{,}560}$	$\frac{1{,}312{,}114{,}459}{1{,}330{,}560}$	$\frac{250{,}523{,}543}{443{,}520}$	$\frac{1{,}312{,}114{,}459}{1{,}330{,}560}$	$\frac{4{,}868{,}089{,}189}{1{,}330{,}560}$	$\frac{8{,}290{,}771{,}913}{443{,}520}$
	1	$\frac{-19{,}308{,}505{,}679}{2{,}217{,}600}$	$\frac{-405{,}382{,}961}{246{,}400}$	$\frac{-2{,}725{,}575{,}317}{6{,}652{,}800}$	$\frac{-464{,}678{,}369}{2{,}217{,}600}$	$\frac{-773{,}749{,}439}{2{,}217{,}600}$	$\frac{-8{,}619{,}440{,}987}{6{,}652{,}800}$	$\frac{-14{,}734{,}178{,}999}{2{,}217{,}600}$
	0	$\frac{8{,}579{,}309{,}749}{4{,}989{,}600}$	$\frac{1{,}531{,}307{,}249}{4{,}989{,}600}$	$\frac{115{,}524{,}053}{1{,}663{,}200}$	$\frac{158{,}544{,}319}{4{,}989{,}600}$	$\frac{256{,}556{,}849}{4{,}989{,}600}$	$\frac{320{,}782{,}183}{1{,}663{,}200}$	$\frac{4{,}964{,}771{,}899}{4{,}989{,}600}$
3	3	$\frac{49{,}256{,}859{,}919}{2{,}993{,}760}$	$\frac{9{,}780{,}057{,}169}{2{,}993{,}760}$	$\frac{2{,}726{,}585{,}359}{2{,}993{,}760}$	$\frac{1{,}607{,}739{,}169}{2{,}993{,}760}$	$\frac{2{,}726{,}585{,}359}{2{,}993{,}760}$	$\frac{9{,}780{,}057{,}169}{2{,}993{,}760}$	$\frac{49{,}256{,}859{,}919}{2{,}993{,}760}$
	2	$\frac{-28{,}364{,}892{,}607}{997{,}920}$	$\frac{-616{,}410{,}313}{110{,}880}$	$\frac{-1{,}476{,}618{,}887}{997{,}920}$	$\frac{-790{,}531{,}177}{997{,}920}$	$\frac{-412{,}424{,}029}{332{,}640}$	$\frac{-4{,}330{,}640{,}057}{997{,}920}$	$\frac{-21{,}693{,}002{,}767}{997{,}920}$
	1	$\frac{66{,}440{,}049{,}371}{4{,}989{,}600}$	$\frac{12{,}601{,}009{,}501}{4{,}989{,}600}$	$\frac{1{,}042{,}531{,}337}{1{,}663{,}200}$	$\frac{1{,}506{,}944{,}981}{4{,}989{,}600}$	$\frac{2{,}224{,}538{,}011}{4{,}989{,}600}$	$\frac{857{,}838{,}469}{554{,}400}$	$\frac{38{,}683{,}385{,}051}{4{,}989{,}600}$
	0	$\frac{-39{,}645{,}439{,}643}{14{,}968{,}800}$	$\frac{-7{,}124{,}638{,}253}{14{,}968{,}800}$	$\frac{-1{,}618{,}284{,}323}{14{,}968{,}800}$	$\frac{-701{,}563{,}133}{14{,}968{,}800}$	$\frac{-995{,}600{,}723}{14{,}968{,}800}$	$\frac{-3{,}465{,}607{,}493}{14{,}968{,}800}$	$\frac{-17{,}425{,}032{,}203}{14{,}968{,}800}$
2	2	$\frac{1{,}369{,}404{,}749}{110{,}880}$	$\frac{796{,}358{,}777}{332{,}640}$	$\frac{34{,}187{,}317}{55{,}440}$	$\frac{16{,}790{,}707}{55{,}440}$	$\frac{143{,}270{,}957}{332{,}640}$	$\frac{53{,}678{,}683}{36{,}960}$	$\frac{199{,}730{,}921}{27{,}720}$
	1	$\frac{-8{,}623{,}431{,}623}{739{,}200}$	$\frac{-14{,}684{,}933{,}057}{6{,}652{,}800}$	$\frac{-3{,}573{,}798{,}407}{6{,}652{,}800}$	$\frac{-176{,}498{,}513}{739{,}200}$	$\frac{-2{,}096{,}571{,}887}{6{,}652{,}800}$	$\frac{-6{,}932{,}480{,}657}{6{,}652{,}800}$	$\frac{-3{,}809{,}437{,}823}{739{,}200}$
	0	$\frac{46{,}808{,}583{,}631}{19{,}958{,}400}$	$\frac{2{,}811{,}067{,}067}{6{,}652{,}800}$	$\frac{1{,}894{,}705{,}391}{19{,}958{,}400}$	$\frac{761{,}142{,}961}{19{,}958{,}400}$	$\frac{105{,}706{,}999}{2{,}217{,}600}$	$\frac{3{,}126{,}718{,}481}{19{,}958{,}400}$	$\frac{15{,}476{,}926{,}351}{19{,}958{,}400}$
1	1	$\frac{6{,}182{,}612{,}731}{2{,}217{,}600}$	$\frac{127{,}942{,}497}{246{,}400}$	$\frac{806{,}338{,}417}{6{,}652{,}800}$	$\frac{108{,}444{,}169}{2{,}217{,}600}$	$\frac{130{,}013{,}563}{2{,}217{,}600}$	$\frac{1{,}250{,}007{,}643}{6{,}652{,}800}$	$\frac{2{,}047{,}941{,}883}{2{,}217{,}600}$
	0	$\frac{-22{,}763{,}092{,}357}{19{,}958{,}400}$	$\frac{-4{,}074{,}544{,}787}{19{,}958{,}400}$	$\frac{-295{,}455{,}983}{6{,}652{,}800}$	$\frac{-323{,}333{,}323}{19{,}958{,}400}$	$\frac{-359{,}321{,}429}{19{,}958{,}400}$	$\frac{-377{,}474{,}689}{6{,}652{,}800}$	$\frac{-5{,}556{,}669{,}277}{19{,}958{,}400}$
0	0	$\frac{897{,}207{,}163}{7{,}484{,}400}$	$\frac{62{,}911{,}297}{2{,}993{,}760}$	$\frac{64{,}361{,}771}{14{,}968{,}800}$	$\frac{2{,}627{,}203}{1{,}871{,}100}$	$\frac{2{,}627{,}203}{1{,}871{,}100}$	$\frac{64{,}361{,}771}{14{,}968{,}800}$	$\frac{62{,}911{,}297}{2{,}993{,}760}$

2. WENO reconstruction

2.1. Polynomial reconstruction background

The principle underlying the development of upwind (UW) and weighted essentially nonoscillatory (WENO) reconstructions for the discretization of $f'(x)$ on a uniform grid $(x_i = x_1 + (i-1)\Delta x,\ i = 1,\dots,N_x)$ stems from the identity (on a uniform grid Δx = const)

Table 5
Coefficients $\sigma_{r,k_s,\ell,m}$ appearing in the definition of the smoothness indicators $\beta_{r,k_s,i+\frac{1}{2}}$ (16) for the WENO 15 ($r = 8$) reconstruction.

ℓ	m	$k_s = 0$	$k_s = 1$	$k_s = 2$	$k_s = 3$	$k_s = 4$	$k_s = 5$	$k_s = 6$	$k_s = 7$
7	7	$\frac{986,005,096,387}{20,756,736,000}$	$\frac{26,446,172,491}{2,965,248,000}$	$\frac{46,388,292,547}{20,756,736,000}$	$\frac{25,116,366,157}{20,756,736,000}$	$\frac{46,388,292,547}{20,756,736,000}$	$\frac{26,446,172,491}{2,965,248,000}$	$\frac{986,005,096,387}{20,756,736,000}$	$\frac{5,870,785,406,797}{20,756,736,000}$
	6	$\frac{-1,410,106,709,147}{1,945,944,000}$	$\frac{-132,173,819,131}{972,972,000}$	$\frac{-65,611,168,187}{1,945,944,000}$	$\frac{-2,407,377,043}{138,996,000}$	$\frac{-56,245,265,927}{1,945,944,000}$	$\frac{-104,391,937,861}{972,972,000}$	$\frac{-1,069,457,397,287}{1,945,944,000}$	$\frac{-3,130,718,954,431}{972,972,000}$
	5	$\frac{10,610,581,100,123}{4,447,872,000}$	$\frac{13,873,328,286,131}{31,135,104,000}$	$\frac{3,388,533,713,021}{31,135,104,000}$	$\frac{1,631,589,107,891}{31,135,104,000}$	$\frac{2,458,417,783,421}{31,135,104,000}$	$\frac{8,624,638,348,211}{31,135,104,000}$	$\frac{43,315,366,304,381}{31,135,104,000}$	$\frac{36,019,630,238,453}{4,447,872,000}$
	4	$\frac{-3,423,798,156,193}{778,377,600}$	$\frac{-90,744,192,823}{111,196,800}$	$\frac{-151,441,370,209}{778,377,600}$	$\frac{-67,513,265,377}{778,377,600}$	$\frac{-18,415,814,357}{155,675,520}$	$\frac{-310,726,966,393}{778,377,600}$	$\frac{-1,550,584,925,161}{778,377,600}$	$\frac{-9,030,771,744,409}{778,377,600}$
	3	$\frac{10,196,716,797,013}{2,075,673,600}$	$\frac{41,566,759,079}{46,126,080}$	$\frac{431,000,077,397}{2,075,673,600}$	$\frac{25,116,366,157}{296,524,800}$	$\frac{72,812,006,087}{691,891,200}$	$\frac{721,220,745,563}{2,075,673,600}$	$\frac{721,470,910,481}{415,134,720}$	$\frac{7,028,987,165,449}{691,891,200}$
	2	$\frac{-6,476,591,199,161}{1,945,944,000}$	$\frac{-583,488,131,053}{972,972,000}$	$\frac{-256,879,392,281}{1,945,944,000}$	$\frac{-47,469,340,603}{972,972,000}$	$\frac{-108,473,646,221}{1,945,944,000}$	$\frac{-25,412,164,549}{138,996,000}$	$\frac{-1,793,558,121,581}{1,945,944,000}$	$\frac{-5,269,260,407,953}{972,972,000}$
	1	$\frac{39,509,061,792,127}{31,135,104,000}$	$\frac{6,925,711,076,497}{31,135,104,000}$	$\frac{1,438,198,790,527}{31,135,104,000}$	$\frac{478,185,649,297}{31,135,104,000}$	$\frac{508,082,860,927}{31,135,104,000}$	$\frac{1,677,021,138,577}{31,135,104,000}$	$\frac{1,221,480,056,521}{4,447,872,000}$	$\frac{50,528,822,994,577}{31,135,104,000}$
	0	$\frac{-819,100,494,587}{3,891,888,000}$	$\frac{-137,801,870,867}{3,891,888,000}$	$\frac{-26,674,345,787}{3,891,888,000}$	$\frac{-7,942,541,267}{3,891,888,000}$	$\frac{-7,942,541,267}{3,891,888,000}$	$\frac{-26,674,345,787}{3,891,888,000}$	$\frac{-137,801,870,867}{3,891,888,000}$	$\frac{-819,100,494,587}{3,891,888,000}$
6	6	$\frac{172,229,708,657,639}{62,270,208,000}$	$\frac{32,268,504,444,809}{62,270,208,000}$	$\frac{7,965,255,985,319}{62,270,208,000}$	$\frac{3,944,861,897,609}{62,270,208,000}$	$\frac{6,047,605,530,599}{62,270,208,000}$	$\frac{20,863,031,646,089}{62,270,208,000}$	$\frac{102,080,471,419,559}{62,270,208,000}$	$\frac{581,791,881,407,369}{62,270,208,000}$
	5	$\frac{-70,944,310,593,109}{3,891,888,000}$	$\frac{-13,257,668,940,469}{3,891,888,000}$	$\frac{-3,233,549,114,749}{3,891,888,000}$	$\frac{-1,521,688,484,269}{3,891,888,000}$	$\frac{-2,129,103,852,829}{3,891,888,000}$	$\frac{-6,905,100,758,509}{3,891,888,000}$	$\frac{-32,903,428,273,669}{3,891,888,000}$	$\frac{-185,432,400,549,349}{3,891,888,000}$
	4	$\frac{41,910,140,004,779}{1,245,404,160}$	$\frac{38,941,083,744,793}{6,227,020,800}$	$\frac{9,306,913,817,431}{6,227,020,800}$	$\frac{4,100,880,843,289}{6,227,020,800}$	$\frac{5,227,966,881,367}{6,227,020,800}$	$\frac{3,240,510,296,069}{1,245,404,160}$	$\frac{76,273,513,229,143}{6,227,020,800}$	$\frac{428,668,917,728,281}{6,227,020,800}$
	3	$\frac{-4,882,688,924,777}{129,729,600}$	$\frac{-224,563,041,869}{32,432,400}$	$\frac{-41,643,930,661}{25,945,920}$	$\frac{-10,590,149,653}{16,216,200}$	$\frac{-98,765,696,693}{129,729,600}$	$\frac{-37,187,936,869}{16,216,200}$	$\frac{-1,397,571,412,901}{129,729,600}$	$\frac{-393,303,816,739}{6,486,480}$
	2	$\frac{795,325,997,722,517}{31,135,104,000}$	$\frac{143,887,855,797,947}{31,135,104,000}$	$\frac{31,959,522,170,837}{31,135,104,000}$	$\frac{11,870,432,980,667}{31,135,104,000}$	$\frac{12,752,830,987,157}{31,135,104,000}$	$\frac{37,913,679,009,467}{31,135,104,000}$	$\frac{178,922,840,432,597}{31,135,104,000}$	$\frac{1,010,731,494,899,387}{31,135,104,000}$
	1	$\frac{-12,661,520,644,021}{1,297,296,000}$	$\frac{-2,230,862,726,341}{1,297,296,000}$	$\frac{-468,561,665,821}{1,297,296,000}$	$\frac{-157,580,595,421}{1,297,296,000}$	$\frac{-157,580,595,421}{1,297,296,000}$	$\frac{-468,561,665,821}{1,297,296,000}$	$\frac{-2,230,862,726,341}{1,297,296,000}$	$\frac{-12,661,520,644,021}{1,297,296,000}$
	0	$\frac{50,528,822,994,577}{31,135,104,000}$	$\frac{1,221,480,056,521}{4,447,872,000}$	$\frac{1,677,021,138,577}{31,135,104,000}$	$\frac{508,082,860,927}{31,135,104,000}$	$\frac{478,185,649,297}{31,135,104,000}$	$\frac{1,438,198,790,527}{31,135,104,000}$	$\frac{6,925,711,076,497}{31,135,104,000}$	$\frac{39,509,061,792,127}{31,135,104,000}$
5	5	$\frac{624,177,436,330,267}{20,756,736,000}$	$\frac{116,487,285,372,277}{20,756,736,000}$	$\frac{28,199,161,918,747}{20,756,736,000}$	$\frac{12,780,967,457,077}{20,756,736,000}$	$\frac{16,476,387,815,707}{20,756,736,000}$	$\frac{49,883,478,342,517}{20,756,736,000}$	$\frac{229,456,135,916,827}{20,756,736,000}$	$\frac{1,272,280,750,118,197}{20,756,736,000}$
	4	$\frac{-983,492,927,359}{8,845,200}$	$\frac{-29,244,985,495}{1,415,232}$	$\frac{-5,445,142,127}{1,105,650}$	$\frac{-74,851,467,823}{35,380,800}$	$\frac{-5,527,715,497}{2,211,300}$	$\frac{-253,865,691,211}{35,380,800}$	$\frac{-11,450,077,957}{353,808}$	$\frac{-6,306,477,584,539}{35,380,800}$
	3	$\frac{775,760,249,154,827}{6,227,020,800}$	$\frac{142,950,967,195,973}{6,227,020,800}$	$\frac{33,191,727,291,659}{6,227,020,800}$	$\frac{532,071,643,661}{249,080,832}$	$\frac{14,416,393,946,891}{6,227,020,800}$	$\frac{39,896,100,785,477}{6,227,020,800}$	$\frac{178,559,835,040,523}{6,227,020,800}$	$\frac{982,150,494,698,309}{6,227,020,800}$
	2	$\frac{-109,928,049,802,589}{1,297,296,000}$	$\frac{-19,952,704,102,349}{1,297,296,000}$	$\frac{-4,456,767,285,989}{1,297,296,000}$	$\frac{-1,644,079,167,749}{1,297,296,000}$	$\frac{-1,644,079,167,749}{1,297,296,000}$	$\frac{-4,456,767,285,989}{1,297,296,000}$	$\frac{-19,952,704,102,349}{1,297,296,000}$	$\frac{-109,928,049,802,589}{1,297,296,000}$
	1	$\frac{1,010,731,494,899,387}{31,135,104,000}$	$\frac{178,922,840,432,597}{31,135,104,000}$	$\frac{37,913,679,009,467}{31,135,104,000}$	$\frac{12,752,830,987,157}{31,135,104,000}$	$\frac{11,870,432,980,667}{31,135,104,000}$	$\frac{31,959,522,170,837}{31,135,104,000}$	$\frac{143,887,855,797,947}{31,135,104,000}$	$\frac{795,325,997,722,517}{31,135,104,000}$
	0	$\frac{-5,269,260,407,953}{972,972,000}$	$\frac{-1,793,558,121,581}{1,945,944,000}$	$\frac{-25,412,164,549}{138,996,000}$	$\frac{-108,473,646,221}{1,945,944,000}$	$\frac{-47,469,340,603}{972,972,000}$	$\frac{-256,879,392,281}{1,945,944,000}$	$\frac{-583,488,131,053}{972,972,000}$	$\frac{-6,476,591,199,161}{1,945,944,000}$
4	4	$\frac{23,315,424,178,373}{226,437,120}$	$\frac{4,322,531,771,339}{226,437,120}$	$\frac{203,912,134,273}{45,287,424}$	$\frac{420,341,161,931}{226,437,120}$	$\frac{457,249,528,517}{226,437,120}$	$\frac{1,231,949,387,723}{226,437,120}$	$\frac{5,407,733,702,789}{226,437,120}$	$\frac{5,896,382,977,423}{45,287,424}$
	3	$\frac{-35,999,233,471,051}{155,675,520}$	$\frac{-6,630,479,776,771}{155,675,520}$	$\frac{-1,532,094,364,651}{155,675,520}$	$\frac{-595,915,721,251}{155,675,520}$	$\frac{-595,915,721,251}{155,675,520}$	$\frac{-1,532,094,364,651}{155,675,520}$	$\frac{-6,630,479,776,771}{155,675,520}$	$\frac{-35,999,233,471,051}{155,675,520}$
	2	$\frac{982,150,494,698,309}{6,227,020,800}$	$\frac{178,559,835,040,523}{6,227,020,800}$	$\frac{39,896,100,785,477}{6,227,020,800}$	$\frac{14,416,393,946,891}{6,227,020,800}$	$\frac{532,071,643,661}{249,080,832}$	$\frac{33,191,727,291,659}{6,227,020,800}$	$\frac{142,950,967,195,973}{6,227,020,800}$	$\frac{775,760,249,154,827}{6,227,020,800}$
	1	$\frac{-393,303,816,739}{6,486,480}$	$\frac{-1,397,571,412,901}{129,729,600}$	$\frac{-37,187,936,869}{16,216,200}$	$\frac{-98,765,696,693}{129,729,600}$	$\frac{-10,590,149,653}{16,216,200}$	$\frac{-41,643,930,661}{25,945,920}$	$\frac{-224,563,041,869}{32,432,400}$	$\frac{-4,882,688,924,777}{129,729,600}$
	0	$\frac{7,028,987,165,449}{691,891,200}$	$\frac{721,470,910,481}{415,134,720}$	$\frac{721,220,745,563}{2,075,673,600}$	$\frac{72,812,006,087}{691,891,200}$	$\frac{25,116,366,157}{296,524,800}$	$\frac{431,000,077,397}{2,075,673,600}$	$\frac{41,566,759,079}{46,126,080}$	$\frac{10,196,716,797,013}{2,075,673,600}$
3	3	$\frac{5,896,382,977,423}{45,287,424}$	$\frac{5,407,733,702,789}{226,437,120}$	$\frac{1,231,949,387,723}{226,437,120}$	$\frac{457,249,528,517}{226,437,120}$	$\frac{420,341,161,931}{226,437,120}$	$\frac{203,912,134,273}{45,287,424}$	$\frac{4,322,531,771,339}{226,437,120}$	$\frac{23,315,424,178,373}{226,437,120}$
	2	$\frac{-6,306,477,584,539}{35,380,800}$	$\frac{-11,450,077,957}{353,808}$	$\frac{-253,865,691,211}{35,380,800}$	$\frac{-5,527,715,497}{2,211,300}$	$\frac{-74,851,467,823}{35,380,800}$	$\frac{-5,445,142,127}{1,105,650}$	$\frac{-29,244,985,495}{1,415,232}$	$\frac{-983,492,927,359}{8,845,200}$
	1	$\frac{428,668,917,728,281}{6,227,020,800}$	$\frac{76,273,513,229,143}{6,227,020,800}$	$\frac{3,240,510,296,069}{1,245,404,160}$	$\frac{5,227,966,881,367}{6,227,020,800}$	$\frac{4,100,880,843,289}{6,227,020,800}$	$\frac{9,306,913,817,431}{6,227,020,800}$	$\frac{38,941,083,744,793}{6,227,020,800}$	$\frac{41,910,140,004,779}{1,245,404,160}$
	0	$\frac{-9,030,771,744,409}{778,377,600}$	$\frac{-1,550,584,925,161}{778,377,600}$	$\frac{-310,726,966,393}{778,377,600}$	$\frac{-18,415,814,357}{155,675,520}$	$\frac{-67,513,265,377}{778,377,600}$	$\frac{-151,441,370,209}{778,377,600}$	$\frac{-90,744,192,823}{111,196,800}$	$\frac{-3,423,798,156,193}{778,377,600}$
2	2	$\frac{1,272,280,750,118,197}{20,756,736,000}$	$\frac{229,456,135,916,827}{20,756,736,000}$	$\frac{49,883,478,342,517}{20,756,736,000}$	$\frac{16,476,387,815,707}{20,756,736,000}$	$\frac{12,780,967,457,077}{20,756,736,000}$	$\frac{28,199,161,918,747}{20,756,736,000}$	$\frac{116,487,285,372,277}{20,756,736,000}$	$\frac{624,177,436,330,267}{20,756,736,000}$
	1	$\frac{-185,432,400,549,349}{3,891,888,000}$	$\frac{-32,903,428,273,669}{3,891,888,000}$	$\frac{-6,905,100,758,509}{3,891,888,000}$	$\frac{-2,129,103,852,829}{3,891,888,000}$	$\frac{-1,521,688,484,269}{3,891,888,000}$	$\frac{-3,233,549,114,749}{3,891,888,000}$	$\frac{-13,257,668,940,469}{3,891,888,000}$	$\frac{-70,944,310,593,109}{3,891,888,000}$
	0	$\frac{36,019,630,238,453}{4,447,872,000}$	$\frac{43,315,366,304,381}{31,135,104,000}$	$\frac{8,624,638,348,211}{31,135,104,000}$	$\frac{2,458,417,783,421}{31,135,104,000}$	$\frac{1,631,589,107,891}{31,135,104,000}$	$\frac{3,388,533,713,021}{31,135,104,000}$	$\frac{13,873,328,286,131}{31,135,104,000}$	$\frac{10,610,581,100,123}{4,447,872,000}$
1	1	$\frac{581,791,881,407,369}{62,270,208,000}$	$\frac{102,080,471,419,559}{62,270,208,000}$	$\frac{20,863,031,646,089}{62,270,208,000}$	$\frac{6,047,605,530,599}{62,270,208,000}$	$\frac{3,944,861,897,609}{62,270,208,000}$	$\frac{7,965,255,985,319}{62,270,208,000}$	$\frac{32,268,504,444,809}{62,270,208,000}$	$\frac{172,229,708,657,639}{62,270,208,000}$
	0	$\frac{-3,130,718,954,431}{972,972,000}$	$\frac{-1,069,457,397,287}{1,945,944,000}$	$\frac{-104,391,937,861}{972,972,000}$	$\frac{-56,245,265,927}{1,945,944,000}$	$\frac{-2,407,377,043}{138,996,000}$	$\frac{-65,611,168,187}{1,945,944,000}$	$\frac{-132,173,819,131}{972,972,000}$	$\frac{-1,410,106,709,147}{1,945,944,000}$
0	0	$\frac{5,870,785,406,797}{20,756,736,000}$	$\frac{986,005,096,387}{20,756,736,000}$	$\frac{26,446,172,491}{2,965,248,000}$	$\frac{46,388,292,547}{20,756,736,000}$	$\frac{25,116,366,157}{20,756,736,000}$	$\frac{46,388,292,547}{20,756,736,000}$	$\frac{26,446,172,491}{2,965,248,000}$	$\frac{986,005,096,387}{20,756,736,000}$

$$\frac{d}{dx}\left[\frac{1}{\Delta x}\int_{x-\frac{1}{2}\Delta x}^{x+\frac{1}{2}\Delta x} h(\xi)\,d\xi\right] = \frac{h\left(x+\frac{1}{2}\Delta x\right) - h\left(x-\frac{1}{2}\Delta x\right)}{\Delta x} \tag{1}$$

obtained by straightforward application of the Leibniz rule [30, pp. 411–412]. From (1) it follows that if a function $h(x)$ could be found such that

$$f(x) = \frac{1}{\Delta x}\int_{x-\frac{1}{2}\Delta x}^{x+\frac{1}{2}\Delta x} h(\xi)\,d\xi \overset{(1)}{\Rightarrow} f'(x) = \frac{h\left(x+\frac{1}{2}\Delta x\right) - h\left(x-\frac{1}{2}\Delta x\right)}{\Delta x} \tag{2}$$

Table 6
Coefficients $\sigma_{r,k_s,\ell,m}$ appearing in the definition of the smoothness indicators $\beta_{r,k_s,i+\frac{1}{2}}$ (16) for the WENO17 ($r=9$) reconstruction.

ℓ	m	$k_s=0$	$k_s=1$	$k_s=2$	$k_s=3$	$k_s=4$	$k_s=5$	$k_s=6$	$k_s=7$	$k_s=8$
8	8	$\frac{17,848,737,251,203}{163,459,296,000}$	$\frac{3,165,355,170,121}{163,459,296,000}$	$\frac{679,328,101,453}{163,459,296,000}$	$\frac{238,114,846,399}{163,459,296,000}$	$\frac{238,114,846,399}{163,459,296,000}$	$\frac{679,328,101,453}{163,459,296,000}$	$\frac{3,165,355,170,121}{163,459,296,000}$	$\frac{17,848,737,251,203}{163,459,296,000}$	$\frac{109,471,139,332,699}{163,459,296,000}$
	7	$\frac{-189,555,672,759,617}{100,590,336,000}$	$\frac{-33,593,572,337,951}{100,590,336,000}$	$\frac{-1,026,441,378,647}{14,370,048,000}$	$\frac{-2,466,233,185,151}{100,590,336,000}$	$\frac{-2,297,804,363,777}{100,590,336,000}$	$\frac{-6,056,041,731,167}{100,590,336,000}$	$\frac{-3,844,139,848,343}{14,370,048,000}$	$\frac{-147,809,125,548,479}{100,590,336,000}$	$\frac{-894,628,364,420,801}{100,590,336,000}$
	6	$\frac{9,355,064,903,078,053}{1,307,674,368,000}$	$\frac{1,655,072,196,501,883}{1,307,674,368,000}$	$\frac{70,341,062,456,897}{261,534,873,600}$	$\frac{117,272,649,474,139}{1,307,674,368,000}$	$\frac{20,216,075,320,673}{261,534,873,600}$	$\frac{247,582,660,569,403}{1,307,674,368,000}$	$\frac{1,063,191,201,446,533}{1,307,674,368,000}$	$\frac{1,152,669,616,433,567}{261,534,873,600}$	$\frac{34,709,567,828,765,989}{1,307,674,368,000}$
	5	$\frac{-816,990,037,454,483}{52,306,974,720}$	$\frac{-3,601,784,423,075,141}{1,307,674,368,000}$	$\frac{-757,402,017,640,571}{1,307,674,368,000}$	$\frac{-48,633,489,917,473}{261,534,873,600}$	$\frac{-192,700,060,973,723}{1,307,674,368,000}$	$\frac{-17,694,932,119,757}{52,306,974,720}$	$\frac{-1,859,899,247,394,491}{1,307,674,368,000}$	$\frac{-10,036,258,935,621,221}{1,307,674,368,000}$	$\frac{-12,083,632,055,537,503}{261,534,873,600}$
	4	$\frac{1,123,058,785,015,051}{52,306,974,720}$	$\frac{984,850,182,064,169}{261,534,873,600}$	$\frac{203,891,614,104,599}{261,534,873,600}$	$\frac{2,497,209,723,185}{10,461,394,944}$	$\frac{45,272,942,020,727}{261,534,873,600}$	$\frac{19,690,918,384,021}{52,306,974,720}$	$\frac{409,921,790,776,919}{261,534,873,600}$	$\frac{2,214,259,153,735,049}{261,534,873,600}$	$\frac{534,237,095,117,903}{10,461,394,944}$
	3	$\frac{-24,911,758,529,750,003}{1,307,674,368,000}$	$\frac{-4,331,747,069,079,341}{1,307,674,368,000}$	$\frac{-877,252,492,928,723}{1,307,674,368,000}$	$\frac{-253,674,820,236,749}{1,307,674,368,000}$	$\frac{-167,888,314,942,259}{1,307,674,368,000}$	$\frac{-350,067,382,006,253}{1,307,674,368,000}$	$\frac{-1,457,105,112,643,091}{1,307,674,368,000}$	$\frac{-7,906,584,673,048,973}{1,307,674,368,000}$	$\frac{-47,841,342,141,981,299}{1,307,674,368,000}$
	2	$\frac{13,952,443,929,995,611}{1,307,674,368,000}$	$\frac{2,394,338,101,248,133}{1,307,674,368,000}$	$\frac{470,643,665,358,907}{1,307,674,368,000}$	$\frac{127,326,292,586,533}{1,307,674,368,000}$	$\frac{76,858,903,972,891}{1,307,674,368,000}$	$\frac{155,614,950,712,261}{1,307,674,368,000}$	$\frac{652,452,925,567,483}{1,307,674,368,000}$	$\frac{3,563,951,929,254,757}{1,307,674,368,000}$	$\frac{21,644,628,077,515,483}{1,307,674,368,000}$
	1	$\frac{-4,517,524,574,525,093}{1,307,674,368,000}$	$\frac{-760,053,376,543,163}{1,307,674,368,000}$	$\frac{-5,748,413,034,701}{52,306,974,720}$	$\frac{-36,073,774,922,459}{1,307,674,368,000}$	$\frac{-3,976,300,410,337}{261,534,873,600}$	$\frac{-39,587,674,152,443}{1,307,674,368,000}$	$\frac{-168,172,381,487,813}{1,307,674,368,000}$	$\frac{-7,406,462,028,919}{10,461,394,944}$	$\frac{-5,644,399,400,246,309}{1,307,674,368,000}$
	0	$\frac{129,739,906,408,601}{261,534,873,600}$	$\frac{105,994,418,298,211}{1,307,674,368,000}$	$\frac{19,094,704,104,061}{1,307,674,368,000}$	$\frac{883,416,230,471}{261,534,873,600}$	$\frac{2,227,506,474,493}{1,307,674,368,000}$	$\frac{883,416,230,471}{261,534,873,600}$	$\frac{19,094,704,104,061}{1,307,674,368,000}$	$\frac{105,994,418,298,211}{1,307,674,368,000}$	$\frac{129,739,906,408,601}{261,534,873,600}$
7	7	$\frac{10,637,354,815,456,613}{1,307,674,368,000}$	$\frac{269,247,491,159,069}{186,810,624,000}$	$\frac{402,355,798,141,541}{1,307,674,368,000}$	$\frac{136,155,780,967,307}{1,307,674,368,000}$	$\frac{119,979,314,906,981}{1,307,674,368,000}$	$\frac{293,675,114,165,963}{1,307,674,368,000}$	$\frac{1,239,990,283,564,133}{1,307,674,368,000}$	$\frac{6,603,455,065,054,091}{1,307,674,368,000}$	$\frac{5,602,753,233,305,651}{186,810,624,000}$
	6	$\frac{-20,204,125,377,340,061}{326,918,592,000}$	$\frac{-3,575,411,646,556,907}{326,918,592,000}$	$\frac{-759,598,480,120,637}{326,918,592,000}$	$\frac{-251,283,767,228,651}{326,918,592,000}$	$\frac{-207,359,252,612,669}{326,918,592,000}$	$\frac{-472,662,830,894,411}{326,918,592,000}$	$\frac{-1,918,610,096,603,357}{326,918,592,000}$	$\frac{-10,036,779,580,858,187}{326,918,592,000}$	$\frac{-59,111,412,950,734,301}{326,918,592,000}$
	5	$\frac{88,287,149,743,355,417}{653,837,184,000}$	$\frac{3,116,380,997,521,963}{130,767,436,800}$	$\frac{3,281,427,995,720,729}{653,837,184,000}$	$\frac{1,051,238,439,516,119}{653,837,184,000}$	$\frac{161,084,839,253,509}{130,767,436,800}$	$\frac{1,720,297,891,825,367}{653,837,184,000}$	$\frac{1,359,891,017,166,853}{130,767,436,800}$	$\frac{35,272,568,778,872,279}{653,837,184,000}$	$\frac{207,178,084,258,860,569}{653,837,184,000}$
	4	$\frac{-24,293,471,434,588,703}{130,767,436,800}$	$\frac{-4,266,972,749,341,649}{130,767,436,800}$	$\frac{-886,173,785,909,759}{130,767,436,800}$	$\frac{-272,139,518,377,073}{130,767,436,800}$	$\frac{-192,310,346,872,991}{130,767,436,800}$	$\frac{-388,442,316,668,753}{130,767,436,800}$	$\frac{-1,512,744,281,500,799}{130,767,436,800}$	$\frac{-7,832,368,115,834,609}{130,767,436,800}$	$\frac{-46,020,384,090,357,023}{130,767,436,800}$
	3	$\frac{107,887,390,486,248,143}{653,837,184,000}$	$\frac{18,799,624,487,562,689}{653,837,184,000}$	$\frac{3,825,435,713,279,951}{653,837,184,000}$	$\frac{1,114,386,138,224,129}{653,837,184,000}$	$\frac{723,357,784,442,063}{653,837,184,000}$	$\frac{1,397,141,337,414,593}{653,837,184,000}$	$\frac{5,414,972,538,444,239}{653,837,184,000}$	$\frac{28,101,378,954,880,001}{653,837,184,000}$	$\frac{165,445,178,916,726,479}{653,837,184,000}$
	2	$\frac{-30,250,052,825,497,529}{326,918,592,000}$	$\frac{-5,205,585,064,855,199}{326,918,592,000}$	$\frac{-1,029,608,247,917,273}{326,918,592,000}$	$\frac{-281,678,601,090,911}{326,918,592,000}$	$\frac{-167,690,675,241,113}{326,918,592,000}$	$\frac{-313,421,131,078,079}{326,918,592,000}$	$\frac{-1,218,782,466,526,649}{326,918,592,000}$	$\frac{-6,356,537,203,415,423}{326,918,592,000}$	$\frac{-37,531,036,453,047,161}{326,918,592,000}$
	1	$\frac{137,189,721,025,309}{4,572,288,000}$	$\frac{23,159,841,631,123}{4,572,288,000}$	$\frac{4,411,553,510,173}{4,572,288,000}$	$\frac{1,123,540,717,459}{4,572,288,000}$	$\frac{613,753,663,261}{4,572,288,000}$	$\frac{1,123,540,717,459}{4,572,288,000}$	$\frac{4,411,553,510,173}{4,572,288,000}$	$\frac{23,159,841,631,123}{4,572,288,000}$	$\frac{137,189,721,025,309}{4,572,288,000}$
	0	$\frac{-5,644,399,400,246,309}{1,307,674,368,000}$	$\frac{-7,406,462,028,919}{10,461,394,944}$	$\frac{-168,172,381,487,813}{1,307,674,368,000}$	$\frac{-39,587,674,152,443}{1,307,674,368,000}$	$\frac{-3,976,300,410,337}{261,534,873,600}$	$\frac{-36,073,774,922,459}{1,307,674,368,000}$	$\frac{-5,748,413,034,701}{52,306,974,720}$	$\frac{-760,053,376,543,163}{1,307,674,368,000}$	$\frac{-4,517,524,574,525,093}{1,307,674,368,000}$
6	6	$\frac{1,994,952,741,927,931}{16,982,784,000}$	$\frac{352,812,369,719,413}{16,982,784,000}$	$\frac{74,730,821,653,819}{16,982,784,000}$	$\frac{24,324,934,655,989}{16,982,784,000}$	$\frac{19,010,310,966,523}{16,982,784,000}$	$\frac{40,385,614,392,181}{16,982,784,000}$	$\frac{156,622,544,328,763}{16,982,784,000}$	$\frac{800,572,672,346,869}{16,982,784,000}$	$\frac{4,660,712,172,178,939}{16,982,784,000}$
	5	$\frac{-23,993,743,892,557,601}{46,702,656,000}$	$\frac{-4,234,862,610,936,119}{46,702,656,000}$	$\frac{-890,937,252,684,641}{46,702,656,000}$	$\frac{-282,622,107,973,367}{46,702,656,000}$	$\frac{-207,059,158,040,897}{46,702,656,000}$	$\frac{-411,721,854,332,951}{46,702,656,000}$	$\frac{-1,544,964,557,143,169}{46,702,656,000}$	$\frac{-7,795,675,329,471,191}{46,702,656,000}$	$\frac{-45,148,728,224,254,817}{46,702,656,000}$
	4	$\frac{150,205,347,326,833}{212,284,800}$	$\frac{26,403,598,814,209}{212,284,800}$	$\frac{5,489,435,141,989}{212,284,800}$	$\frac{1,679,094,624,733}{212,284,800}$	$\frac{1,143,576,251,161}{212,284,800}$	$\frac{2,145,005,788,633}{212,284,800}$	$\frac{7,883,820,528,109}{212,284,800}$	$\frac{39,564,077,889,589}{212,284,800}$	$\frac{228,786,920,178,433}{212,284,800}$
	3	$\frac{-29,387,187,771,747,941}{46,702,656,000}$	$\frac{-5,129,104,009,946,051}{46,702,656,000}$	$\frac{-209,388,842,757,121}{9,340,531,200}$	$\frac{-305,368,847,812,163}{46,702,656,000}$	$\frac{-38,450,763,316,993}{9,340,531,200}$	$\frac{-343,655,982,425,891}{46,702,656,000}$	$\frac{-1,250,454,991,752,101}{46,702,656,000}$	$\frac{-1,254,519,948,165,511}{9,340,531,200}$	$\frac{-36,294,580,012,168,613}{46,702,656,000}$
	2	$\frac{33,008,527,082,236,991}{93,405,312,000}$	$\frac{5,694,325,930,465,457}{93,405,312,000}$	$\frac{1,131,898,542,897,407}{93,405,312,000}$	$\frac{311,458,280,689,841}{93,405,312,000}$	$\frac{180,786,151,740,479}{93,405,312,000}$	$\frac{311,458,280,689,841}{93,405,312,000}$	$\frac{1,131,898,542,897,407}{93,405,312,000}$	$\frac{5,694,325,930,465,457}{93,405,312,000}$	$\frac{33,008,527,082,236,991}{93,405,312,000}$
	1	$\frac{-37,531,036,453,047,161}{326,918,592,000}$	$\frac{-6,356,537,203,415,423}{326,918,592,000}$	$\frac{-1,218,782,466,526,649}{326,918,592,000}$	$\frac{-313,421,131,078,079}{326,918,592,000}$	$\frac{-167,690,675,241,113}{326,918,592,000}$	$\frac{-281,678,601,090,911}{326,918,592,000}$	$\frac{-1,029,608,247,917,273}{326,918,592,000}$	$\frac{-5,205,585,064,855,199}{326,918,592,000}$	$\frac{-30,250,052,825,497,529}{326,918,592,000}$
	0	$\frac{21,644,628,077,515,483}{1,307,674,368,000}$	$\frac{3,563,951,929,254,757}{1,307,674,368,000}$	$\frac{652,452,925,567,483}{1,307,674,368,000}$	$\frac{155,614,950,712,261}{1,307,674,368,000}$	$\frac{76,858,903,972,891}{1,307,674,368,000}$	$\frac{127,326,292,586,533}{1,307,674,368,000}$	$\frac{470,643,665,358,907}{1,307,674,368,000}$	$\frac{2,394,338,101,248,133}{1,307,674,368,000}$	$\frac{13,952,443,929,995,611}{1,307,674,368,000}$

5	5	$\frac{105,045,730,109,557,451}{186,810,624,000}$	$\frac{18,518,028,023,237,957}{186,810,624,000}$	$\frac{3,878,296,682,785,739}{186,810,624,000}$	$\frac{1,206,964,694,318,597}{186,810,624,000}$	$\frac{836,484,368,637,131}{186,810,624,000}$	$\frac{1,553,225,813,426,501}{186,810,624,000}$	$\frac{5,599,666,272,693,707}{186,810,624,000}$	$\frac{27,770,723,927,721,989}{186,810,624,000}$	$\frac{159,646,773,711,558,347}{186,810,624,000}$
	4	$\frac{-5,794,119,024,433,483}{3,736,212,480}$	$\frac{-5,091,060,727,437,401}{18,681,062,400}$	$\frac{-1,056,291,616,534,871}{18,681,062,400}$	$\frac{-63,811,818,908,581}{3,736,212,480}$	$\frac{-207,139,067,201,783}{18,681,062,400}$	$\frac{-72,310,955,346,373}{3,736,212,480}$	$\frac{-1,267,992,294,203,351}{18,681,062,400}$	$\frac{-6,230,647,138,120,121}{18,681,062,400}$	$\frac{-7,140,074,733,899,851}{3,736,212,480}$
	3	$\frac{25,802,513,458,691,833}{18,681,062,400}$	$\frac{22,533,757,546,843,859}{93,405,312,000}$	$\frac{4,601,782,036,044,509}{93,405,312,000}$	$\frac{266,698,467,235,063}{18,681,062,400}$	$\frac{805,195,803,373,277}{93,405,312,000}$	$\frac{266,698,467,235,063}{18,681,062,400}$	$\frac{4,601,782,036,044,509}{93,405,312,000}$	$\frac{22,533,757,546,843,859}{93,405,312,000}$	$\frac{25,802,513,458,691,833}{18,681,062,400}$
	2	$\frac{-36,294,580,012,168,613}{46,702,656,000}$	$\frac{-1,254,519,948,165,511}{9,340,531,200}$	$\frac{-1,250,454,991,752,101}{46,702,656,000}$	$\frac{-343,655,982,425,891}{46,702,656,000}$	$\frac{-38,450,763,316,993}{9,340,531,200}$	$\frac{-305,368,847,812,163}{46,702,656,000}$	$\frac{-209,388,842,757,121}{9,340,531,200}$	$\frac{-5,129,104,009,946,051}{46,702,656,000}$	$\frac{-29,387,187,771,747,941}{46,702,656,000}$
	1	$\frac{165,445,178,916,726,479}{653,837,184,000}$	$\frac{28,101,378,954,880,001}{653,837,184,000}$	$\frac{5,414,972,538,444,239}{653,837,184,000}$	$\frac{1,397,141,337,414,593}{653,837,184,000}$	$\frac{723,357,784,442,063}{653,837,184,000}$	$\frac{1,114,386,138,224,129}{653,837,184,000}$	$\frac{3,825,435,713,279,951}{653,837,184,000}$	$\frac{18,799,624,487,562,689}{653,837,184,000}$	$\frac{107,887,390,486,248,143}{653,837,184,000}$
	0	$\frac{-47,841,342,141,981,299}{1,307,674,368,000}$	$\frac{-7,906,584,673,048,973}{1,307,674,368,000}$	$\frac{-1,457,105,112,643,091}{1,307,674,368,000}$	$\frac{-350,067,382,006,253}{1,307,674,368,000}$	$\frac{-167,888,314,942,259}{1,307,674,368,000}$	$\frac{-253,674,820,236,749}{1,307,674,368,000}$	$\frac{-877,252,492,928,723}{1,307,674,368,000}$	$\frac{-4,331,747,069,079,341}{1,307,674,368,000}$	$\frac{-24,911,758,529,750,003}{1,307,674,368,000}$
4	4	$\frac{8,001,879,703,767,347}{7,472,424,960}$	$\frac{1,403,304,354,475,421}{7,472,424,960}$	$\frac{289,259,235,638,771}{7,472,424,960}$	$\frac{85,394,018,909,597}{7,472,424,960}$	$\frac{52,297,392,889,139}{7,472,424,960}$	$\frac{85,394,018,909,597}{7,472,424,960}$	$\frac{289,259,235,638,771}{7,472,424,960}$	$\frac{1,403,304,354,475,421}{7,472,424,960}$	$\frac{8,001,879,703,767,347}{7,472,424,960}$
	3	$\frac{-7,140,074,733,899,851}{3,736,212,480}$	$\frac{-6,230,647,138,120,121}{18,681,062,400}$	$\frac{-1,267,992,294,203,351}{18,681,062,400}$	$\frac{-72,310,955,346,373}{3,736,212,480}$	$\frac{-207,139,067,201,783}{18,681,062,400}$	$\frac{-63,811,818,908,581}{3,736,212,480}$	$\frac{-1,056,291,616,534,871}{18,681,062,400}$	$\frac{-5,091,060,727,437,401}{18,681,062,400}$	$\frac{-5,794,119,024,433,483}{3,736,212,480}$
	2	$\frac{228,786,920,178,433}{212,284,800}$	$\frac{39,564,077,889,589}{212,284,800}$	$\frac{7,883,820,528,109}{212,284,800}$	$\frac{2,145,005,788,633}{212,284,800}$	$\frac{1,143,576,251,161}{212,284,800}$	$\frac{1,679,094,624,733}{212,284,800}$	$\frac{5,489,435,141,989}{212,284,800}$	$\frac{26,403,598,814,209}{212,284,800}$	$\frac{150,205,347,326,833}{212,284,800}$
	1	$\frac{-46,020,384,090,357,023}{130,767,436,800}$	$\frac{-7,832,368,115,834,609}{130,767,436,800}$	$\frac{-1,512,744,281,500,799}{130,767,436,800}$	$\frac{-388,442,316,668,753}{130,767,436,800}$	$\frac{-192,310,346,872,991}{130,767,436,800}$	$\frac{-272,139,518,377,073}{130,767,436,800}$	$\frac{-886,173,785,909,759}{130,767,436,800}$	$\frac{-4,266,972,749,341,649}{130,767,436,800}$	$\frac{-24,293,471,434,588,703}{130,767,436,800}$
	0	$\frac{534,237,095,117,903}{10,461,394,944}$	$\frac{2,214,259,153,735,049}{261,534,873,600}$	$\frac{409,921,790,776,919}{261,534,873,600}$	$\frac{19,690,918,384,021}{52,306,974,720}$	$\frac{45,272,942,020,727}{261,534,873,600}$	$\frac{2,497,209,723,185}{10,461,394,944}$	$\frac{203,891,614,104,599}{261,534,873,600}$	$\frac{984,850,182,064,169}{261,534,873,600}$	$\frac{1,123,058,785,015,051}{52,306,974,720}$
3	3	$\frac{159,646,773,711,558,347}{186,810,624,000}$	$\frac{27,770,723,927,721,989}{186,810,624,000}$	$\frac{5,599,666,272,693,707}{186,810,624,000}$	$\frac{1,553,225,813,426,501}{186,810,624,000}$	$\frac{836,484,368,637,131}{186,810,624,000}$	$\frac{1,206,964,694,318,597}{186,810,624,000}$	$\frac{3,878,296,682,785,739}{186,810,624,000}$	$\frac{18,518,028,023,237,957}{186,810,624,000}$	$\frac{105,045,730,109,557,451}{186,810,624,000}$
	2	$\frac{-45,148,728,224,254,817}{46,702,656,000}$	$\frac{-7,795,675,329,471,191}{46,702,656,000}$	$\frac{-1,544,964,557,143,169}{46,702,656,000}$	$\frac{-411,721,854,332,951}{46,702,656,000}$	$\frac{-207,059,158,040,897}{46,702,656,000}$	$\frac{-282,622,107,973,367}{46,702,656,000}$	$\frac{-890,937,252,684,641}{46,702,656,000}$	$\frac{-4,234,862,610,936,119}{46,702,656,000}$	$\frac{-23,993,743,892,557,601}{46,702,656,000}$
	1	$\frac{207,178,084,258,860,569}{653,837,184,000}$	$\frac{35,272,568,778,872,279}{653,837,184,000}$	$\frac{1,359,891,017,166,853}{130,767,436,800}$	$\frac{1,720,297,891,825,367}{653,837,184,000}$	$\frac{161,084,839,253,509}{130,767,436,800}$	$\frac{1,051,238,439,516,119}{653,837,184,000}$	$\frac{3,281,427,995,720,729}{653,837,184,000}$	$\frac{3,116,380,997,521,963}{130,767,436,800}$	$\frac{88,287,149,743,355,417}{653,837,184,000}$
	0	$\frac{-12,083,632,055,537,503}{261,534,873,600}$	$\frac{-10,036,258,935,621,221}{1,307,674,368,000}$	$\frac{-1,859,899,247,394,491}{1,307,674,368,000}$	$\frac{-17,694,932,119,757}{52,306,974,720}$	$\frac{-192,700,060,973,723}{1,307,674,368,000}$	$\frac{-48,633,489,917,473}{261,534,873,600}$	$\frac{-757,402,017,640,571}{1,307,674,368,000}$	$\frac{-3,601,784,423,075,141}{1,307,674,368,000}$	$\frac{-816,990,037,454,483}{52,306,974,720}$
2	2	$\frac{4,660,712,172,178,939}{16,982,784,000}$	$\frac{800,572,672,346,869}{16,982,784,000}$	$\frac{156,622,544,328,763}{16,982,784,000}$	$\frac{40,385,614,392,181}{16,982,784,000}$	$\frac{19,010,310,966,523}{16,982,784,000}$	$\frac{24,324,934,655,989}{16,982,784,000}$	$\frac{74,730,821,653,819}{16,982,784,000}$	$\frac{352,812,369,719,413}{16,982,784,000}$	$\frac{1,994,952,741,927,931}{16,982,784,000}$
	1	$\frac{-59,111,412,950,734,301}{326,918,592,000}$	$\frac{-10,036,779,580,858,187}{326,918,592,000}$	$\frac{-1,918,610,096,603,357}{326,918,592,000}$	$\frac{-472,662,830,894,411}{326,918,592,000}$	$\frac{-207,359,252,612,669}{326,918,592,000}$	$\frac{-251,283,767,228,651}{326,918,592,000}$	$\frac{-759,598,480,120,637}{326,918,592,000}$	$\frac{-3,575,411,646,556,907}{326,918,592,000}$	$\frac{-20,204,125,377,340,061}{326,918,592,000}$
	0	$\frac{34,709,567,828,765,989}{1,307,674,368,000}$	$\frac{1,152,669,616,433,567}{261,534,873,600}$	$\frac{1,063,191,201,446,533}{1,307,674,368,000}$	$\frac{247,582,660,569,403}{1,307,674,368,000}$	$\frac{20,216,075,320,673}{261,534,873,600}$	$\frac{117,272,649,474,139}{1,307,674,368,000}$	$\frac{70,341,062,456,897}{261,534,873,600}$	$\frac{1,655,072,196,501,883}{1,307,674,368,000}$	$\frac{9,355,064,903,078,053}{1,307,674,368,000}$
1	1	$\frac{5,602,753,233,305,651}{186,810,624,000}$	$\frac{6,603,455,065,054,091}{1,307,674,368,000}$	$\frac{1,239,990,283,564,133}{1,307,674,368,000}$	$\frac{293,675,114,165,963}{1,307,674,368,000}$	$\frac{119,979,314,906,981}{1,307,674,368,000}$	$\frac{136,155,780,967,307}{1,307,674,368,000}$	$\frac{402,355,798,141,541}{1,307,674,368,000}$	$\frac{269,247,491,159,069}{186,810,624,000}$	$\frac{10,637,354,815,456,613}{1,307,674,368,000}$
	0	$\frac{-894,628,364,420,801}{100,590,336,000}$	$\frac{-147,809,125,548,479}{100,590,336,000}$	$\frac{-3,844,139,848,343}{14,370,048,000}$	$\frac{-6,056,041,731,167}{100,590,336,000}$	$\frac{-2,297,804,363,777}{100,590,336,000}$	$\frac{-2,466,233,185,151}{100,590,336,000}$	$\frac{-1,026,441,378,647}{14,370,048,000}$	$\frac{-33,593,572,337,951}{100,590,336,000}$	$\frac{-189,555,672,759,617}{100,590,336,000}$
0	0	$\frac{109,471,139,332,699}{163,459,296,000}$	$\frac{17,848,737,251,203}{163,459,296,000}$	$\frac{3,165,355,170,121}{163,459,296,000}$	$\frac{679,328,101,453}{163,459,296,000}$	$\frac{238,114,846,399}{163,459,296,000}$	$\frac{238,114,846,399}{163,459,296,000}$	$\frac{679,328,101,453}{163,459,296,000}$	$\frac{3,165,355,170,121}{163,459,296,000}$	$\frac{17,848,737,251,203}{163,459,296,000}$

Obviously (2) $f(x)$ are cell-averages [12] of $h(x)$. In practice $h(x+\frac{1}{2}\Delta x)$ is approximated by polynomials of degree M, $p_{h,i+\frac{1}{2}}(x,x_i,\Delta x)$

$$h(x) \approxeq p_{h,i+\frac{1}{2}}(x,x_i,\Delta x) := \sum_{m=0}^{M} c_{h_{m,i+\frac{1}{2}}} \left(\frac{x-x_i}{\Delta x}\right)^m \overset{(2)}{\Rightarrow} \tag{3a}$$

$$f(x) \approxeq p_{f,i+\frac{1}{2}}(x,x_i,\Delta x) := \frac{1}{\Delta x}\int_{x-\frac{1}{2}\Delta x}^{x+\frac{1}{2}\Delta x} p_{h,i+\frac{1}{2}}(\xi,x_i,\Delta x)\, d(\xi - x_i) \Rightarrow \tag{3b}$$

$$f(x) \approxeq p_{f,i+\frac{1}{2}}(x,x_i,\Delta x) = \sum_{m=0}^{M} \frac{c_{h_{m,i+\frac{1}{2}}}}{m+1}\left[\left(\frac{x-x_i}{\Delta x}+\frac{1}{2}\right)^{m+1} - \left(\frac{x-x_i}{\Delta x}-\frac{1}{2}\right)^{m+1}\right] \tag{3c}$$

and the $M+1$ coefficients $c_{h_{m,i+\frac{1}{2}}}$ $(m=0,\ldots,M)$ are computed by equating $p_{f,i+\frac{1}{2}}(x,x_i,\Delta x)$ (3c) to known values $f_{i+\ell}$, at the points of an appropriately selected stencil

$$\mathsf{s}_{i,M_-,M_+} := \{i-M_-,\ldots,i+M_+\}; \quad M_- + M_+ = M; \quad M_- \geqslant 0; \quad M_+ \geqslant 0 \tag{4}$$

resulting in an $(M+1)\times(M+1)$ linear system

$$\begin{aligned} f_{i-M_-} &= p_{f,i+\frac{1}{2}}(x_i - M_-\Delta x) \\ &\vdots \\ f_{i+M_+} &= p_{f,i+\frac{1}{2}}(x_i + M_+\Delta x) \end{aligned} \tag{5}$$

with a similar system for the coefficients $c_{h_{m,i-\frac{1}{2}}}$ $(m=0,\ldots,M)$ of the polynomial $p_{h,i-\frac{1}{2}}(x,x_{i-1},\Delta x)$ approximating $h(x-\frac{1}{2}\Delta x)$ on the shifted stencil $\mathsf{s}_{i-1,M_-,M_+} = [i-1-M_-,\ldots,i-1+M_+]$. For $M_-+M_+=M$, these polynomials approximate $h(x)$ to $O(\Delta x^{M+1})$ [23,27].

2.2. Upwind scheme

The family of upwind (UW) schemes (more precisely upwind-biased schemes) is constructed [1,2,14,3,4] by choosing $M_- = M_+ = r-1$ in the definition of the stencil (4), i.e. $M = M_- + M_+ = 2r-2$. Straightforward application of (5) yields the coefficients $c_{r,\mathrm{UW},m,i+\frac{1}{2}}$ $(m=0,\ldots,2r-2)$ of the polynomial $p_{r,\mathrm{UW},i+\frac{1}{2}}(x,x_i,\Delta x)$, with similar i-shifted relations for the polynomial $p_{r,\mathrm{UW},i-\frac{1}{2}}(x,x_{i-1},\Delta x)$. Evaluation of $f^{\mathrm{L}}_{r,\mathrm{UW},i+\frac{1}{2}} := p_{r,\mathrm{UW},i+\frac{1}{2}}(x_i+\frac{1}{2}\Delta x, x_i, \Delta x)$ and $f^{\mathrm{L}}_{r,\mathrm{UW},i-\frac{1}{2}} := p_{r,\mathrm{UW},i-\frac{1}{2}}(x_i-\frac{1}{2}\Delta x, x_{i-1}, \Delta x)$ yields the left reconstructed values $f^{\mathrm{L}}_{r,\mathrm{UW},i\pm\frac{1}{2}}$ in the form

$$f^{\mathrm{L}}_{r,\mathrm{UW},i+\frac{1}{2}} = \sum_{\ell=-(r-1)}^{(r-1)} a_{r,\mathrm{UW},\ell} f_{i+\ell} \tag{6}$$

The coefficients $a_{r,\mathrm{UW},\ell}$ were given by Jiang and Shu [2] for $r=2,3$, and by Balsara and Shu [3] for $r=4,5,6$. They were also computed in the present work for $r=7,8,9$, and tabulated (Table 1). Straightforward Taylor-expansions, in regions where $f(x)$ is smooth, yield [1,2,14,3,4]

$$f^{\mathrm{L}}_{r,\mathrm{UW},i\pm\frac{1}{2}} = h\left(x_i \pm \frac{1}{2}\Delta x\right) + A_{r,\mathrm{UW},2r-1} \left.\frac{d^{2r-1}h}{dx^{2r-1}}\right|_{x_{i\pm\frac{1}{2}}} \Delta x^{2r-1} + O(\Delta x^{2r}) \tag{7a}$$

$$\frac{f^{\mathrm{L}}_{r,\mathrm{UW},i+\frac{1}{2}} - f^{\mathrm{L}}_{r,\mathrm{UW},i-\frac{1}{2}}}{\Delta x} = f'(x_i) + A_{r,\mathrm{UW},2r-1}\left.\frac{d^{2r}f}{dx^{2r}}\right|_{x_i} \Delta x^{2r-1} + O(\Delta x^{2r}) \tag{7b}$$

where $A_{r,\mathrm{UW},m}$ $(m \geqslant 2r-1)$ are constants [27]. Because of the order-of-accuracy relation (7b) the UW scheme obtained using $M_- = M_+ = r-1$ is called UW$(2r-1)$ [2,14,3,4]. The expression for the R-reconstructions at $i-\frac{1}{2}$ (corresponding to information propagating in the $(-x)$-direction) are obtained from the L-reconstructions at $i+\frac{1}{2}$ (corresponding to information propagating in the (+x)-direction) by applying to (6) symmetry with respect to the point i [2,14]

$$f^{\mathrm{R}}_{r,\mathrm{UW},i-\frac{1}{2}} = \sum_{\ell=-(r-1)}^{(r-1)} a_{r,\mathrm{UW},\ell} f_{i-\ell} \tag{8a}$$

$$f^{\mathrm{R}}_{r,\mathrm{UW},i+\frac{1}{2}} = \sum_{\ell=-(r-1)}^{(r-1)} a_{r,\mathrm{UW},\ell} f_{i-\ell+1} = \sum_{\ell=-(r-2)}^{r} a_{r,\mathrm{UW},1-\ell} f_{i+\ell} \tag{8b}$$

2.3. WENO reconstruction

2.3.1. Stencils

The UW reconstructions (6) work well for smooth flows [31], but, being linear, they do not ensure monotonicity for flows with shock-waves or other discontinuities, as expected from the Godunov theorem [32]. In the presence of discontinuities, they must be replaced by nonlinear reconstructions [33,32]. The WENO$(2r-1)$ approach [1,2,14,3,4] achieves this by computing the reconstructed value as a weighted convex (positive weights) combination of r linear reconstructions

$$f^{\mathrm{L}}_{r,k_s,i+\frac{1}{2}} = \sum_{\ell=0}^{(r-1)} a_{r,k_s,\ell} f_{i+k_s-\ell}; \quad k_s = 0,\ldots,(r-1) \tag{9}$$

obtained on r different stencils (4)

$$\mathrm{s}_{i,r-1-k_s,k_s} = \{i+k_s-(r-1),\ldots,i+k_s\}; \quad k_s = 0,\ldots,(r-1) \tag{10a}$$

$$\bigcup_{k_s=0}^{r-1} \mathrm{s}_{i,r-1-k_s,k_s} = \mathrm{s}_{i,r-1,r-1} \tag{10b}$$

whose union (10b) is the stencil corresponding to the UW$(2r-1)$ scheme (6). The reconstructed value $f^{\mathrm{L}}_{r,k_s,i+\frac{1}{2}}$ is obtained following (5), with $M_- = r-1-k_s$ and $M_+ = k_s$, to define polynomials $p_{r,k_s,i+\frac{1}{2}}(x,x_i,\Delta x)$ of degree $r-1$, which are evaluated at $x_i + \frac{1}{2}\Delta x$ to give $f^{\mathrm{L}}_{r,k_s,i+\frac{1}{2}}$ (9). The coefficients $a_{r,k_s,\ell}$ were given by Jiang and Shu [2] for $r = 2,3$, and by Balsara and Shu [3] for $r = 4,5,6$. They were also computed in the present work for $r = 7,8,9$, and tabulated (Table 2). Straightforward Taylor-expansions, in regions where $f(x)$ is smooth, yield [1,2,14,3,4]

$$f^{\mathrm{L}}_{r,k_s,i+\frac{1}{2}} = h(x_i + \frac{1}{2}\Delta x) + \sum_{m=r}^{\infty} A_{r,k_s,m} \left.\frac{d^m h}{dx^m}\right|_{x_{i+\frac{1}{2}}} \Delta x^m \tag{11a}$$

$$\frac{f^{\mathrm{L}}_{r,k_s,i+\frac{1}{2}} - f^{\mathrm{L}}_{r,k_s,i-\frac{1}{2}}}{\Delta x} = f'(x_i) + \sum_{m=r}^{2r-2} A_{r,k_s,m} \left.\frac{d^{m+1} f}{dx^{m+1}}\right|_{x_i} \Delta x^m + A_{r,k_s,2r-1} \left.\frac{d^{2r} f}{dx^{2r}}\right|_{x_i} \Delta x^{2r-1} + O(\Delta x^{2r}) \tag{11b}$$

where $A_{r,k_s,m}$ are tabulated constants.

Nonlinearity, necessary for monotonicity, is introduced in the definition of the weights $\omega_{r,k_s,i+\frac{1}{2}}$

$$f^{\mathrm{L}}_{r,\mathrm{WENO},i+\frac{1}{2}} = \sum_{k_s=0}^{(r-1)} \omega_{r,k_s,i+\frac{1}{2}} f^{\mathrm{L}}_{r,k_s,i+\frac{1}{2}} \tag{12a}$$

$$\sum_{k_s=0}^{(r-1)} \omega_{r,k_s,i+\frac{1}{2}} = 1 \tag{12b}$$

$$\omega_{r,k_s,i+\frac{1}{2}} \geqslant 0 \quad \forall k_s \in \{0,\ldots,r-1\} \tag{12c}$$

which are given in Sections 2.3.4 and 2.3.5.

2.3.2. Optimal weights

The Taylor-expansions (11) for the evaluation of $f'(x)$ with the reconstructed values of each of the r stencils (10) can be *linearly* combined, with constant weights C_{r,k_s} to eliminate the terms of order less than $O(\Delta x^{2r-1})$

$$\begin{aligned} &\sum_{k_s=0}^{r-1} C_{r,k_s} A_{r,k_s,r} = 0 \\ &\qquad\vdots \\ &\sum_{k_s=0}^{r-1} C_{r,k_s} A_{r,k_s,2r-2} = 0 \\ &\sum_{k_s=0}^{r-1} C_{r,k_s} = 1 \end{aligned} \tag{13}$$

where the first $r-1$ equations are supplemented by the requirement that the weights sum up to 1. The resulting combination of the reconstructions of the r stencils is exactly equal to the upwind reconstruction (6) [1,2,14,3,4].

$$f^{\mathrm{L}}_{r,\mathrm{UW},i+\frac{1}{2}} = \sum_{k_s=0}^{(r-1)} C_{r,k_s} f^{\mathrm{L}}_{r,k_s,i+\frac{1}{2}} \tag{14}$$

The coefficients $C_{r,k_s} > 0$ were given by Jiang and Shu [2] for $r = 2,3$, and by Balsara and Shu [3] for $r = 4,5,6$. They were also computed in the present work for $r = 7,8,9$, and tabulated (Table 3).

The positive linear weights C_{r,k_s} combine the reconstructions of the r stencils, to give the upwind reconstruction (6), and thus achieve the highest possible accuracy of $O(\Delta x^{2r-1})$. For this reason they are usually called optimal weights [1,2,14,3,4]. Notice that C_{r,k_s} are constants, and thus do not depend on $i+\frac{1}{2}$ contrary to the nonlinear weights $\omega_{r,k_s,i\pm\frac{1}{2}}$ (in general

$\omega_{r,k_s,i+\frac{1}{2}} \neq \omega_{r,k_s,i-\frac{1}{2}}$). Nonlinear weights ω_{r,k_s} are designed to approach as closely as possible the optimal weights C_{r,k_s}, in regions where $f(x)$ is smooth, and thus to achieve the accuracy of the corresponding UW$(2r-1)$ scheme (7b).

2.3.3. Smoothness indicators

The WENO procedure requires a measure of smoothness to compare the r stencils which are combined to obtain the reconstructed value. Invariably [2,3,5,4,6,7], the smoothness indicators introduced by Jiang and Shu [2] are used. They are defined as

$$\beta_{r,k_s,i+\frac{1}{2}} := \sum_{m=1}^{r-1} \Delta x^{2m-1} \int_{-\frac{1}{2}\Delta x}^{+\frac{1}{2}\Delta x} \left[\frac{d^m}{d\xi^m} p_{r,k_s,i+\frac{1}{2}}\right]^2 d(\xi - x_i) \tag{15}$$

and are a continuous measure of the smoothness of all the derivatives approximated by $p_{r,k_s,i+\frac{1}{2}}$, i.e. up to degree $r-1$. Substitution of the expressions for the coefficients $c_{h,r,k_s,m,i+\frac{1}{2}}$ as linear combinations of the values of $f_{i+\ell}$ in each stencil $\mathsf{s}_{i,r-1-k_s,k_s}$ (10) yields

$$\beta_{r,k_s,i+\frac{1}{2}} = \sum_{\ell=0}^{(r-1)} \sum_{m=0}^{\ell} \sigma_{r,k_s,\ell,m} f_{i+k_s-\ell} f_{i+k_s-m} \geqslant 0 \tag{16}$$

The constant coefficients $\sigma_{r,k_s,\ell,m}$ were given by Jiang and Shu [2] for $r = 2, 3$, and by Balsara and Shu [3] for $r = 4, 5, 6$. They were also computed and tabulated in the present work for $r = 7$ (WENO13, Table 4), $r = 8$ (WENO15, Table 5), $r = 9$ (WENO17, Table 6).

2.3.4. Jiang–Shu nonlinear weights

The nonlinear weights are computed as

$$\omega_{\mathrm{JS},r,k_s,i+\frac{1}{2}} = \frac{\alpha_{\mathrm{JS},r,k_s,i+\frac{1}{2}}}{\sum_{m_s=0}^{(r-1)} \alpha_{\mathrm{JS},r,m_s,i+\frac{1}{2}}} \tag{17a}$$

$$\alpha_{\mathrm{JS},r,k_s,i+\frac{1}{2}} = \frac{C_{r,k_s}}{\epsilon_\beta + \left(\beta_{r,k_s,i+\frac{1}{2}}\right)^{p_\beta}} \tag{17b}$$

The influence of the parameter ϵ_β, used to avoid division by 0 (Eq. (17b)), is examined in detail by Henrick et al. [4], who showed the ϵ_β must be small enough for the theoretical WENO$(2r-1)$ order-of-accuracy relations (Section 2.3.6) to be valid. In the present work we used the intrinsic FORTRAN95 function $\mathtt{tiny}(\beta_{r,k_s})$, which gives the smallest computer-representable value of variables of $\mathtt{kind}(\beta_{r,k_s})$. Notice that ϵ_β is added to $\left(\beta_{r,k_s,i+\frac{1}{2}}\right)^{p_\beta}$ (17b), in lieu of the usual expression $\left(\epsilon_\beta + \beta_{r,k_s,i+\frac{1}{2}}\right)^{p_\beta}$ [2–4]. The appropriate value of the exponent p_β is discussed in Section 3.3.

2.3.5. WENOM

Recently, Henrick et al. [4] have undertaken a thorough study of the performance and effective order of WENO schemes. The basic nonlinear mechanism in the WENO reconstruction (nonlinear weights $\omega_{r,k_s,i+\frac{1}{2}}$) modifies the optimal weights (C_{r,k_s}) to bias the convex combination of stencils (12) toward the smoother stencils, removing as much as possible stencils containing discontinuities of the solution [2,3]. Henrick et al. [4] demonstrated that the increased numerical dissipation, associated with the departure of the Jiang–Shu nonlinear weights $\omega_{\mathrm{JS},r,k_s,i+\frac{1}{2}}$ from the optimal weights C_{r,k_s}, can be reduced by using mapped nonlinear weights, through a mapping function $g_{\mathrm{M}}(\omega, C)$, which delays the departure of $\omega_{r,k_s,i+\frac{1}{2}}$ from the optimal value of C_{r,k_s}. The weights of the resulting WENOM scheme read [4]

$$\omega_{\mathrm{MJS},r,k_s,i+\frac{1}{2}} = \frac{\alpha_{\mathrm{MJS},r,k_s,i+\frac{1}{2}}}{\sum_{m_s=0}^{(r-1)} \alpha_{\mathrm{MJS},r,m_s,i+\frac{1}{2}}} \tag{18a}$$

$$\alpha_{\mathrm{MJS},r,k_s,i+\frac{1}{2}} = g_{\mathrm{M}}\left(\omega_{\mathrm{JS},r,k_s,i+\frac{1}{2}}, C_{r,k_s}\right) \tag{18b}$$

$$g_{\mathrm{M}}(\omega, C) := \frac{\omega(C + C^2 - 3C\omega + \omega^2)}{C^2 + \omega(1 - 2C)} \tag{18c}$$

where the $\omega_{\mathrm{JS},r,k_s,i+\frac{1}{2}}$ are the Jiang–Shu [2] nonlinear weights (17) of the corresponding WENO$(2r-1)$ scheme.

2.3.6. Taylor-expansions and order-of-accuracy

Sufficient conditions for the WENO$(2r-1)$ scheme to be effectively $O(\Delta x^{2r-1})$, when $f(x)$ is smooth over all of the stencils $\mathsf{s}_{i,r-1-k_s,k_s}$ (10), are given by Jiang and Shu [2], Henrick et al. [4] and Borges et al. [7]. Combining (12) and (14) yields

$$\frac{f^{\mathrm{L}}_{r,\mathrm{WENO},i+\frac{1}{2}} - f^{\mathrm{L}}_{r,\mathrm{WENO},i-\frac{1}{2}}}{\Delta x} = \frac{f^{\mathrm{L}}_{r,\mathrm{UW},i+\frac{1}{2}} - f^{\mathrm{L}}_{r,\mathrm{UW},i-\frac{1}{2}}}{\Delta x} + \frac{1}{\Delta x}\left\{\sum_{k_s=0}^{r-1}\left(\left(\omega_{r,k_s,i+\frac{1}{2}} - C_{r,k_s}\right) f^{\mathrm{L}}_{r,k_s,i+\frac{1}{2}}\right) - \sum_{k_s=0}^{r-1}\left(\left(\omega_{r,k_s,i-\frac{1}{2}} - C_{r,k_s}\right) f^{\mathrm{L}}_{r,k_s,i-\frac{1}{2}}\right)\right\} \tag{19}$$

and using the order-of-accuracy relations (7) and (11)

$$\begin{aligned}\frac{f^{\mathrm{L}}_{r,\mathrm{WENO},i+\frac{1}{2}}-f^{\mathrm{L}}_{r,\mathrm{WENO},i-\frac{1}{2}}}{\Delta x} &= f'(x_i)+O(\Delta x^{2r-1})+\frac{1}{\Delta x}\left\{\sum_{k_s=0}^{r-1}\left[\left(\omega_{r,k_s,i+\frac{1}{2}}-C_{r,k_s}\right)\left(h\left(x_i+\frac{1}{2}\Delta x\right)+\sum_{m=r}^{\infty}A_{r,k_s,m}\frac{d^m h}{dx^m}\bigg|_{x_{i+\frac{1}{2}}}\Delta x^m\right)\right]\right.\\
&\left.\quad-\sum_{k_s=0}^{r-1}\left[\left(\omega_{r,k_s,i-\frac{1}{2}}-C_{r,k_s}\right)\left(h\left(x_i-\frac{1}{2}\Delta x\right)+\sum_{m=r}^{\infty}A_{r,k_s,m}\frac{d^m h}{dx^m}\bigg|_{x_{i-\frac{1}{2}}}\Delta x^m\right)\right]\right\}\\
&= f'(x_i)+O(\Delta x^{2r-1})+\frac{1}{\Delta x}\left\{\left(\sum_{k_s=0}^{r-1}\omega_{r,k_s,i+\frac{1}{2}}-\sum_{k_s=0}^{r-1}C_{r,k_s}\right)h\left(x_i+\frac{1}{2}\Delta x\right)\right.\\
&\left.\quad-\left(\sum_{k_s=0}^{r-1}\omega_{r,k_s,i-\frac{1}{2}}-\sum_{k_s=0}^{r-1}C_{r,k_s}\right)h\left(x_i-\frac{1}{2}\Delta x\right)\right\}+\frac{1}{\Delta x}\left\{\sum_{k_s=0}^{r-1}\left[\left(\omega_{r,k_s,i+\frac{1}{2}}-C_{r,k_s}\right)\left(\sum_{m=r}^{\infty}A_{r,k_s,m}\frac{d^m h}{dx^m}\bigg|_{x_{i+\frac{1}{2}}}\Delta x^m\right)\right]\right.\\
&\left.\quad-\sum_{k_s=0}^{r-1}\left[\left(\omega_{r,k_s,i-\frac{1}{2}}-C_{r,k_s}\right)\left(\sum_{m=r}^{\infty}A_{r,k_s,m}\frac{d^m h}{dx^m}\bigg|_{x_{i-\frac{1}{2}}}\Delta x^m\right)\right]\right\}\end{aligned}\tag{20}$$

and since both the nonlinear (12b) and the optimal (13) weights sum up to 1

$$\begin{aligned}\frac{f^{\mathrm{L}}_{r,\mathrm{WENO},i+\frac{1}{2}}-f^{\mathrm{L}}_{r,\mathrm{WENO},i-\frac{1}{2}}}{\Delta x} &= f'(x_i)+O(\Delta x^{2r-1})+\sum_{k_s=0}^{r-1}\left[\left(\omega_{r,k_s,i+\frac{1}{2}}-C_{r,k_s}\right)\left(\sum_{m=r}^{\infty}A_{r,k_s,m}\frac{d^m h}{dx^m}\bigg|_{x_{i+\frac{1}{2}}}\Delta x^{m-1}\right)\right]\\
&\quad-\sum_{k_s=0}^{r-1}\left[\left(\omega_{r,k_s,i-\frac{1}{2}}-C_{r,k_s}\right)\left(\sum_{m=r}^{\infty}A_{r,k_s,m}\frac{d^m h}{dx^m}\bigg|_{x_{i-\frac{1}{2}}}\Delta x^{m-1}\right)\right]\end{aligned}\tag{21}$$

Obviously, keeping in mind that, in general, $\omega_{r,k_s,i+\frac{1}{2}}\neq\omega_{r,k_s,i-\frac{1}{2}}$, sufficient conditions for the WENO scheme to approximate f' to $O(\Delta x^{2r-1})$ are

$$\omega_{r,k_s,i\pm\frac{1}{2}}-C_{r,k_s}=O(\Delta x^r)\quad\forall k_s\tag{22}$$

Jiang and Shu [2] demonstrated that sufficient conditions for the WENO scheme to approximate f' to $O(\Delta x^{2r-1})$ are verified by considering Taylor-expansions of the smoothness indicators $\beta_{r,k_s,i+\frac{1}{2}}$, and requiring [2] that

$$\beta_{r,k_s,i+\frac{1}{2}}=D_{\beta_{r,i+\frac{1}{2}}}(1+O(\Delta x^{r-1}))\tag{23}$$

where $D_{\beta_{r,i+\frac{1}{2}}}(f'(x_i),f''(x_i),\ldots;\Delta x)$ is independent of k_s (the same for all stencils) at fixed r (for a given order).

Straightforward formal calculus (which was performed using Maxima [34]), shows that the results for the Taylor-expansions of $\beta_{r,k_s,i+\frac{1}{2}}$ can be given in a very simple form

$$\mathrm{T}\left(\beta_{2,k_s,i+\frac{1}{2}}\right)=Q_{\beta_2}\Delta x^2+B_{\beta_{2,k_s}}\left[\frac{df}{dx}\frac{d^2f}{dx^2}\right]_{x=x_i}\Delta x^3+O(\Delta x^4)\tag{24a}$$

$$\mathrm{T}\left(\beta_{3,k_s,i+\frac{1}{2}}\right)=Q_{\beta_2}\Delta x^2+Q_{\beta_4}\Delta x^4+B_{\beta_{3,k_s}}\left[\frac{df}{dx}\frac{d^3f}{dx^3}\right]_{x=x_i}\Delta x^4+O(\Delta x^5)\tag{24b}$$

$$\mathrm{T}\left(\beta_{4,k_s,i+\frac{1}{2}}\right)=Q_{\beta_2}\Delta x^2+Q_{\beta_4}\Delta x^4+B_{\beta_{4,k_s}}\left[\frac{df}{dx}\frac{d^4f}{dx^4}\right]_{x=x_i}\Delta x^5+O(\Delta x^6)\tag{24c}$$

$$\mathrm{T}\left(\beta_{5,k_s,i+\frac{1}{2}}\right)=Q_{\beta_2}\Delta x^2+Q_{\beta_4}\Delta x^4+Q_{\beta_6}\Delta x^6+B_{\beta_{5,k_s}}\left[\frac{df}{dx}\frac{d^5f}{dx^5}\right]_{x=x_i}\Delta x^6+O(\Delta x^7)\tag{24d}$$

$$\mathrm{T}\left(\beta_{6,k_s,i+\frac{1}{2}}\right)=Q_{\beta_2}\Delta x^2+Q_{\beta_4}\Delta x^4+Q_{\beta_6}\Delta x^6+B_{\beta_{6,k_s}}\left[\frac{df}{dx}\frac{d^6f}{dx^6}\right]_{x=x_i}\Delta x^7+O(\Delta x^8)\tag{24e}$$

$$\mathrm{T}\left(\beta_{7,k_s,i+\frac{1}{2}}\right)=Q_{\beta_2}\Delta x^2+Q_{\beta_4}\Delta x^4+Q_{\beta_6}\Delta x^6+Q_{\beta_8}\Delta x^8+B_{\beta_{7,k_s}}\left[\frac{df}{dx}\frac{d^7f}{dx^7}\right]_{x=x_i}\Delta x^8+O(\Delta x^9)\tag{24f}$$

$$\mathrm{T}\left(\beta_{8,k_s,i+\frac{1}{2}}\right)=Q_{\beta_2}\Delta x^2+Q_{\beta_4}\Delta x^4+Q_{\beta_6}\Delta x^6+Q_{\beta_8}\Delta x^8+B_{\beta_{8,k_s}}\left[\frac{df}{dx}\frac{d^8f}{dx^8}\right]_{x=x_i}\Delta x^9+O(\Delta x^{10})\tag{24g}$$

$$\mathrm{T}\left(\beta_{9,k_s,i+\frac{1}{2}}\right)=Q_{\beta_2}\Delta x^2+Q_{\beta_4}\Delta x^4+Q_{\beta_6}\Delta x^6+Q_{\beta_8}\Delta x^8+Q_{\beta_{10}}\Delta x^{10}+B_{\beta_{9,k_s}}\left[\frac{df}{dx}\frac{d^9f}{dx^9}\right]_{x=x_i}\Delta x^{10}+O(\Delta x^{11})\tag{24h}$$

or in more compact form

$$\mathrm{T}\left(\beta_{r,k_s,i+\frac{1}{2}}\right) = \sum_{\ell=1}^{\lfloor\frac{r+1}{2}\rfloor} Q_{\beta_{2\ell}}(x_i)\Delta x^{2\ell} + B_{\beta_{r,k_s}}\left[\frac{df}{dx}\frac{d^rf}{dx^r}\right]_{x=x_i}\Delta x^{r+1} + O(\Delta x^{r+2});\quad k_s = 0,\ldots,r-1;\quad r = 2,\ldots,9 \tag{25}$$

where all the derivatives are evaluated at $x = x_i$, and

$$Q_{\beta_2}(x) = \left[\left(\frac{df}{dx}\right)^2\right] \tag{26a}$$

$$Q_{\beta_4}(x) = \left[\frac{13}{12}\left(\frac{d^2f}{dx^2}\right)^2\right] \tag{26b}$$

$$Q_{\beta_6}(x) = \left[\frac{781}{720}\left(\frac{d^3f}{dx^3}\right)^2 - \frac{1}{360}\frac{d^2f}{dx^2}\frac{d^4f}{dx^4}\right] \tag{26c}$$

$$Q_{\beta_8}(x) = \left[\frac{32,803}{30,240}\left(\frac{d^4f}{dx^4}\right)^2 - \frac{43}{15,120}\frac{d^3f}{dx^3}\frac{d^5f}{dx^5} + \frac{1}{15,120}\frac{d^2f}{dx^2}\frac{d^6f}{dx^6}\right] \tag{26d}$$

$$Q_{\beta_{10}}(x) = \left[\frac{1,312,121}{1,209,600}\left(\frac{d^5f}{dx^5}\right)^2 - \frac{1721}{604,800}\frac{d^4f}{dx^4}\frac{d^6f}{dx^6} + \frac{41}{604,800}\frac{d^3f}{dx^3}\frac{d^7f}{dx^7} - \frac{1}{604,800}\frac{d^2f}{dx^2}\frac{d^8f}{dx^8}\right] \tag{26e}$$

Obviously, the common part ($\forall k_s, r$fixed), at a regular point ($f'(x_i) \neq 0$) is

$$D_{\beta_{r,i+\frac{1}{2}}} := \sum_{\ell=1}^{\lfloor\frac{r+1}{2}\rfloor} Q_{\beta_{2\ell}}(x_i)\Delta x^{2\ell} \tag{27}$$

and condition (23) is verified, at points where $f' \neq 0$. Henrick et al. [4] and Borges et al. [7] further investigate the order relations for the WENO5 scheme. The complete evaluation of the order relations for the WENO$(2r-1)$ scheme can be obtained by making full asymptotic expansions of the WENO reconstruction (12).

Notice, however, that observation of the Taylor-expansions of $\beta_{r,k_s,i+\frac{1}{2}}$ (24) or of the general relation (25), reveals a difference between the cases r even or odd. Indeed, for r odd, the common part $D_{\beta_{r,i+\frac{1}{2}}}$ includes terms up to $O(\Delta x^{r+1})$, the differences $\beta_{r,k_s,i+\frac{1}{2}} - \beta_{r,m_s,i+\frac{1}{2}}$ $(k_s \neq m_s)$ being $O(\Delta x^{r+1})$. On the other hand, for r even, the common part includes terms up to $O(\Delta x^r)$, the differences $\beta_{r,k_s,i+\frac{1}{2}} - \beta_{r,m_s,i+\frac{1}{2}}$ $(k_s \neq m_s)$ being $O(\Delta x^{r+1})$. Furthermore, closer examination of the coefficients $B_{\beta_{r,k_s}}$ of the leading term of the noncommon part (Table 7), suggests that

$$B_{\beta_{r,k_s}} = (-1)^{r-1}B_{\beta_{r,r-1-k_s}};\quad k_s = 0,\ldots,r-1;\quad r = 2,\ldots,9 \tag{28}$$

The above observations were exploited, in the particular case $r = 3$, by Borges et al. [7], to develop the WENOZ5 nonlinear weights.

2.4. Boundary treatment

In the neighbourhood of the boundaries of the computational domain there are not enough points for the reconstruction stencils used (Eqs. (6), (8), (9), (12), (16) and (17)). At these nodes, the reconstruction-order is progressively reduced (when points in the stencil are not available) down to the UW1 scheme (for nodes where the UW1 stencil points are not available, a simple linear extrapolation procedure is used [35]).

Periodicity-boundaries and/or interfaces between grid-domains, are treated using a phantom-nodes technique, i.e. by adding phantom-nodes corresponding to actual grid-nodes of the neighbouring domain. The number of phantom nodes was determined by requiring that the grid-node at the boundary should have a complete discretization stencil. This implies, that the UW$(2r-1)$ or the WENOM$(2r-1)$ schemes, which use an $[i-r, i+r]$ stencil at point i, require $N_{\text{PH}} = r$ phantom nodes

$$\begin{aligned}
r &= 2;\quad \text{UW03}:\quad N_{\text{PH}} = 2\\
r &= 3;\quad \text{UW05}:\quad N_{\text{PH}} = 3\\
r &= 4;\quad \text{UW07}:\quad N_{\text{PH}} = 4\\
r &= 5;\quad \text{UW09}:\quad N_{\text{PH}} = 5\\
r &= 6;\quad \text{UW11}:\quad N_{\text{PH}} = 6\\
r &= 7;\quad \text{UW13}:\quad N_{\text{PH}} = 7\\
r &= 8;\quad \text{UW15}:\quad N_{\text{PH}} = 8\\
r &= 9;\quad \text{UW17}:\quad N_{\text{PH}} = 9
\end{aligned} \tag{29}$$

Table 7

Coefficients $B_{\beta_{r,k_s}}$ in the Taylor-expansions of the Jiang–Shu [2] smoothness indicators $\beta_{r,k_s,i+\frac{1}{2}}$ (16), for $r = 2, \ldots, 9$ (WENO3,…,WENO17), up to the lowest order for which $\mathrm{T}\left(\beta_{r,k_s,i+\frac{1}{2}}\right) \neq \mathrm{T}\left(\beta_{r,\ell_s,i+\frac{1}{2}}\right)$ ($k_s \neq \ell_s$), at a regular point ($f' \neq 0$).

k_s	$r = 9$	$r = 8$	$r = 7$	$r = 6$	$r = 5$	$r = 4$	$r = 3$	$r = 2$
	$B_{\beta_{r,k_s}}$							
0	$-\frac{2}{9}$	$-\frac{1}{4}$	$-\frac{2}{7}$	$-\frac{1}{3}$	$-\frac{2}{5}$	$-\frac{1}{2}$	$-\frac{2}{3}$	-1
1	$+\frac{1}{36}$	$+\frac{1}{28}$	$+\frac{1}{21}$	$+\frac{1}{15}$	$+\frac{1}{10}$	$+\frac{1}{6}$	$+\frac{1}{3}$	+1
2	$-\frac{1}{126}$	$-\frac{1}{84}$	$-\frac{2}{105}$	$-\frac{1}{30}$	$-\frac{1}{15}$	$-\frac{1}{6}$	$-\frac{2}{3}$	
3	$+\frac{1}{252}$	$+\frac{1}{140}$	$+\frac{1}{70}$	$+\frac{1}{30}$	$+\frac{1}{10}$	$+\frac{1}{2}$		
4	$-\frac{1}{315}$	$-\frac{1}{140}$	$-\frac{2}{105}$	$-\frac{1}{15}$	$-\frac{2}{5}$			
5	$+\frac{1}{252}$	$+\frac{1}{84}$	$+\frac{1}{21}$	$+\frac{1}{3}$				
6	$-\frac{1}{126}$	$-\frac{1}{28}$	$-\frac{2}{7}$					
7	$+\frac{1}{36}$	$+\frac{1}{4}$						
8	$-\frac{2}{9}$							

3. Basic results for the advection equation

3.1. The advection equation with periodic boundary-conditions

We study the advection equation [1–4]

$$\frac{\partial u}{\partial t} + \frac{\partial u}{\partial x} = 0; \quad x \in [-1, 1] \tag{30a}$$

$$u(t, x = -1) = u(t, x = +1) \tag{30b}$$

$$u(t = 0, x) = u_0(x) \tag{30c}$$

with periodic boundary-conditions (BCS) and different initial conditions (ICS) $u_0(x)$. The periodicity conditions are applied by adding, at each end of the computational domain ($x < -1$ and $x > +1$) $N_{\text{PH}} = r$ phantom nodes, for the $(2r-1)$-order scheme (Section 2.4). These phantom nodes are updated at each RK-stage, from the corresponding values of actual nodes. In this way, the first and last actual grid-nodes have a complete stencil for the WENO reconstruction. The reconstruction procedure, for the phantom nodes, is applied by progressively reducing the order, based on the available points for constructing the stencil. Since the phantom nodes are updated at each RK-stage, using values from actual nodes with a complete stencil $\mathsf{s}_{i,r,r}$, this procedure preserves the $O(\Delta x^{2r-1})$ accuracy of the scheme.

3.2. Time-integration

To study the actual order-of-accuracy, by determining the rate-of-convergence r_{CNVRG} of the various schemes for selected test-problems, it is useful to apply time-discretizations of the same order as the space-discretization. It is well known [36] that A-stable general purpose Runge–Kutta (RK) routines of such high-order (up to 17) are either not readily available, or else require a very large number of stages [36]. Furthermore, the requirement that the method be strong-stability-preserving (SSP) [23,27,37–40] for the general nonlinear case, complicates the problem even more.

In the present study we used linear strong-stability-preserving Runge–Kutta algorithms (ℓSSPRK), which are SSP for linear problems [37–39]. We used in particular the M_{RK}-stages methods of $(M_{\text{RK}}-1)$-order (ℓSSPRK$(M_{\text{RK}}, M_{\text{RK}}-1)$), developed by Gottlieb et al. [37], whose coefficients can be determined recursively, up to the desired order of accuracy, [39, p. 116] These schemes have CFL-coefficient $c_{\text{CFL}} = 2$, where $c_{\text{CFL}} := \Delta t_{\text{stab}}/\Delta t_{\text{stab}_{\text{FE}}}$ is the ratio of the stability-time-step of the ℓSSPRK method Δt_{stab} to the stability-time-step of the explicit forward-Euler method $\Delta t_{\text{stab}_{\text{FE}}}$, for the particular problem studied. Obviously the CFL-coefficient $c_{\text{CFL}} = 2$ should not be confused with the CFL-number [37–40]. Another advantage presented by these methods is that all the β-coefficients (in the RK formulation of Shu and Osher [23,27]) are positive, so that they do not require the use of the downwind-operator [23,27,37–40]. For general nonlinear problems, the ℓSSPRK$(M_{\text{RK}}, M_{\text{RK}}-1)$ methods are no longer $O(\Delta t^{M_{\text{RK}}-1})$.

3.3. Influence of the exponent p_β

The exponent p_β (Eq. (17b)) is a free parameter in the formulation of the WENO(M) schemes, and has no direct influence on the formal order-of-accuracy of the scheme [1–4]. It does, however, control the amount of nonlinear dissipation [4], which increases with increasing p_β. The original proposal of Liu et al. [1] was $p_\beta = r$ for the WENO$(2r-1)$ scheme. Jiang and Shu [2] suggested that $p_\beta = 2$ is an appropriate choice for the WENO3 ($r = 2$) and for the WENO5 ($r = 3$) schemes. Balsara and Shu [3] who computed the coefficients up to the WENO11 scheme, did not study the influence of the exponent p_β for test-cases with discontinuities, which were run, instead, using the MPWENO schemes. Martín et al. [10] have shown that $p_\beta = 1$ (low-dissipation) may be sufficient for the WENO5 ($r = 3$) scheme (with a low CFL = 0.2), but not for the WENO7 ($r = 4$) scheme, which requires $p_\beta = 2$ to preserve monoticity [10].

We study in detail the influence of the value of the exponent p_β for the advection of a square wave

$$u_\sqcap(x) = \begin{cases} 0; & -1 \leqslant x < -\frac{1}{2} \\ 1; & -\frac{1}{2} \leqslant x < \frac{1}{2} \\ 0; & \frac{1}{2} \leqslant x < 1 \end{cases} \quad ; \quad x \in [-1, 1] \tag{31}$$

The wave was advected 8 times through the computational domain, using the ℓSSPRK$(2r, 2r-1)$ time-integration procedure, with CFL = 0.8, along with the corresponding WENO$(2r-1)$ or WENOM$(2r-1)$ scheme, with 2 different values of p_β ($p_\beta = 2$ or $p_\beta = r$). The computations (Figs. 1 and 2) were run on progressively refined computational grids of $N_x = 21, 41, 81, 161, 321, 641$ points (not counting the phantom nodes). The WENOM$(2r-1)$ schemes with $p_\beta = r$ (Fig. 1) correctly reproduce the square wave $\forall r$ as N_x increases. Even on the very coarse $N_x = 21$ points grid, the square wave is correctly reproduced for

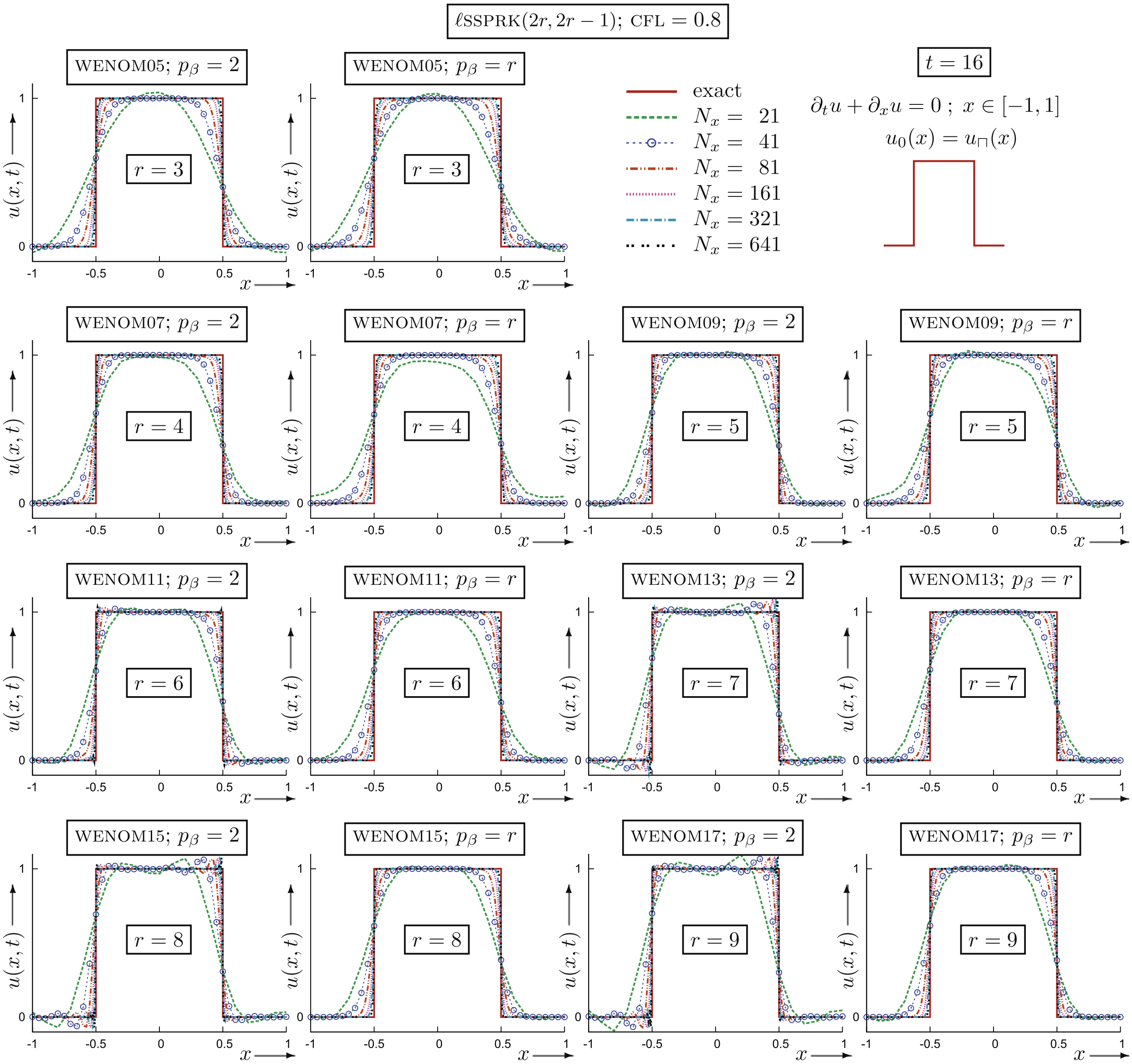

Fig. 1. Comparison of the analytical solution with the numerical solution of the linear advection equation $\partial_t + \partial_x u = 0$ ($x \in [-1, 1]$), with periodic BCS, and IC $u_0(x) = u_\sqcap(x)$ (31), advected 8 times through the computational domain, obtained with the WENOM$(2r-1)$ schemes for $r \in \{3, \dots, 9\}$, with 2 different values of the exponent p_β in the definition of the Jiang–Shu [2] nonlinear weights (17b) ($p_\beta = 2$ and $p_\beta = r$), using ℓSSPRK$(2r, 2r-1)$ time-integration [39] with CFL $= \Delta t \Delta x^{-1} = 0.8$, on progressively refined computational grids ($N_x = 21, 41, 81, 161, 321, 641$ points).

$r \geqslant 7$ (WENOM13, WENOM15, WENOM17; $p_\beta = r$). On the other hand, the WENOM$(2r-1)$ schemes with $p_\beta = 2$ (Fig. 1) work well up to $r = 5$ (WENOM9), but become oscillatory for $r \geqslant 6$ (Fig. 1). The same conclusions apply to the WENO$(2r-1)$ schemes (Fig. 2), which, however, being more dissipative than the corresponding WENOM$(2r-1)$ schemes, remain ENO, for $p_\beta = 2$, for $r \leqslant 6$, but are oscillatory for $r \geqslant 7$ (Fig. 2), in agreement with the recommandation of Balsara and Shu [3], who developed WENO$_{p_\beta=2}$ schemes up to $r = 6$.

Obviously, as r increases, the value $p_\beta = 2$ has also to be increased. The value $p_\beta = r$ (which was the original proposition of Liu et al. [1]) ensures ENO behaviour in all cases. Nonetheless, this value is probably too high. The determination of the optimal (lowest, and hence less dissipative) value $p_\beta(r) \in [2, r]$ will be the subject of a future study.

3.4. Test-cases

The performance and order-of-accuracy of the various schemes is studied by comparing with the exact solution of the advection equation (30) for different initial conditions (ICs). All of the computations used the corresponding ℓSSPRK$(2r, 2r-1)$ time-discretization.

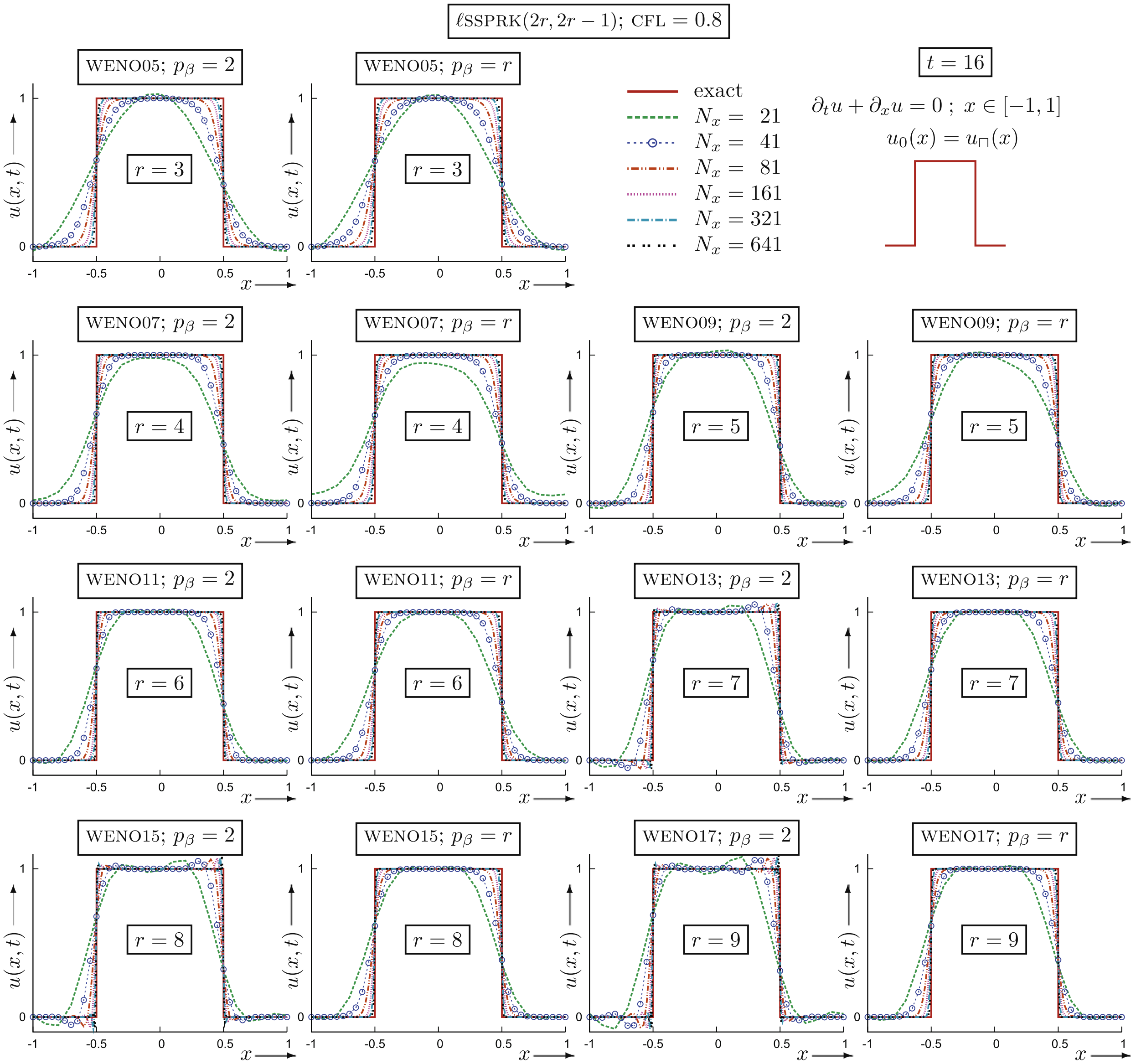

Fig. 2. Comparison of the analytical solution with the numerical solution of the linear advection equation $\partial_t + \partial_x u = 0$ ($x \in [-1, 1]$), with periodic BCs, and IC $u_0(x) = u_\sqcap(x)$ (31), advected 8 times through the computational domain, obtained with the WENO$(2r-1)$ schemes for $r \in \{3, \ldots, 9\}$, with 2 different values of the exponent p_β in the definition of the Jiang–Shu [2] nonlinear weights (17b) ($p_\beta = 2$ and $p_\beta = r$), using ℓSSPRK$(2r, 2r-1)$ time-integration [39] with CFL $= \Delta t \Delta x^{-1} = 0.8$, on progressively refined computational grids ($N_x = 21, 41, 81, 161, 321, 641$ points).

3.4.1. $u_0(x) = \sin(\pi x + \pi^{-1} \sin \pi x)$

We computed this test-case [4], using the UW$(2r-1)$, and the WENO$(2r-1)$ or WENOM$(2r-1)$ schemes, with $p_\beta = 2$ and $p_\beta = r$ (Fig. 3). The wave was advected 10 times through the computational domain, using ℓSSPRK$(2r, 2r-1)$ time-discretization with CFL $= 1$. As the number of cells ($N_c = N_x - 1$) increases, the L_∞-norm of the error [4] E_{L_∞} of the UW$(2r-1)$ scheme

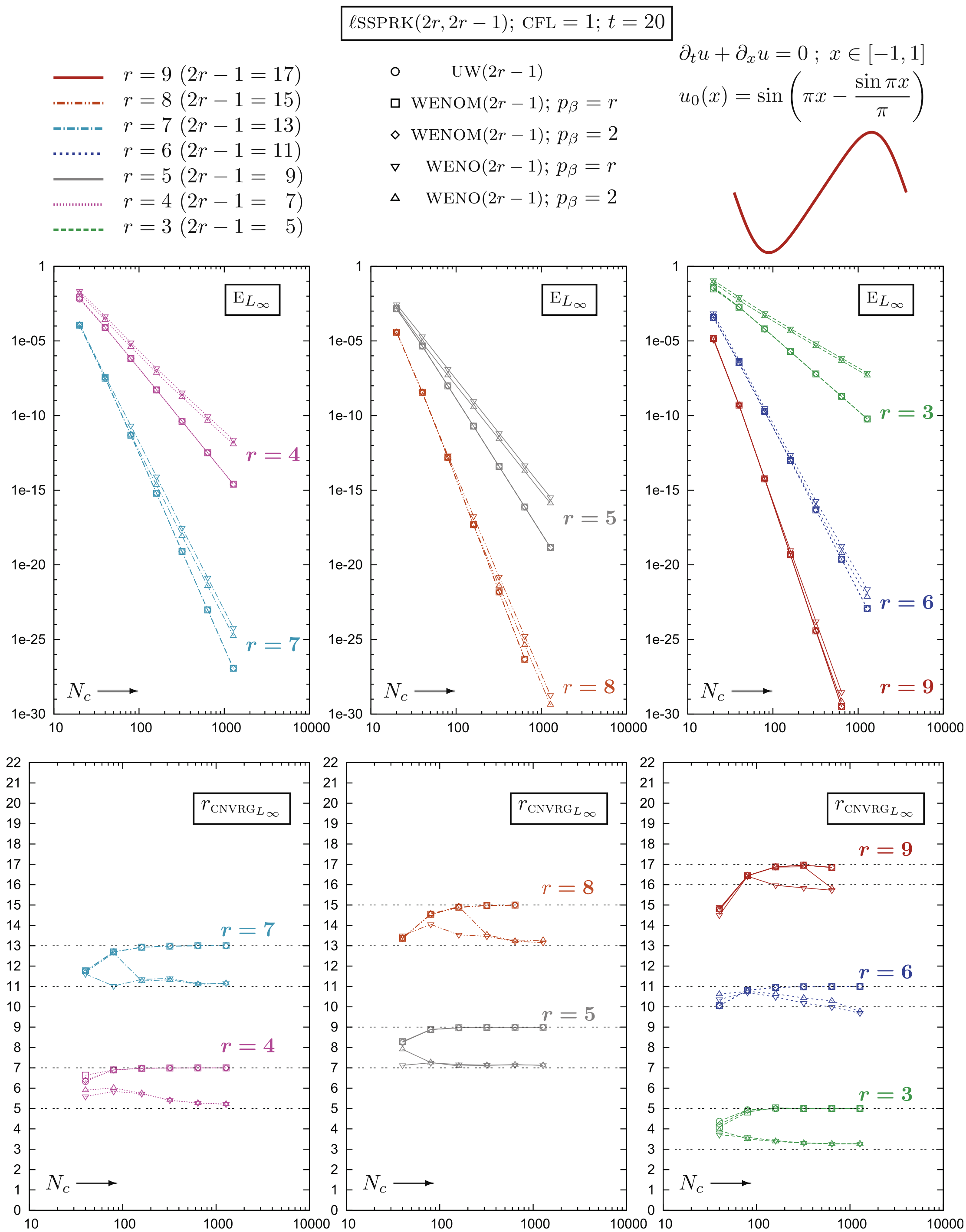

Fig. 3. L_∞-norm error E_{L_∞} and rate-of-convergence $r_{\mathrm{CNVRG}_{L_\infty}}$, as a function of the number of grid-cells $N_c = N_x - 1$, for the UW$(2r-1)$, WENO$(2r-1)$ and WENOM$(2r-1)$ reconstructions ($r = 3, \dots, 9$), with $p_\beta = 2$ and $p_\beta = r$, for the linear advection equation $\partial_t + \partial_x u = 0$ ($x \in [-1, 1]$), with periodic BCs, and IC $u_0(x) = \sin(\pi x + \pi^{-1} \sin \pi x)$, using ℓSSPRK$(2r, 2r-1)$ time-integration [39] with CFL $= \Delta t \Delta x^{-1} = 1$ (the wave was advected 10 times through the computational domain).

decreases, with the theoretical rate-of-convergence [2,4] $r_{\text{CNVRG}_{L_\infty}} = 2r - 1$. The computations were performed using 128-bit arithmetic (quadruple precision; `real*16` [41]), and the UW17 scheme already reaches machine-precision on an $N_x = 641$ points grid (Fig. 3).

It is well known [4] that WENO schemes do not reach their formal order-of-accuracy of $O(\Delta x^{2r-1})$ at critical points $(u_0'(x_{\text{CP}}) = 0)$. At such points, the first terms retained in the Taylor-expansions of the smoothness indicators $\beta_{r,k_s,i+\frac{1}{2}}$ (27) which

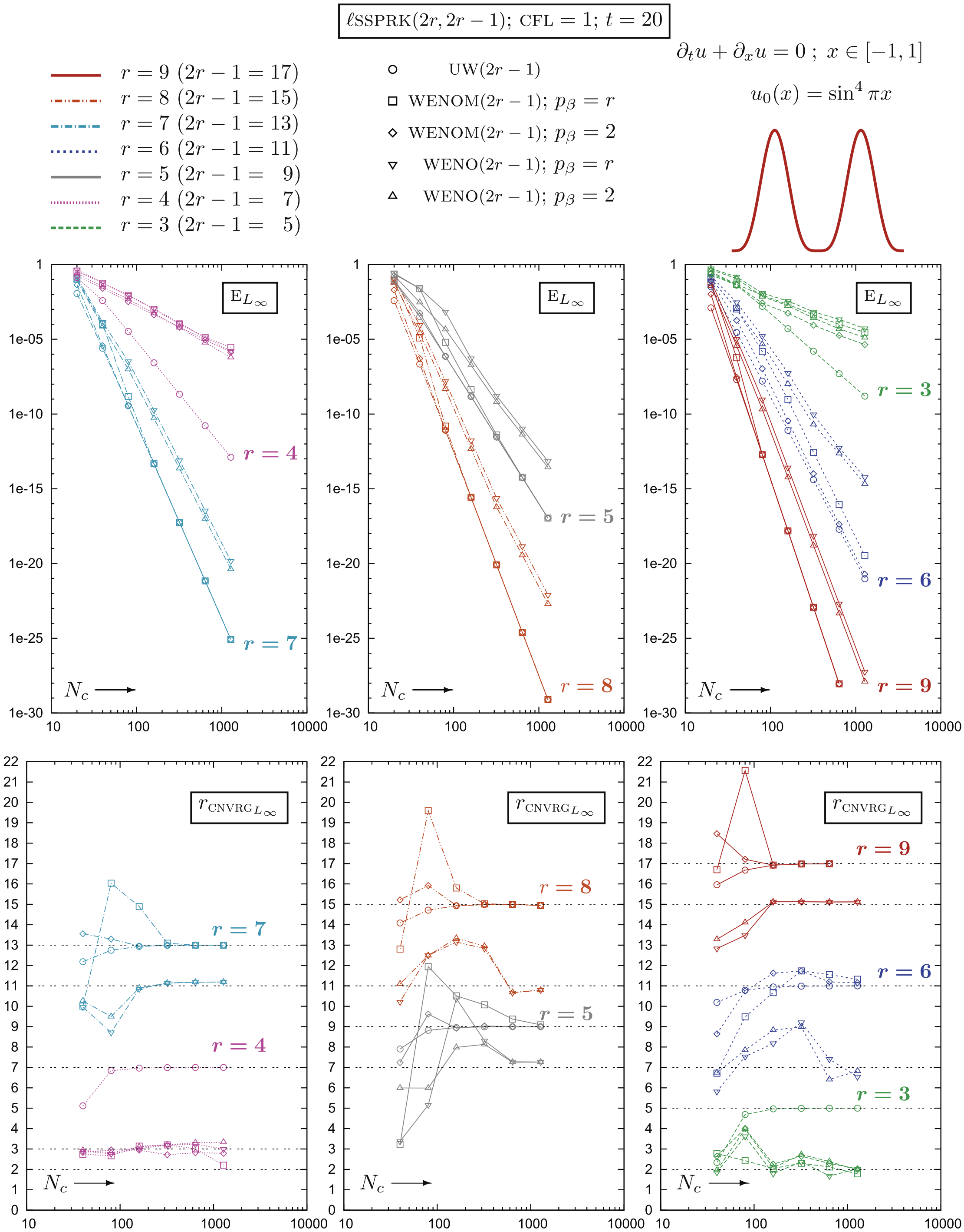

Fig. 4. L_∞-norm error E_{L_∞} and rate-of-convergence $r_{\text{CNVRG}_{L_\infty}}$, as a function of the number of grid-cells $N_c = N_x - 1$, for the UW$(2r-1)$, WENO$(2r-1)$ and WENOM$(2r-1)$ reconstructions $(r = 3, \ldots, 9)$, with $p_\beta = 2$ and $p_\beta = r$, for the linear advection equation $\partial_t + \partial_x u = 0$ $(x \in [-1, 1])$, with periodic BCS, and IC $u_0(x) = \sin^4 \pi x$, using ℓSSPRK$(2r, 2r-1)$ time-integration [39] with CFL $= \Delta t \Delta x^{-1} = 1$ (the wave was advected 10 times through the computational domain).

scheme (Fig. 3). Expectedly, and in agreement with the analysis of Henrick et al. [4, Table 10, p. 566], the WENO$(2r-1)$ schemes have a rate-of-convergence of $r_{\text{CNVRG}_{L_\infty}} = \max(2r-2-n_{\text{CP}}, n_{\text{CP}}, r-1) = \max(2r-3, 1, r-1)$ (Fig. 3). The WENO11 $(r=6)$ and the WENO17 $(r=9)$ schemes (Fig. 3), have not reached their asymptotic $r_{\text{CNVRG}_{L_\infty}}$ at $N_c = 1200$, but are still 1 order

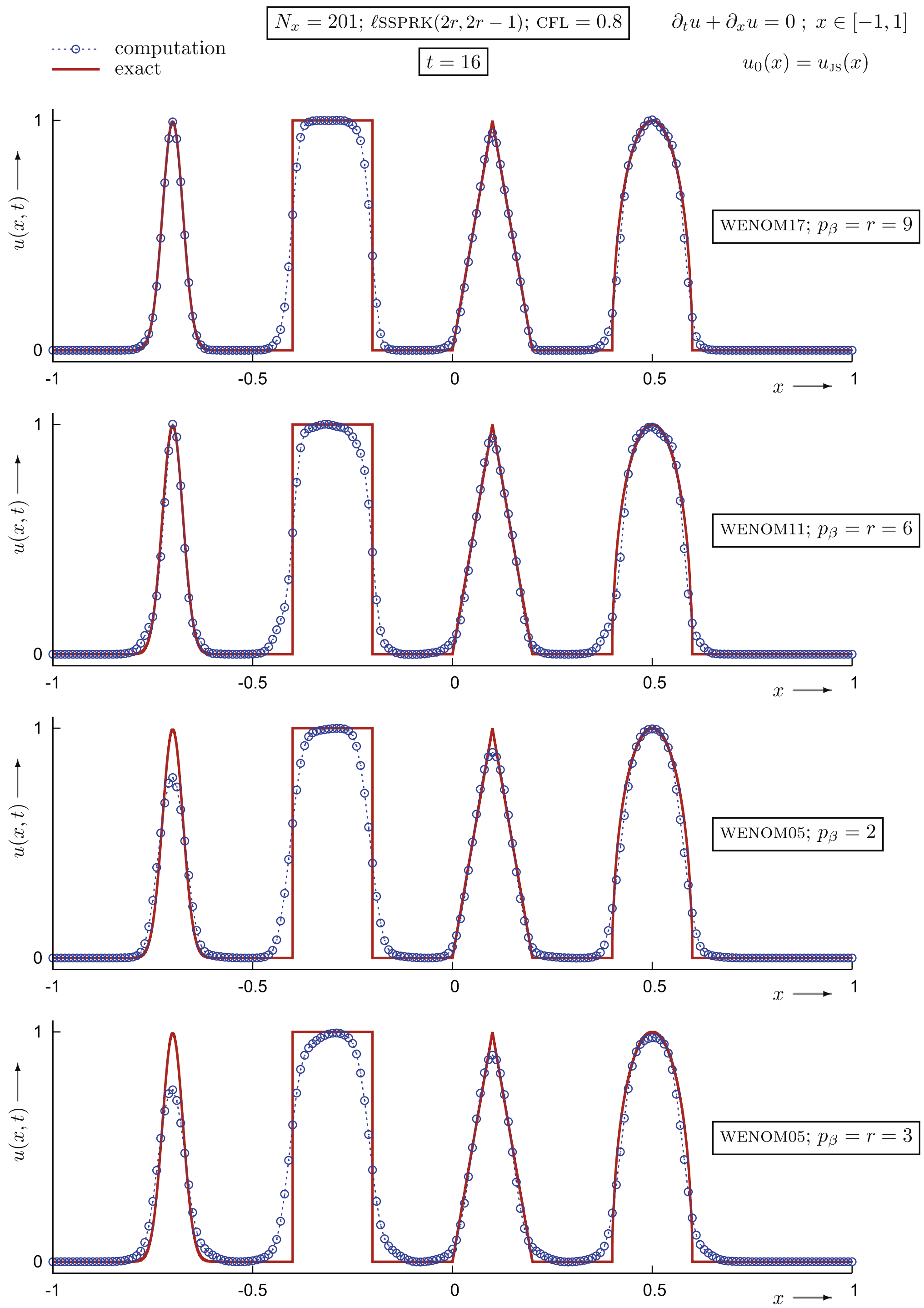

Fig. 6. Comparison of the analytical solution with the numerical solution of the linear advection equation $\partial_t + \partial_x u = 0$ $(x \in [-1, 1])$, with periodic BCS, and IC $u_0(x) = u_{\text{JS}}(x)$ (Jiang–Shu [2, p. 213] waveform), convected 8 times through the computational domain, obtained with the WENOM5 ($p_\beta = 2$ and $p_\beta = r = 3$), the WENOM11 ($p_\beta = r = 6$), and the WENOM17 ($p_\beta = r = 9$) schemes, using ℓSSPRK$(2r, 2r-1)$ time-integration [39] with CFL $= \Delta t \Delta x^{-1} = 0.8$, on a grid of $N_x = 201$ points ($N_c = 200$ cells).

higher (10 and 16, respectively, instead of 9 and 15). Closer examination indicates that, for these 2 schemes, $r_{\text{CNVRG}_{L_\infty}}$ is not yet stabilized but dropping.

Notice (Fig. 3) that the influence of the exponent p_β is small. The higher values $p_\beta = r$ giving marginally higher values of E_{L_∞}, and, of course (cf. Section 2.3.6) p_β has no influence on the rate-of-convergence, once the asymptotic region is reached (Fig. 3). Notice also (Fig. 3) a superconvergence accident [2,4] for the WENO schemes, especially with $p_\beta = 2$, at intermediate values of N_c, for $r \geqslant 7$. For instance, with the WENO15 scheme ($r = 8$), $r_{\text{CNVRG}_{L_\infty}} = 15$, for $p_\beta = 2$, at $N_c = 160$, then dropping to the theoretically [4] expected value of 13 for $N_c \geqslant 320$ (Fig. 3).

3.4.2. $u_0(x) = \sin^4 \pi x$

This wave [2] is more complex because the degree of the critical points [4] is $n_{\text{CP}} = 3$ $\left(u_0'(x_{\text{CP}}) = 0,\ u_0''(x_{\text{CP}}) = 0,\ u_0'''(x_{\text{CP}}) = 0,\ u_0''''(x_{\text{CP}}) \neq 0\right)$. We computed this test-case [2], using the UW$(2r-1)$, and the WENO$(2r-1)$ or WENOM$(2r-1)$ schemes, with $p_\beta = 2$ and $p_\beta = r$ (Fig. 4). The wave was advected 10 times through the computational domain, using ℓSSPRK$(2r, 2r-1)$ time-discretization with CFL $= 1$. Again (Fig. 4), the UW$(2r-1)$ schemes reach rapidly their theoretical rate-of-convergence [2,4] $r_{\text{CNVRG}_{L_\infty}} = 2r-1$. The WENOM$(2r-1)$ schemes, for $r \geqslant 5$, converge, as N_c increases, to the corresponding upwind scheme (Fig. 4), the final asymptotic rate-of-convergence being independent of p_β. Nonetheless, the convergence of the WENOM scheme to the corresponding upwind scheme, as N_c increases, is slower for $p_\beta = r$ than for $p_\beta = 2$ (Fig. 4).

For $r = 5$, e.g. the WENOM9 scheme, with $p_\beta = r$, converges asymptotically to the UW9 scheme (Fig. 4), as late as $N_c = 1200$, inducing a superconvergence accident [2], also observed for the WENOM13 ($r = 7$), WENOM15 ($r = 8$), WENOM17 ($r = 9$) schemes (Fig. 4). Notice also that, for $r = 5$, the WENOM9 schemes achieve $r_{\text{CNVRG}_{L_\infty}} = 2r-1 = 9$ (Fig. 4), which is in contradiction with the analysis of Henrick et al. [4] (which predicts $r_{\text{CNVRG}_{L_\infty}}(\text{WENOM9}) = 7$).

Concerning the WENO$(2r-1)$ schemes (without mapping of the nonlinear weights), there is very little influence of p_β (Fig. 4). Examination of the loss of accuracy at the $n_{\text{CP}} = 3$ critical points (Fig. 4) suggest that the behaviour is different for r odd or even. For r even ($r = 4, 6, 8$) the numerical results are in agreement with the analysis of Henrick et al. [4], predicting $r_{\text{CNVRG}_{L_\infty}} = \max(2r-2-n_{\text{CP}}, n_{\text{CP}}, r-1) = \max(2r-5, 3, r-1)$, i.e. loss of 4 orders (Fig. 4). On the other hand, for the WENO$(2r-1)$ schemes with r odd ($r = 5, 7, 9$) the loss of accuracy (rate-of-convergence $r_{\text{CNVRG}_{L_\infty}}$) is of only 2 orders (Fig. 4). It is probable that this difference in behaviour for r odd or even is related to the observed differences (cf. Section 2.3.6) in the Taylor-expansions of the smoothness indicators $\beta_{r,k_s,i+\frac{1}{2}}$.

Notice also that (22) and (23) are sufficient (but not necessary) conditions for the WENO$(2r-1)$ scheme to be $O(\Delta x^{2r-1})$. Furthermore, the corresponding analysis based on Taylor-expansions of the smoothness indicators does not investigate the influence of the difference between $\omega_{r,k_s,i+\frac{1}{2}}$ and $\omega_{r,k_s,i-\frac{1}{2}}$ (it is this that makes (22) a sufficient but not necessary condition). Further work, based on the full asymptotic expansions of the WENO (WENOM) reconstructions, is necessary to clarify this behaviour.

3.4.3. $u_0(x) = u_{\text{JS}}(x)$

Finally, we computed the advection of the Jiang–Shu [2, p. 213] waveform, which consists of a smooth but narrow combination of Gaussians, a square wave, a sharp triangle wave, and a half ellipse (Figs. 5 and 6), using the WENOM5 ($p_\beta = 2$ and $p_\beta = r = 3$), the WENOM11 ($p_\beta = r = 6$), and the WENOM17 ($p_\beta = r = 9$) schemes. The wave was advected 8 times through the computational domain, using ℓSSPRK$(2r, 2r-1)$ time-integration with CFL $= 0.8$. On the coarse $N_x = 101$ points grid (Fig. 5) the WENOM5 schemes (both $p_\beta = 2$ and $p_\beta = r = 3$) fail to accurately describe the square wave (which looks in the numerical solution more like a sinusoidal wave), and severely underestimate the peaks of both the Gaussians and of the triangle wave (Fig. 5). Furthermore, the flat regions $u(x,t) = 0$ between waves, are mistaken for sinusoidal waves (Fig. 5), because of the coarseness of the mesh. The situation is substantially improved by the WENOM11 ($p_\beta = r = 6$) scheme, and especially by the WENOM17 ($p_\beta = r = 9$) scheme (Fig. 5), which not only resolves the square wave, but also recognizes the flat regions $u(x,t) = 0$ between waves, even on this very coarse $N_x = 101$ points grid. On a twice finer $N_x = 201$ points grid (Fig. 6), the WENOM17 ($p_\beta = r = 9$) scheme gives very good agreement with the analytical solution (and so does, to a somehow lesser extent, the WENOM11; $p_\beta = r = 6$ scheme), while remaining perfectly ENO. On this finer $N_x = 201$ points grid (Fig. 6) the WENOM5 ($p_\beta = 2$ and $p_\beta = r = 3$) schemes have resolution similar to the WENOM17 ($p_\beta = r = 9$) scheme on the $N_x = 101$ points grid (Fig. 5). These results illustrate very well the improvement in accuracy by the high-order WENOM schemes.

4. Burgers equation

To verify that the results obtained for the linear advection equation are also valid for the nonlinear scalar case (nonlinear scalar hyperbolic conservation law), we applied the family of WENOM$(2r-1)$ reconstructions, with $p_\beta = r$, to the Burgers equation [22,23,1]

$$\frac{\partial u}{\partial t} + \frac{\partial}{\partial x}\left(\frac{1}{2}u^2\right) = 0; \quad x \in [0,2] \tag{32a}$$

$$u(t, x=0) = u(t, x=2) \tag{32b}$$

$$u(t=0, x) = u_0(x) = \frac{1}{2} + \sin \pi x \tag{32c}$$

with periodic boundary-conditions. The periodicity conditions are applied by adding, at each end of the computational domain ($x < -1$ and $x > +1$) $N_{\text{PH}} = r$ phantom nodes, for the $(2r-1)$-order scheme (cf. Sections 2.4 and 3.1).

The analytical solution was computed using the method of characteristics [42]. The solution [1] is smooth for $t \leqslant \pi^{-1}$, a shock-wave appearing for $t \geqslant \pi^{-1}$. We computed this problem until $t = 0.7$, with the WENOM$(2r-1)$ schemes, for $r \in [3, 9]$, with $p_\beta = r$, on different grids (Fig. 7), using SSPRK$(8,3)$ time-integration [40], with $\max_i(\text{CFL}) = 1$ (the time-step varies from one iteration to the next, to satisfy the condition $\text{CFL} = 1$, and is very slightly readjusted to obtain exactly $t_{\text{END}} = 0.7$ at the final iteration). We used $\text{WENOM}_{p_\beta=r}$ reconstruction of the variables, $u^{\text{L}}_{i+\frac{1}{2}}$ and $u^{\text{R}}_{i+\frac{1}{2}}$, and an exact Riemann solver [43, pp. 176–178] (RS) sampled to compute the Godunov state $u^{\text{GDNV}}_{i+\frac{1}{2}} = u^{\text{GDNV}}_{\text{RS}}(u^{\text{L}}_{i+\frac{1}{2}}, u^{\text{R}}_{i+\frac{1}{2}})$, at which is computed the flux $F^{\text{GDNV}}_{i+\frac{1}{2}}$. The maximum wavespeed computed by the RS $\mathsf{s}_{i+\frac{1}{2}}$ is used to define $\text{CFL}_i = \max\left(\left|\mathsf{s}_{i+\frac{1}{2}}\right|, \left|\mathsf{s}_{i-\frac{1}{2}}\right|\right)\Delta t \Delta x^{-1}$.

All of the WENOM$(2r-1)$ schemes ($r \in [3, 9]$) perform quite well (Fig. 7), even with the coarsest $N_x = 21$ points computational grid, are perfectly nonoscillatory, up to the WENOM17 scheme, and the shock-wave is accurately predicted. The problem is apparently too easy for the differences between schemes of various orders to be discernible.

5. 1-D Euler equations

5.1. System of the 1-D Euler equations

The high-order WENO reconstruction is extended to the 1-D Euler equations [43]

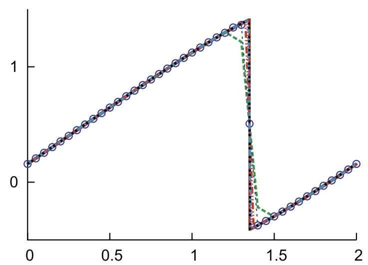

$$\frac{\partial \underline{u}}{\partial t}+\frac{\partial \underline{F}(\underline{u})}{\partial x}=0 \Longleftrightarrow \frac{\partial}{\partial t}\begin{bmatrix}\rho\\ \rho u\\ \rho e_t\end{bmatrix}+\frac{\partial}{\partial x}\begin{bmatrix}\rho u\\ \rho u^2+p\\ \rho u h_t\end{bmatrix}=0 \tag{33}$$

where $\underline{u}=[\rho,\rho u,\rho e_t]^{\mathrm{T}}$ is the vector of conservative variables, $\underline{F}(\underline{u})=[\rho u,\rho u^2+p,\rho u h_t]^{\mathrm{T}}$ is the flux, ρ is the density, u is the velocity, p is the pressure, $e_t=e+\frac{1}{2}u^2$ is the total internal energy, e is the internal energy, $h_t=h+\frac{1}{2}u^2$ is the total enthalpy, $h=e+p\rho^{-1}$ is the enthalpy. We assume perfect gas thermodynamics, with

$$p=(\gamma-1)\rho\left(e_t-\frac{1}{2}u^2\right)=\frac{\gamma-1}{\gamma}\rho\left(h_t-\frac{1}{2}u^2\right);\quad a=\sqrt{\gamma\frac{p}{\rho}} \tag{34}$$

where a is the speed-of-sound [43]. We will note

$$\underline{v}:=\begin{bmatrix}\rho\\ u\\ p\end{bmatrix} \tag{35}$$

the vector of primitive variables. For all of the test-cases studied $\gamma=1.4$.

5.2. Remarks on the scalar WENO reconstruction

The numerical experiments, presented in Section 3 for the advection equation (using ℓSSPRK$(2r,2r-1)$) and in Section 4 for the Burgers equation (using SSPRK(8,3)), indicate that the scalar WENOM$(2r-1)$ reconstruction, with $p_\beta=r$, is ENO, with CFL $\in[0.8,1]$, both for linear and for nonlinear scalar hyperbolic conservation laws. Therefore, the WENOM$_{p_\beta=r}$ scalar reconstructions will be used as basic building block of the variables reconstruction for the Euler equations.

5.3. Local characteristic reconstruction

The extension of the scalar WENOM reconstruction to systems of hyberbolic conservation laws, whether applied to fluxes [2–4] or to variables [5,13,6] (this was also the choice made in the original ENO schemes [12]), is based on local characteristic decomposition [12]

$$\underline{w}_{i+\frac{1}{2},i+\ell}:=\underline{\underline{L}}\left(\underline{u}^{\mathrm{AVG}}_{i+\frac{1}{2}}\right)\underline{u}_{i+\ell};\quad i+\ell\in\mathsf{S}_{i,r-1,r-1}:=\{i-(r-1),\ldots,i+(r-1)\} \tag{36}$$

where $\underline{\underline{L}}$ is the matrix of left eigenvectors [12] of the flux-Jacobian $\underline{\underline{A}}(\underline{u}):=\partial_{\underline{u}}\underline{F}$ and $\underline{u}^{\mathrm{AVG}}_{i+\frac{1}{2}}(\underline{u}_i,\underline{u}_{i+1})$ is an average state at the interface. There are several possible choices for $\underline{u}^{\mathrm{AVG}}_{i+\frac{1}{2}}$, such as [12] arithmetic average, or Roe-average [44]. In the present work we have used

$$\underline{u}^{\mathrm{AVG}}_{i+\frac{1}{2}}=\underline{u}^{\mathrm{GDNV}}_{\mathrm{RS}}(\underline{u}_i,\underline{u}_{i+1}) \tag{37}$$

where $\underline{u}^{\mathrm{GDNV}}_{\mathrm{RS}}(\underline{u}_{\mathrm{L}},\underline{u}_{\mathrm{R}})$ is the Godunov state obtained by sampling the exact solution of the $(\underline{u}_{\mathrm{L}},\underline{u}_{\mathrm{R}})$ Riemann problem (cf. Section 5.6). The WENOM-reconstructed characteristic variables are then projected back to the conservative variables space, using the matrix of the right eigenvectors $\underline{\underline{R}}=\underline{\underline{L}}^{-1}$ [12]

$$\underline{u}^{\mathrm{L}}_{r,\mathrm{WENOM}_c,i+\frac{1}{2}}=\underline{\underline{R}}\left(\underline{u}^{\mathrm{AVG}}_{i+\frac{1}{2}}\right)\underline{w}^{\mathrm{L}}_{r,\mathrm{WENOM},i+\frac{1}{2}}\left(\underline{w}_{i+\frac{1}{2},i-(r-1)},\ldots,\underline{w}_{i+\frac{1}{2},i+(r-1)}\right) \tag{38}$$

where the WENOM reconstruction of $\underline{w}$ is understood as the scalar reconstruction of each characteristic field. Notice [12,5] that the much simpler componentwise reconstruction of either primitive variables (which automatically guarantees positivity of $\rho_{\mathrm{L}},\ p_{\mathrm{L}},\ \rho_{\mathrm{R}}$ and p_{R}) or of conservative variables can lead to serious oscillations of the solution in presence of strong discontinuities.

5.4. Problem detection and recursive-order-reduction

It is well known [12] that the interaction between characteristic fields and/or the absence of a zone of smoothness of r points to choose (overweight) a stencil from, may cause serious oscillations in the solution, even though the scalar WENOM reconstruction of each characteristic field separately be ENO. Such pathological situations may arise in the starting stages of a 2-shock Riemann problem, or when 2 discontinuities are about to collide. In such instances, no matter how small Δx is, oscillations will appear, which increase with increasing resolution (as r increases and/or as Δx decreases). Titarev and Toro [5] working with the WENO7 scheme, suggested to recursively reduce the reconstruction-order r, for these cell-interfaces $i+\frac{1}{2}$ where a problem is detected. The recursive-order-reduction (ROR) procedure consists of 2 steps:

1. a reconstruction-failure-detection criterion;
2. reducing, at the cell-interfaces where reconstruction-failure is detected, the order from r to $r-1$, and so on, recursively, until reconstruction be considered successful.

The stencils used by the high-order WENO schemes are quite large, enhancing encounters of interacting characteristics, and the possibility of nonexistence of a smooth stencil in the WENO-weighting procedure, so that particular care is required in the reconstruction procedure. In the present work, especially as we are concerned with very-high-order schemes, we adopted the ROR procedure. Nonetheless, the criterion used in Titarev and Toro [5] who considered that the reconstruction was successful provided that $\left[\left|\rho^{\mathrm{L}}_{i+\frac{1}{2}}-\rho_i\right| \leqslant 0.9\rho_i,\ \left|\rho^{\mathrm{R}}_{i+\frac{1}{2}}-\rho_{i+1}\right| \leqslant 0.9\rho_{i+1},\ \left|p^{\mathrm{L}}_{i+\frac{1}{2}}-p_i\right| \leqslant 0.9p_i \text{ and } \left|p^{\mathrm{R}}_{i+\frac{1}{2}}-p_{i+1}\right| \leqslant 0.9p_{i+1}\right]$ is somehow empirical (due to the arbitrary value of 0.9), and active only in the presence of very strong shocks or expansions. On the other hand, it brings forward the idea that reconstruction success or failure may be evaluated by considering the difference between the values of ρ and p reconstructed using WENOM$(2r-1)$, and the corresponding UW1 values (which, although over-dissipative, are always nonoscillatory). If the functions $\rho(x)(p(x))$ were linear, then the exact value of $\rho^{\mathrm{L}}_{i+\frac{1}{2}}\left(p^{\mathrm{L}}_{i+\frac{1}{2}}\right)$ should satisfy the relation $\left|\rho^{\mathrm{L}}_{i+\frac{1}{2}}-\rho_i\right| = \frac{1}{2}|\rho_{i+1}-\rho_i|\left(\left|p^{\mathrm{L}}_{i+\frac{1}{2}}-p_i\right| = \frac{1}{2}|p_{i+1}-p_i|\right)$. This suggests the use of such a criterion, replacing however $\frac{1}{2}|\rho_{i+1}-\rho_i|(\frac{1}{2}|p_{i+1}-p_i|)$ by $\frac{1}{2}\max_\ell|\rho_{i+\ell+1}-\rho_{i+\ell}|(\frac{1}{2}\max_\ell|p_{i+\ell+1}-p_{i+\ell}|)$, with ℓ belonging to a stencil related to the reconstruction stencil. When testing the WENOM$(2r-1)$ reconstruction, we used the stencil corresponding to WENOM$(2r-2)$ scheme. The final criterion reads

$$r \geqslant 3 \quad \mathrm{ROR}^{\mathrm{L}}_{r,i+\frac{1}{2}} = \left\{\left|\rho^{\mathrm{L}}_{i+\frac{1}{2}}-\rho_i\right| \leqslant \frac{1}{2}\max_{-(r-2)\leqslant\ell\leqslant(r-3)}|\rho_{i+\ell+1}-\rho_{i+\ell}| \text{ and } \left|p^{\mathrm{L}}_{i+\frac{1}{2}}-p_i\right| \leqslant \frac{1}{2}\max_{-(r-2)\leqslant\ell\leqslant(r-3)}|p_{i+\ell+1}-p_{i+\ell}|\right\} \tag{39a}$$

$$r = 2 \quad \mathrm{ROR}^{\mathrm{L}}_{r,i+\frac{1}{2}} = \left\{\rho^{\mathrm{L}}_{i+\frac{1}{2}} \geqslant 0 \text{ and } p^{\mathrm{L}}_{i+\frac{1}{2}} \geqslant 0\right\} \tag{39b}$$

where ROR is a logical variable, which is true if the conditions (39) are satisfied. By the usual symmetry with respect to *i* (8) it follows

$$r \geqslant 3 \quad \mathrm{ROR}^{\mathrm{R}}_{r,i+\frac{1}{2}} = \left\{\left|\rho^{\mathrm{R}}_{i+\frac{1}{2}}-\rho_{i+1}\right| \leqslant \frac{1}{2}\max_{-(r-3)\leqslant\ell\leqslant(r-2)}|\rho_{i+\ell+1}-\rho_{i+\ell}| \text{ and } \left|p^{\mathrm{R}}_{i+\frac{1}{2}}-p_{i+1}\right| \leqslant \frac{1}{2}\max_{-(r-3)\leqslant\ell\leqslant(r-2)}|p_{i+\ell+1}-p_{i+\ell}|\right\} \tag{39c}$$

$$r = 2 \quad \mathrm{ROR}^{\mathrm{R}}_{r,i+\frac{1}{2}} = \left\{\rho^{\mathrm{R}}_{i+\frac{1}{2}} \geqslant 0 \text{ and } p^{\mathrm{R}}_{i+\frac{1}{2}} \geqslant 0\right\} \tag{39d}$$

5.5. Complete reconstruction algorithm

The ROR procedure can be writen symbolically

$$\begin{aligned}
&\text{do } q = r, 1, -1\\
&\underline{u}^{\mathrm{L}}_{i+\frac{1}{2}} = \underline{u}^{\mathrm{L}}_{q,\mathrm{WENOM}_c,i+\frac{1}{2}}\\
&\underline{u}^{\mathrm{R}}_{i+\frac{1}{2}} = \underline{u}^{\mathrm{R}}_{q,\mathrm{WENOM}_c,i+\frac{1}{2}}\\
&\text{if } \left\{\mathrm{ROR}^{\mathrm{L}}_{q,i+\frac{1}{2}}\left(\underline{u}^{\mathrm{L}}_{i+\frac{1}{2}}\right) \text{ and } \mathrm{ROR}^{\mathrm{R}}_{q,i+\frac{1}{2}}\left(\underline{u}^{\mathrm{R}}_{i+\frac{1}{2}}\right)\right\} \text{ exit}\\
&\text{end do}
\end{aligned} \tag{40}$$

We start by reconstructing at $q=r$, and then check if the reconstruction conditions (39) at $i+\frac{1}{2}$ are satisfied. If they are, both for $\underline{u}^{\mathrm{L}}_{i+\frac{1}{2}}$ and for $\underline{u}^{\mathrm{R}}_{i+\frac{1}{2}}$, the reconstructed variables at $i+\frac{1}{2}$ are kept (the algorithm exits). If the reconstruction conditions (39) are not satisfied, either for $\underline{u}^{\mathrm{L}}_{i+\frac{1}{2}}$ or for $\underline{u}^{\mathrm{R}}_{i+\frac{1}{2}}$, the order is reduced, locally at $i+\frac{1}{2}$, to $r-1$, and so on, recursively until either (39) are satisfied for some $q \leqslant r$, or the UW1 scheme is reached.

5.6. Exact Riemann solver and Godunov flux

We used the exact Riemann solver reported in Toro [43] to define the Godunov state

$$\underline{u}^{\mathrm{GDNV}}_{i+\frac{1}{2}} = \underline{u}^{\mathrm{GDNV}}_{\mathrm{RS}}\left(\underline{u}^{\mathrm{L}}_{r,\mathrm{RORWENOM}_c,i+\frac{1}{2}}, \underline{u}^{\mathrm{R}}_{r,\mathrm{RORWENOM}_c,i+\frac{1}{2}}\right) \tag{41}$$

which is the state at which the Godunov flux is evaluated. As noted by Titarev and Toro [6] the Godunov flux is the less dissipative monotone flux, on the basis of an analysis of various fluxes for the advection equation.

5.7. Time-integration

We used the Shu–Osher [23] SSPRK(3,3), with CFL $= 0.6$, for all of the Euler results presented in the present work. The time-step varies from one iteration to the next, to satisfy the condition CFL $= 0.6$, and is very slightly readjusted to obtain exactly the desired value of t_{END} at the final iteration.

5.8. Typical 1-D test-cases

5.8.1. Riemann problems of Sod and Lax

The standard Riemann problems of Lax [24]

$$\underline{v}(x \leqslant 0, t=0) = \underline{v}_{\mathrm{L}} = \begin{bmatrix} 0.445 \\ 0.698 \\ 3.528 \end{bmatrix}; \quad \underline{v}(x > 0, t=0) = \underline{v}_{\mathrm{R}} = \begin{bmatrix} 0.500 \\ 0.000 \\ 0.571 \end{bmatrix}; \quad x \in [-5, +5] \tag{42}$$

and of Sod [25]

$$\underline{v}(x \leqslant 0, t=0) = \underline{v}_{\mathrm{L}} = \begin{bmatrix} 1.000 \\ 0.000 \\ 1.000 \end{bmatrix}; \quad \underline{v}(x > 0, t=0) = \underline{v}_{\mathrm{R}} = \begin{bmatrix} 0.125 \\ 0.000 \\ 0.100 \end{bmatrix}; \quad x \in [-5, +5] \tag{43}$$

were computed (Fig. 8) with the RORWENOM5 ($r=3$), the RORWENOM11 ($r=6$), and the RORWENOM17 ($r=9$) schemes, using SSPRK(3,3) at CFL $= 0.6$, on different grids ($N_x = 51, 101, 201, 401, 801, 1601$ points), up to $t_{\mathrm{END}} = 1.3$ (Lax [24]) and to $t_{\mathrm{END}} = 2$ (Sod [25]). For $t \leqslant t_{\mathrm{END}}$, waves created by the discontinuity at $(x,t) = (0,0)$ do not reach the boundaries, where a no-change ($\underline{u}(x_{\mathrm{B}}, t) = \underline{u}_0(x_{\mathrm{B}})\ \forall t$) condition is applied. All of the schemes perform quite well for these difficult problems, and give reasonably ENO results on all grids (Fig. 8). It is important to notice that, as $\Delta x \to 0$, the schemes remain ENO (Fig. 8). This is ensured by the ROR algorithm (Section 5.4). For the Lax problem, as the reconstruction-order increases, the resolution of the square wave in the ρ distribution is improved (Fig. 8). The slight oscillation observed, for the Lax problem, for the RORWENOM17 scheme with $N_x = 101$ points, is induced by the coarseness of the grid, and completely disappears as $\Delta x \to 0$ (Fig. 8).

5.8.2. Shu–Osher shock-wave/entropy interaction

The ICS for the shock-wave/entropy interaction problem, introduced by Shu and Osher [27], describe the interaction of a uniform left state ($x \leqslant x_{\mathrm{SW}_0}$) with a right state ($x > x_{\mathrm{SW}_0}$) which is perturbed by a sinusoidal density-variation

$$\underline{v}_0(x \leqslant x_{\mathrm{SW}_0}) = \underline{v}_{\mathrm{L}} = \begin{bmatrix} \rho_{\mathrm{L}} \\ u_{\mathrm{L}} \\ p_{\mathrm{L}} \end{bmatrix}; \quad \underline{v}_0(x > x_{\mathrm{SW}_0}) = \begin{bmatrix} \rho_{\mathrm{R}} + A_\rho \sin \kappa_\rho x \\ u_{\mathrm{R}} \\ p_{\mathrm{R}} \end{bmatrix} = \underline{v}_{\mathrm{R}} + \begin{bmatrix} A_\rho \sin \kappa_\rho x \\ 0 \\ 0 \end{bmatrix} \tag{44}$$

We computed the original Shu–Osher [27] problem, and 2 other variants, introduced by Titarev and Toro [5] (short-wave-length), and by Martín et al. [10] (long-wavelength)

$$\text{SO}: \quad \underline{v}_{\mathrm{L}} = \begin{bmatrix} 3.857143 \\ 2.629369 \\ 10.33333 \end{bmatrix}; \quad \underline{v}_{\mathrm{R}} = \begin{bmatrix} 1.000000 \\ 0.000000 \\ 1.000000 \end{bmatrix}; \quad A_\rho = 0.2; \quad \kappa_\rho = 5.0; \quad x_{\mathrm{SW}_0} = -4; \quad x \in [-5, +5] \tag{45a}$$

$$\text{TT}: \quad \underline{v}_{\mathrm{L}} = \begin{bmatrix} 1.515695 \\ 0.523346 \\ 1.805000 \end{bmatrix}; \quad \underline{v}_{\mathrm{R}} = \begin{bmatrix} 1.000000 \\ 0.000000 \\ 1.000000 \end{bmatrix}; \quad A_\rho = 0.1; \quad \kappa_\rho = 20\pi; \quad x_{\mathrm{SW}_0} = -1.5; \quad x \in [-5, +5] \tag{45b}$$

$$\text{MTWW}: \quad \underline{v}_{\mathrm{L}} = \begin{bmatrix} 0.635700 \\ 0.414200 \\ 1.401800 \end{bmatrix}; \quad \underline{v}_{\mathrm{R}} = \begin{bmatrix} 0.500000 \\ 0.000000 \\ 1.000000 \end{bmatrix}; \quad A_\rho = 0.1; \quad \kappa_\rho = 5.0; \quad x_{\mathrm{SW}_0} = -4; \quad x \in [-7, +3] \tag{45c}$$

The conditions (45a) for the Shu–Osher [27] problem are identical with the original paper [27], and computations were run until $t_{\mathrm{END}} = 1.8$ [27]. In the Shu–Osher [27] problem the inflow-Mach-number $M_i \approxeq 1.36$ is supersonic and there is no upstream propagation. On the contrary, in the Titarev–Toro [5] problem the inflow-Mach-number $M_i \approxeq 0.41$ is subsonic, and perturbations propagate upstream. With the original choice [5] $(x_{\mathrm{SW}_0}, t_{\mathrm{END}}) = (-2, 5)$, the upstream-travelling pressure-wave has reached the inflow-boundary at $t < t_{\mathrm{END}}$. If a no-change condition is applied at inflow, the pressure-wave is reflected at the upstream boundary. To avoid this we have chosen $(x_{\mathrm{SW}_0}, t_{\mathrm{END}}) = (-1.5, 4)$ (45b), which are the parameters allowing maximum t_{END}, without any wave reaching the boundaries. The same problem appears in the original choice of the Martín–Taylor–Wu–Weirs [10] problem, where $M_i \approxeq 0.24$, and we have simply shifted the computational domain (45c) to avoid reflexions at the boundaries. For all of the 3 test-cases (45) a no-change ($\underline{u}(x_{\mathrm{B}}, t) = \underline{u}_0(x_{\mathrm{B}})\ \forall t$) condition is applied at the boundaries.

The ICS (45) create [27,5,10] at $(x,t) = (x_{\mathrm{SW}_0}, 0)$ a right-propagating shock-wave, which interacts with the sinusoidal density-variation of the ICS (44), inducing, on the left of the shock-wave, a wavetrail at wavenumbers higher than the initial density-variation wavenumber κ_ρ (44). Grid-converged computations using the RORWENOM5 ($r=3$), RORWENOM11 ($r=6$), and RORWENOM17 schemes ($r=9$), with SSPRK(3,3) time-integration at CFL $= 0.6$, illustrate the solution of the 3 problems (Fig. 9). The ICS (45) without the density-variation ($A_\rho = 0$) are simple Riemann problems, and the corresponding shock-wave

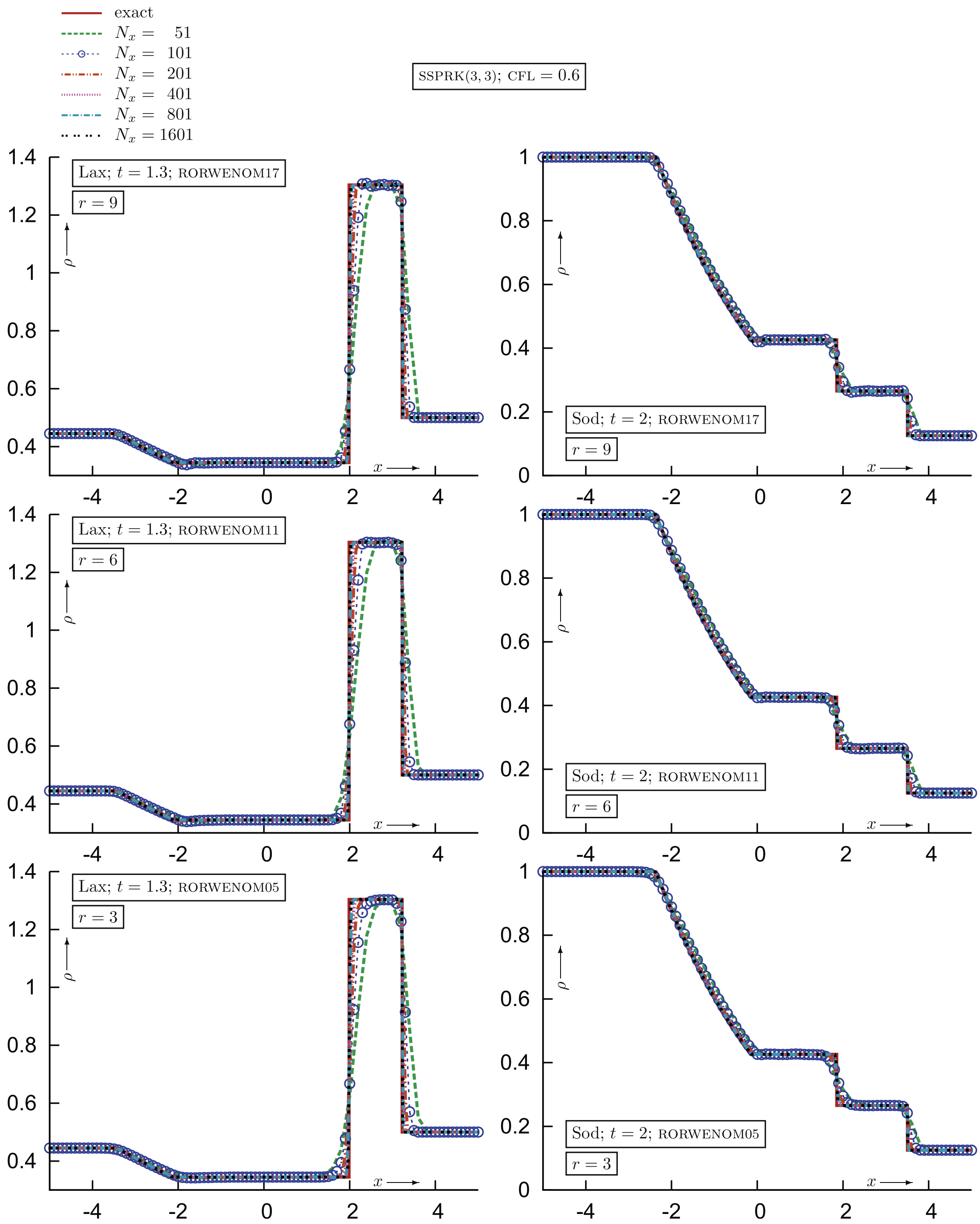

Fig. 8. Comparison of analytical solution [43] of the Riemann problems of Sod [25] (at $t = 2$) and of Lax [24] (at $t = 1.3$) with the numerical solution of the 1-D Euler equations, obtained with the RORWENOM5, the RORWENOM11, and the RORWENOM17 schemes, using SSPRK(3,3) time-integration [23] with CFL = 0.6, on progressively refined grids ($N_x = 51, 101, 201, 401, 801, 1601$ points).

Mach-numbers are $M_{SW_{SO}} \approxeq 3$ (Shu–Osher [27]), $M_{SW_{TT}} \approxeq 1.3$ (Titarev–Toro [5]), and $M_{SW_{MTWW}} \approxeq 1.16$ (Martín–Taylor–Wu–Weirs [10]). The original Shu–Osher [27] problem (45a) has the strongest shock-wave, and an intermediate wavetrail-wavelength (Fig. 9). The Martín–Taylor–Wu–Weirs [10] problem (45c) has the weakest shock-wave, and the longest wavetrail-wavelength (Fig. 9). It was introduced [10] to investigate situations where the density-gradients are of the same order as the shock-wave density-ratio, which might appear in compressible turbulence studies. Finally, the Titarev–Toro [5] problem

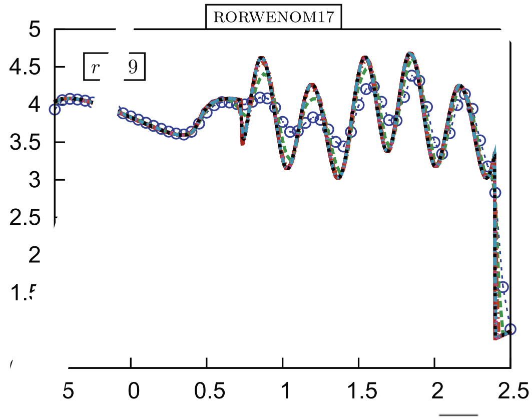

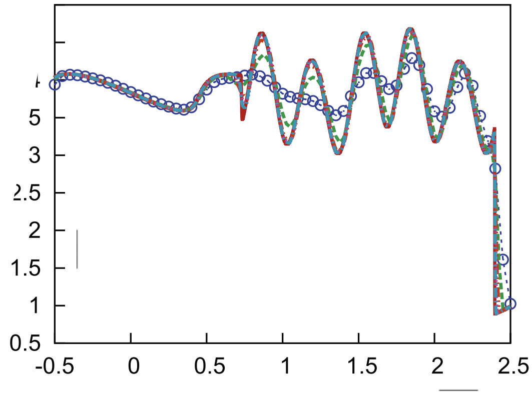

ıeous position of the shock-wave, $x_{\text{sw}}(t) - x$, increases (Fig. 10). On the $N_x = 401$ points grid, the RORWENOM17 scheme is ready almost grid-converged (Fig. 10). On this $N_x = 401$ points grid, the RORWENOM5 scheme resolves the high wavenumbers f the wavetrail, but underestimates their amplitude (the RORWENOM5 scheme resolution on the $N_x = 401$ points grid is similar o the resolution of the RORWENOM17 scheme on the twice coarser $N_x = 201$ points grid). Expectedly, the RORWENOM11 ($r = 6$) scheme gives results intermediate between the RORWENOM5 ($r = 3$) and the RORWENOM17 ($r = 9$) schemes (Fig. 10). As the mesh is refined, all of the 3 schemes converge to the same solution (Figs. 9 and 10), and remain perfectly ENO.

The modified (45c) Martín–Taylor–Wu–Weirs [10] problem was computed with the RORWENOM5 ($r = 3$), the RORWENOM11 ($r = 6$), and the RORWENOM17 ($r = 9$) schemes, using SSPRK(3,3) at CFL $= 0.6$, on different grids ($N_x = 51, 101, 201, 401, 801, 1601$ points), up to $t_{\text{END}} = 2$, and compared (Fig. 11) with the quasi-grid-converged solution (RORWENOM5; $N_x = 25,601$). The shock-wave being quite weak ($M_{\text{SW}_{\text{MTWW}}} \approxeq 1.16$), the dominant wavenumber of the wavetrail is only mar- ınally higher than the wavenumber κ_ρ (44) of the initial density-variation (Fig. 9). Even on the very coarse $N_x = 51$ points d, the dominant wavelength of the wavetrail is reasonably well predicted by all of the 3 schemes, while the amplitude diction is improved as r increases (Fig. 11). On this very coarse $N_x = 51$ points grid, the $O(1)$ discontinuities (at $- 3.3$ and at $x \approxeq -0.1$) cannot be resolved (Fig. 11). On the twice finer $N_x = 101$ points grid, the RORWENOM17 scheme dy almost grid-converged (except at the $O(1)$ discontinuities), while the RORWENOM5 slightly underestimates the ampli- ıe last peak, at $x \approxeq -2.7$ (Fig. 11). Again, expectedly, the RORWENOM11 ($r = 6$) scheme gives results intermediate be- RORWENOM5 ($r = 3$) and the RORWENOM17 ($r = 9$) schemes (Fig. 11). As the mesh is refined, all of the 3 schemes ıe same solution (Figs. 9 and 11), ultimately resolving the $O(1)$ discontinuities, and remain perfectly ENO.

(45b) Titarev–Toro [5] problem was computed with the RORWENOM5 ($r = 3$), the RORWENOM11 ($r = 6$), and the schemes, using SSPRK(3,3) at CFL $= 0.6$, on different grids ($N_x = 801, 1601, 3201, 6401, 12,801$ points), up red (Fig. 12) with the quasi-grid-converged solution (RORWENOM5; $N_x = 25,601$). The high wavenum- 9) impose stringent resolution requirements. As the distance from the instantaneous position increases, the prediction, on a given grid with a given scheme deteriorates (Fig. 12). On the RORWENOM5 scheme immediately ($x \in [4.6, 4.7]$) underestimates the amplitude of the wave- ıgth correctly only for $x \gtrsim 4.2$, while for $x \lesssim 4.2$ the increased

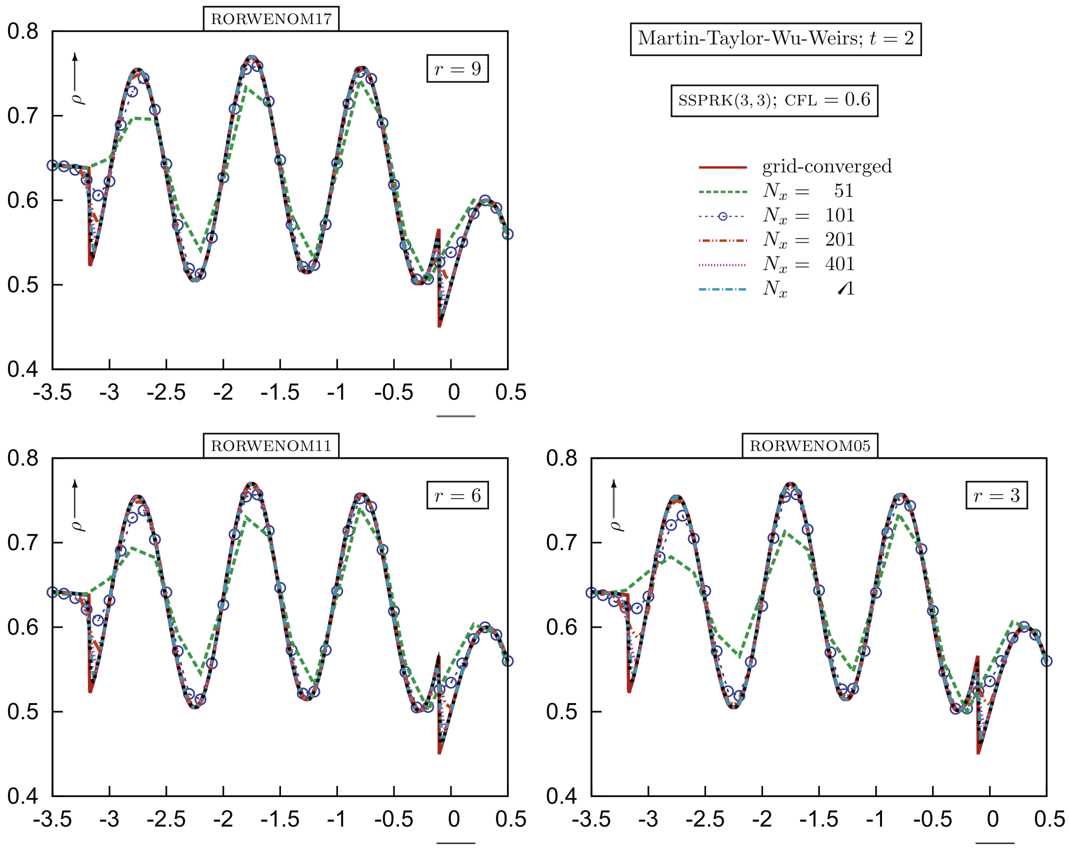

by the interaction are completely missed (Fig. 12). On this $N_x = 801$ points grid, the RORWENOM17 scheme (Fig. 12) satisfactorily predicts the amplitude for the first 2 wavelengths of the wavetrail ($4.5 \lessapprox x \lessapprox 4.7$), and correctly predicts the wavelength (albeit with underestimated amplitude) up to $x \approxeq 3.6$ (Fig. 12), largely improving upon the RORWENOM5 scheme, on the same $N_x = 801$ points grid. On the $N_x = 1601$ points grid (Fig. 12), all of the 3 schemes correctly predict the dominant wavelength of the wavetrail, for $x \gtrapprox 3.2$, but the RORWENOM17 scheme is much closer to the solution, predicting at $x \in [3.2, 3.3]$ an amplitude almost twice larger than the RORWENOM5 scheme (Fig. 12). Again, expectedly, the RORWENOM11 ($r = 6$) scheme gives results intermediate between the RORWENOM5 ($r = 3$) and the RORWENOM17 ($r = 9$) schemes (Fig. 12). As the mesh is refined, all of the 3 schemes converge to the same solution (Figs. 9 and 12), and remain perfectly ENO.

Grid-convergence (on the scale of the plot; Fig. 11) for the Martín–Taylor–Wu–Weirs [10] problem is obtained with $N_x = 801$ points, while $N_x = 1601$ (on the scale of the plot; Fig. 10) is necessary for the Shu–Osher [27] problem, indicating that the low-wavenumber (long-wavelength) case problem is the easiest. For the high-wavenumber (short-wavelength) case of the Titarev–Toro [5] problem grid-convergence is achieved at $N_x = 6401$ (on the scale of the plot; Fig. 12), demonstrating that the basic difficulty in predicting the shock-wave/entropy interaction problems is the correct spatial resolution of the high wavenumbers produced by the interaction. The underlying phenomenon (increase of the dominant wavenumber of the wavetrail compared to the initial density-variation wavenumber) becomes more pronounced as M_{sw} increases.

The previous numerical results on the shock-wave/entropy interaction problems (Figs. 9–12) demonstrate that the ROR procedure reduces the order of the reconstruction only locally (even for these rapidly varying, both in space and in time, problems), and that the accuracy of the RORWENOM$(2r-1)$ schemes does increase with r.

5.8.3. Woodward–Colella interacting blast-waves

Finally, we study the well known interacting blast-waves (IBWS) of Woodward and Colella [26], whose ICS are 2 Riemann problems

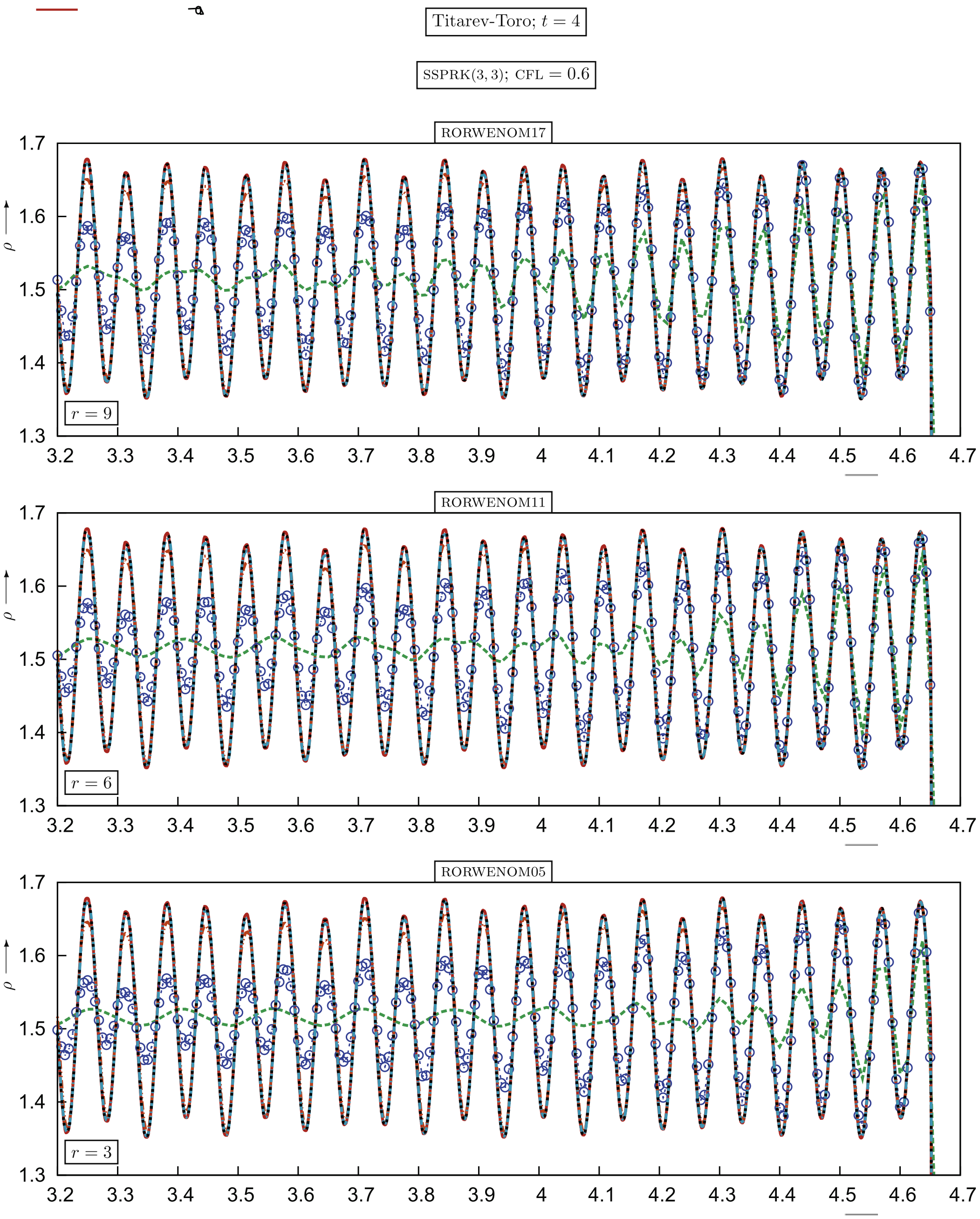

$$\underline{v}_0(x) = \begin{cases} [1, 0, 1000]^{\mathrm{T}}; & 0 \leqslant x < 0.1 \\ [1, 0, \frac{1}{100}]^{\mathrm{T}}; & 0.1 \leqslant x < 0.9\,; \quad x \in [0, 1] \\ [1, 0, 100]^{\mathrm{T}}; & 0.9 \leqslant x < 1 \end{cases} \tag{46}$$

in a shock-tube [26]

$$u = 0; \quad \frac{\partial \rho}{\partial x} = 0; \quad \frac{\partial p}{\partial x} = 0; \quad x = 0, 1 \ \forall t \tag{47}$$

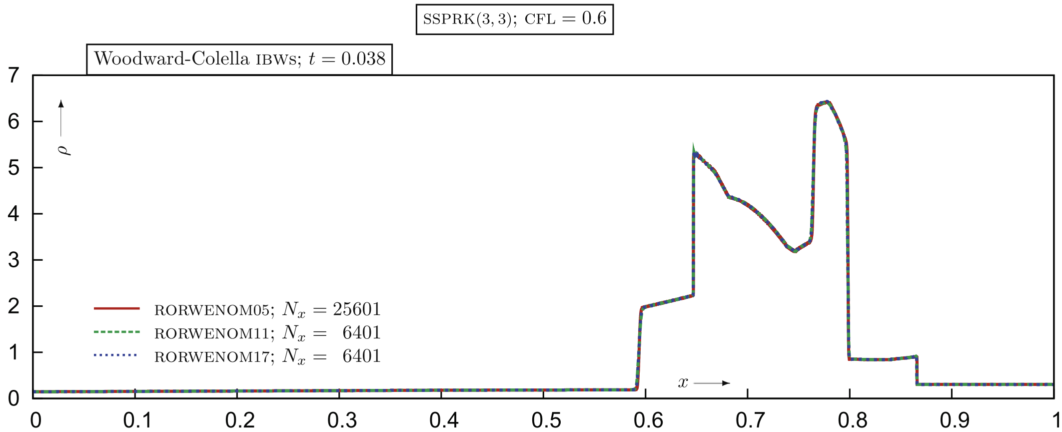

Fig. 13. Grid-converged solutions of the Woodward–Colella interacting blast-waves (IBWS) problem [26], at $t = 0.038$, obtained with the RORWENOM5, the RORWENOM11, and the RORWENOM17 schemes, using SSPRK(3,3) time-integration [23] of the 1-D Euler equations with CFL = 0.6.

This is a standard test-case, with very strong shock-waves (blast-waves), a right-propagating shock-wave at $(x,t) = (\frac{1}{10}, 0)$ ($M_{\text{SW}_\text{I}} \approxeq 199$) and a left-propagating shock-wave at $(x,t) = (\frac{9}{10}, 0)$ ($M_{\text{SW}_\text{II}} \approxeq 63$), and associated expansion-waves propagating in the opposite directions. The complex interactions which take place (Fig. 13) are described in detail in the original paper of Woodward and Colella [26].

The Woodward–Colella [26] problem was computed with the RORWENOM5 ($r = 3$), the RORWENOM 11 ($r = 6$), and the RORWENOM17 ($r = 9$) schemes, using SSPRK(3,3) at CFL = 0.6, on different grids ($N_x = 201, 401, 801$ points), up to $t_{\text{END}} = 0.038$, and compared (Fig. 14) with the quasi-grid-converged solution (RORWENOM5; $N_x = 25,601$; Fig. 13). On the coarsest $N_x = 201$ points grid, the RORWENOM17 and the RORWENOM11 schemes, although far from the quasi-grid-converged solution (Fig. 14), predict the main flow features, including the local minimum of ρ at $x \in [0.72, 0.76]$, which is not clearly visible in the RORWENOM5 solution on this grid (Fig. 14). Furthermore, the discontinuity at $x \approxeq 0.6$ is smeared in the RORWENOM5 ($r = 3$) solution on the coarse $N_x = 201$ points grid (Fig. 14), and is progressively sharpenned as r increases up to the RORWENOM17 ($r = 9$) scheme (Fig. 14). On the twice finer $N_x = 401$ points grid, the agreement with the quasi-grid-converged solution is improved (Fig. 14). The RORWENOM17 ($r = 9$) scheme on this grid ($N_x = 401$) predicts the correct value of the local maximum of ρ at $x \approxeq 0.65$, while it starts approaching the correct value of the local minimum of ρ in the region $\in [0.72, 0.76]$ (the RORWENOM17 scheme is halfway between the prediction of the RORWENOM5 scheme, on this $N_x = 401$ points grid, and the quasi-grid-converged value). Furthermore, the quasi-grid-converged value of the density-maximum at $x \approxeq 0.78$ is being approached by the RORWENOM17 scheme on the $N_x = 401$ points grid (Fig. 14), while its value is underestimated by the RORWENOM5 scheme, whose solution on the $N_x = 401$ points grid is quite close to the RORWENOM17 solution on the twice coarser $N_x = 201$ points grid (Fig. 14).

Finally, on the $N_x = 801$ points grid (Fig. 14), the solution of the RORWENOM17 scheme is very close to the quasi-grid-converged solution. The results of the RORWENOM5 scheme, on the $N_x = 801$ points grid, are close to the results of the RORWENOM17 scheme on the twice coarser $N_x = 401$ points grid (Fig. 14). As usual, the RORWENOM11 ($r = 6$) scheme gives results intermediate between the RORWENOM5 ($r = 3$) and the RORWENOM17 ($r = 9$) schemes (Fig. 14). As the mesh is refined, all of the 3 schemes converge to the same solution (Fig. 13), and remain reasonably ENO (indeed slight oscillations eventually present in the solution diminish as $\Delta x \to 0$).

6. Linewise multidimensional extension

The best way to extend the very-high-order WENO methods to 2-D and 3-D problems would be to use multidimensional reconstruction [45,5,46]. Both for structured [5] and for unstructured [45,46] grids, these techniques use a finite-volume approach and aim at obtaining a high-order reconstruction of the solution at appropriately chosen Gauss-integration points on the control-volume. For structured grids, the technique of Titarev and Toro [5], consists of successive linewise reconstructions, and can be easily extended to higher-orders. In a recent work, Dumbser et al. [47] have further shown that multidimensional finite-volume approaches can be considered as a particular case of a unified framework of discontinuous Galerkin approaches.

The study and development of very-high-order multidimensional reconstruction is beyond the scope of the present paper. We use instead a baseline linewise extension of the method to 2-D, with the aim of checking accuracy and nonoscillatory performance for 2-D problems. This extension can be viewed as a finite-difference [2,3] approach (on Cartesian grids), although it has been implemented as an unsplit finite-volume method [43, pp. 521–526], for non-Cartesian meshes. What is important is that we do not use any dimensional-splitting approach for the time-inte-

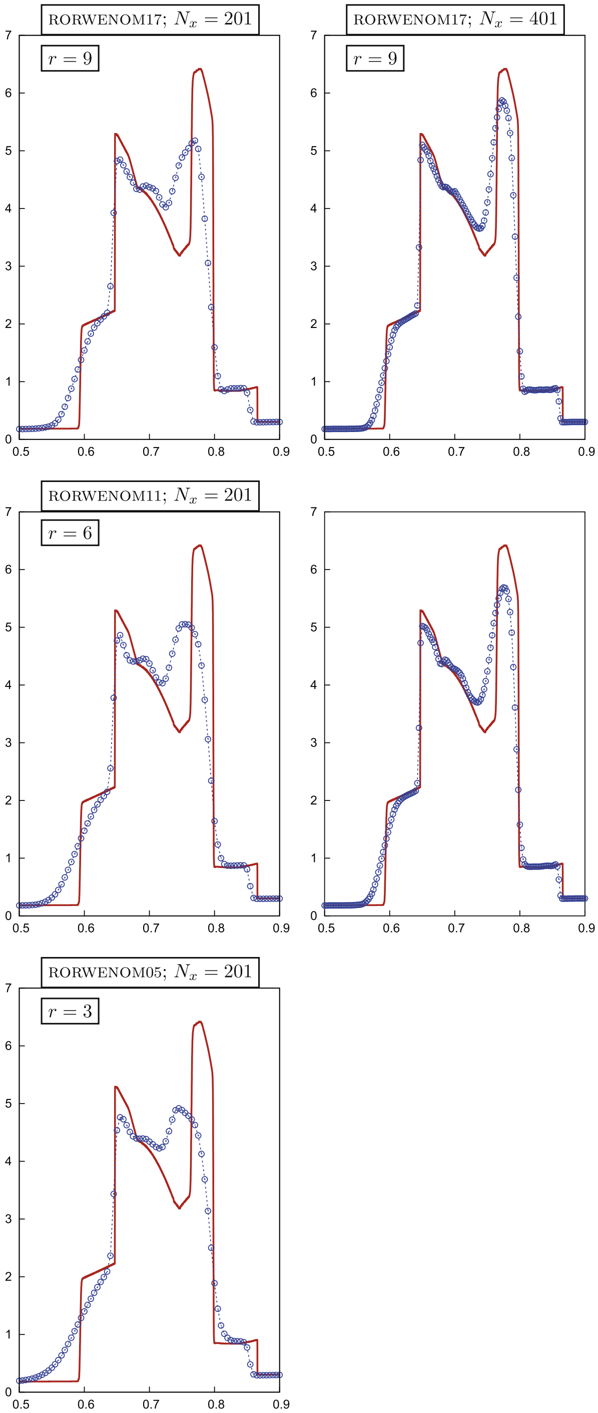

gration [43, pp. 510–520], but instead follow a method of lines approach [23,27], where we compute the multidimensional space-discretized operator, and then apply an appropriate time-integration scheme for the semidiscrete equation.

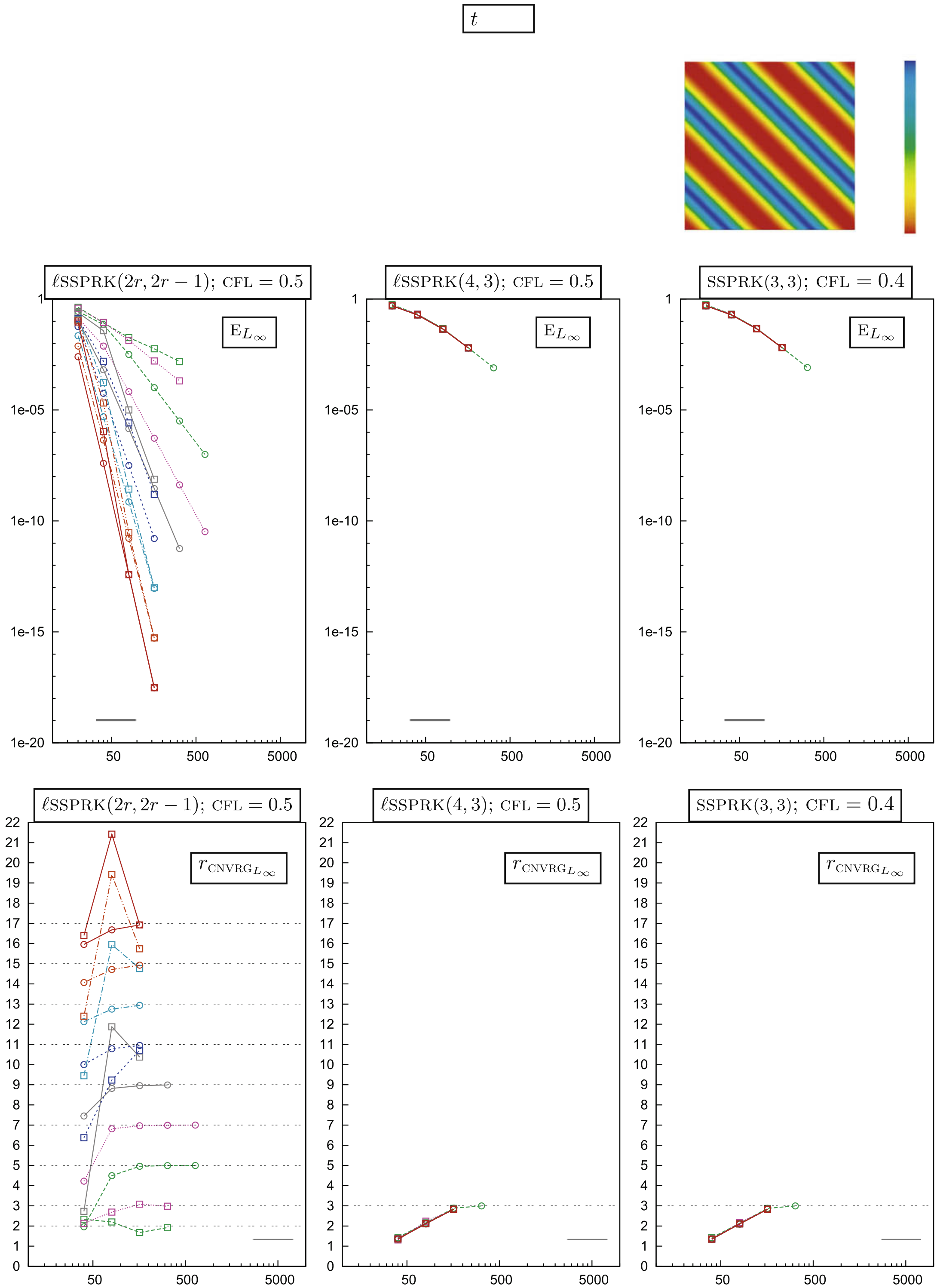

t
ℓSSPRK$(2r, 2r-1)$; CFL $= 0.5$
ℓSSPRK$(4, 3)$; CFL $= 0.5$
SSPRK$(3, 3)$; CFL $= 0.4$
E_{L_∞}
1
1e-05
1e-10
1e-15
1e-20
50
500
5000
ℓSSPRK$(2r, 2r-1)$; CFL $= 0.5$
ℓSSPRK$(4, 3)$; CFL $= 0.5$
SSPRK$(3, 3)$; CFL $= 0.4$
$r_{\mathrm{CNVRG}_{L_\infty}}$
0 1 2 3 4 5 6 7 8 9 10 11 12 13 14 15 16 17 18 19 20 21 22
50
500
5000

7. 2-D Advection equation

7.1. The 2-D advection equation with periodic boundary-conditions

To check the accuracy of the schemes in the 2-D case, we study the advection equation [45,3]

$$\frac{\partial u}{\partial t}+\frac{\partial u}{\partial x}+\frac{\partial u}{\partial y}=0;\quad \begin{cases} x\in[-1,1] \\ y\in[-1,1]\end{cases} \tag{48a}$$

$$u(t,x=-1,y)=u(t,x=+1,y) \tag{48b}$$

$$u(t,x,y=-1)=u(t,x,y=+1) \tag{48c}$$

$$u(t=0,x,y)=u_0(x,y) \tag{48d}$$

with periodic boundary-conditions (BCs), both x-wise and y-wise, and different initial conditions (ICs) $u_0(x,y)$. The periodicity conditions are applied, as in the 1-D case (Section 3.1), by adding, at the boundaries of the computational domain ($x\notin[-1,1]$ or $y\notin[-1,1]$), $N_{\text{PH}}=r$ phantom nodes, for the $(2r-1)$-order scheme (Section 2.4), thus preserving the linewise $O(\Delta x^{2r-1})$ spatial accuracy of the scheme.

7.2. Space- and time-discretization

On a Cartesian homogeneous grid, the 2-D advection equation (48) is semi-discretized

$$\frac{du_{i,j}}{dt}=-\left(\frac{u^{\text{L}}_{i+\frac{1}{2},j}-u^{\text{L}}_{i-\frac{1}{2},j}}{\Delta x}+\frac{u^{\text{L}}_{i,j+\frac{1}{2}}-u^{\text{L}}_{i,j-\frac{1}{2}}}{\Delta y}\right) \tag{49}$$

where the $u^{\text{L}}_{i\pm\frac{1}{2},j}$ and $u^{\text{L}}_{i,j\pm\frac{1}{2}}$ are obtained by 1-D reconstruction (Section 2) along the corresponding grid-lines (x-wise and y-wise, respectively). Then, the unsplit semi-discrete equation (49) is integrated in time with an appropriate RK technique [23,27,37–40].

7.3. Test-cases

The performance and order-of-accuracy of the various schemes is studied by comparing with the exact solution of the 2-D advection equation (48) for different initial conditions (ICs). All of the computations used the corresponding ℓSSPRK$(2r,2r-1)$ time-discretization [37–39]. In view of the results obtained for the 1-D case (cf. Section 3), we only consider UW$(2r-1)$ (Section 2.2) and WENOM$(2r-1)$ (with $p_\beta=r$; Section 2.3) schemes for the space-discretization. The computations were performed using 128-bit arithmetic (quadruple precision; `real*16` [41]).

7.3.1. $u_0(x,y)=\sin(\pi(x+y))$

We computed this test-case [45], using the UW$(2r-1)$, and the WENOM$(2r-1)$ schemes, with $p_\beta=r$ (Fig. 15). The wave was advected 10 times through the computational domain, using ℓSSPRK$(2r,2r-1)$ time-discretization with CFL $=0.5$ (the d-D stability limit for the advection equation being d^{-1} [5]). This test-case is relatively easy, since at the critical point $n_{\text{CP}}=1$ (Section 3.4). As a consequence, the mapping procedure of the WENOM schemes [4] is sufficient to give results almost identical with the corresponding UW$(2r-1)$ scheme, already at the coarsest ($N_x\times N_y=21\times21$) grid (Fig. 15). The L_∞-norm of the error [4] E_{L_∞} reaches almost immediately the theoretical rate-of-convergence [2,4] $r_{\text{CNVRG}_{L_\infty}}=2r-1$, as the number of cells $N_c=N_x-1=N_y-1$ increases. The result is significant in that it provides systematic verification of previous observation by Balsara and Shu [3] that the unsplit 2-D linewise extension of the very-high-order upwind and WENOM schemes returns the theoretical order-of-accuracy of the 1-D tests, for the scalar linear advection equation (48).

7.3.2. $u_0(x)=\sin^4(\pi(x+y))$

This wave is more complex because the degree of the critical points [4] is $n_{\text{CP}}=3$. We computed this test-case, using the UW$(2r-1)$, and the WENOM$(2r-1)$ schemes, with $p_\beta=r$ (Fig. 16). The wave was advected 10 times through the computational domain, using ℓSSPRK$(2r,2r-1)$ time-discretization with CFL $=0.5$. The results (Fig. 16) are quite similar with those obtained for the $n_{\text{CP}}=3$ 1-D case (Section 3.4.2; Fig. 4). As the number of cells $N_c=N_x-1=N_y-1$ increases all of the UW$(2r-1)$ reach the theoretical rate-of-convergence [2,4] $r_{\text{CNVRG}_{L_\infty}}=2r-1$. The WENOM$(2r-1)$, as N_c increases, tend to the corresponding UW$(2r-1)$ scheme, for $r\geqslant5$ (Fig. 16). Because of the high value of $n_{\text{CP}}=3$, the WENOM5 and WENOM7 schemes are limited to $r_{\text{CNVRG}_{L_\infty}}=2$ and $r_{\text{CNVRG}_{L_\infty}}=3$ (Fig. 16). These results (Fig. 16) further substantiate the conjecture that the unsplit 2-D linewise extension of the very-high-order upwind and WENOM schemes returns the theoretical order-of-accuracy of the 1-D tests, for the scalar linear advection equation (48).

7.4. Importance of temporal discretization

The accuracy-tests for the 1-D (Figs. 3 and 4) and 2-D (Figs. 15 and 16) advection equation, which demonstrated that the very-high-order UW, WENO and WENOM discretizations correctly restore the theoretical rates-of-convergence with grid-refinement, were all run using linear strong-stability-preserving Runge–Kutta algorithms ℓSSPRK$(2r, 2r-1)$, which are SSP and $O(\Delta t^{2r-1})$ for linear problems [37–39]. In this way the temporal accuracy is of the same order as the spatial discretization, at the expense of performing $M_{\text{RK}} = 2r$ Runge–Kutta-steps.

To highlight the importance of combined temporal and spatial accuracy in obtaining the theoretical rate-of-convergence, we re-run the 2-D test-cases (Figs. 15 and 16) using the linearly $O(\Delta t^3)$ ℓSSPRK$(4,3)$ method [37–39], as well as the Shu–Osher [23] SSPRK$(3,3)$, which is $O(\Delta t^3)$ both for linear and for general nonlinear problems. All the computations with the ℓSSPRK$(2r, 2r-1)$ methods [37–39], including those of the different space-discretizations combined with the ℓSSPRK$(4,3)$ time-integration, were run with $\text{CFL} := \Delta t \Delta x^{-1} = \Delta t \Delta y^{-1} = 0.5$. When using the nonlinearly accurate SSPRK$(3,3)$ method [23], $\text{CFL} = 0.5$ was beyond the limit of stability for $r \geqslant 8$ (but worked perfectly well for $r \leqslant 7$). We therefore run the SSPRK$(3,3)$ tests for the 2-D advection equation with $\text{CFL} = 0.4$

The computations for the test-case $u_0(x,y) = \sin(\pi(x+y))$ (Section 7.3.1), using the ℓSSPRK$(2r, 2r-1)$ in conjunction with the UW$(2r-1)$ or the WENOM$(2r-1)$ space-discretizations readily restore the theoretical rate-of-convergence $r_{\text{CNVRG}_{L_\infty}} = 2r-1$ (Section 7.3.1), the UW17 scheme reaching $\text{E}_{L_\infty} \approxeq 10^{-28}$ on a grid where the the UW5 scheme yields $\text{E}_{L_\infty} \approxeq 10^{-8}$. The negative effect on accuracy of using the $O(\Delta t^3)$ ℓSSPRK$(4,3)$ method [37–39] is spectacular (Fig. 15), in that we obtain nearly identical results, on a given grid, whatever the spatial discretization used. The error is completely controlled by the low-order time-integration method (for the test-case at hand; $u_0(x,y) = \sin(\pi(x+y))$). All the space-discretizations, in conjunction with the $O(\Delta t^3)$ ℓSSPRK$(4,3)$ method return $r_{\text{CNVRG}_{L_\infty}} = 3$. The same conclusions as for the linearly accurate ℓSSPRK$(4,3)$ method apply to the results obtained using the SSPRK$(3,3)$ method (Fig. 15). For this simple IC, with $n_{\text{CP}} = 1$ [4], there is virtually no difference in the results obtained using the UW$(2r-1)$ or the WENOM$(2r-1)$ space-discretizations. Notice that the results for $r = 3, \ldots, 9$ with the ℓSSPRK$(4,3)$ and the SSPRK$(3,3)$ methods are all plotted, and practically collapse on a single curve (Fig. 15).

Similar observations (Fig. 16) on the influence of the time-integration method apply to the test-case $u_0(x,y) = \sin^4(\pi(x+y))$ (Section 7.3.2). Again the results for $r = 3, \ldots, 9$ with the ℓSSPRK$(4,3)$ and the SSPRK$(3,3)$ methods are all plotted, and practically collapse on a single curve (Fig. 16). Notice that up to the $N_x \times N_y = 161 \times 161$ grid, when using the ℓSSPRK$(4,3)$ or the SSPRK$(3,3)$ methods, the rate-of-convergence of the WENOM5 (respectively, WENOM7) scheme is the same as for the higher-order schemes or for the corresponding UW5 (respectively, UW7) scheme (Fig. 16), while when using the ℓSSPRK$(6,5)$ (respectively, ℓSSPRK$(8,7)$) method we obtain (Fig. 16) $r_{\text{CNVRG}_{L_\infty}} = 2$ for the WENOM5 (respectively, $r_{\text{CNVRG}_{L_\infty}} = 3$ for the WENOM7) scheme. This is simlply a superconvergence accident [2,4], the error-levels with the ℓSSPRK$(4,3)$ or the SSPRK$(3,3)$ methods being higher than the corresponding error-levels with the ℓSSPRK$(2r, 2r-1)$ methods (Fig. 16).

In view of accuracy studies with the 2-D nonlinear Euler equations (Section 8.2), using the SSPRK$(3,3)$ time-integration method, it it important to notice that for the $u_0(x,y) = \sin^4(\pi(x+y))$ test-case (Fig. 16), which contains critical points with high $n_{\text{CP}} = 3$ [4], the rate-of-convergence obtained by the SSPRK$(3,3)$ time-integration method is initially only $r_{\text{CNVRG}_{L_\infty}} = 1$, progressively increasing to $r_{\text{CNVRG}_{L_\infty}} = 3$ with increasing N_c (Fig. 16).

8. 2-D Euler equations

8.1. System of the 2-D Euler equations

To assess the peformance of the high-order WENO reconstruction for multidimensional nonlinear problems, we further consider its application to the 2-D Euler equations [43]

$$\frac{\partial \underline{u}}{\partial t} + \frac{\partial \underline{F}_x(\underline{u})}{\partial x} + \frac{\partial \underline{F}_y(\underline{u})}{\partial y} = 0 \iff \frac{\partial}{\partial t}\begin{bmatrix} \rho \\ \rho u \\ \rho v \\ \rho e_t \end{bmatrix} + \frac{\partial}{\partial x}\begin{bmatrix} \rho u \\ \rho u^2 + p \\ \rho u v \\ \rho u h_t \end{bmatrix} + \frac{\partial}{\partial y}\begin{bmatrix} \rho v \\ \rho v u \\ \rho v^2 + p \\ \rho v h_t \end{bmatrix} = 0 \tag{50}$$

where $\underline{u} = [\rho, \rho u, \rho v, \rho e_t]^{\text{T}}$ is the vector of conservative variables, $\underline{F}_x(\underline{u}) = [\rho u, \rho u^2 + p, \rho u v, \rho u h_t]^{\text{T}}$ is the x-wise-flux component, $\underline{F}_y(\underline{u}) = [\rho v, \rho v u, \rho v^2 + p, \rho v h_t]^{\text{T}}$ is the y-wise-flux component, ρ is the density, u is the x-wise-velocity component, v is the y-wise-velocity component, p is the pressure, $e_t = e + \frac{1}{2}(u^2 + v^2)$ is the total internal energy, e is the internal energy, $h_t = h + \frac{1}{2}(u^2 + v^2)$ is the total enthalpy, $h = e + p\rho^{-1}$ is the enthalpy. We assume perfect gas thermodynamics, with

$$p = (\gamma - 1)\rho\left(e_t - \frac{1}{2}(u^2 + v^2)\right) = \frac{\gamma - 1}{\gamma}\rho\left(h_t - \frac{1}{2}(u^2 + v^2)\right); \quad a = \sqrt{\gamma \frac{p}{\rho}} \tag{51}$$

where a is the speed-of-sound [43]. We will note

$$\underline{v} := \begin{bmatrix} \rho \\ u \\ v \\ p \end{bmatrix} \tag{52}$$

the vector of primitive variables. For all of the test-cases studied $\gamma = 1.4$.

8.2. Linewise extension of the numerical method to 2-D

As for the 2-D advection equation, the linewise extension of the method to the 2-D Euler equations uses RORWENOM reconstruction of the characteristic variables (Section 5.5), along grid-lines. The Godunov flux is computed using an exact Riemann solver, where the tangential-to-the-cell-interface velocity is treated as a passively convected quantity [43, pp. 149–150]. The matrices $\underline{\underline{L}}\left(\underline{u}^{\text{AVG}}_{i+\frac{1}{2},j}\right)$ and $\underline{\underline{R}}\left(\underline{u}^{\text{AVG}}_{i+\frac{1}{2},j}\right)$ $\left(\text{respectively, } \underline{\underline{L}}\left(\underline{u}^{\text{AVG}}_{i,j+\frac{1}{2}}\right) \text{ and } \underline{\underline{R}}\left(\underline{u}^{\text{AVG}}_{i,j+\frac{1}{2}}\right)\right)$ of the left and right eigenvectors used to define the local characteristic variables (Section 5.3) are given, for the general 3-D case with arbitrary cell-interface orientation, in [48] (they can be simplified in an ifless construction for the 2-D case [12,48], but we used the general 3-D expressions in the present work). The resulting semi-discrete scheme is integrated in time using the SSPRK(3,3) method of Shu and Osher [23].

The stability-time-step is computed as

$$\Delta t = \text{CFL} \min_{i,j}\left(\frac{\Delta\ell_{i,j}}{\mathsf{s}_{\max_{i,j}}}\right); \quad \mathsf{s}_{\max_{i,j}} = \max\left(\left[\mathsf{s}_{\max_{i+\frac{1}{2},j}}, \mathsf{s}_{\max_{i-\frac{1}{2},j}}, \mathsf{s}_{\max_{i,j+\frac{1}{2}}}, \mathsf{s}_{\max_{i,j-\frac{1}{2}}}, V_{i,j} + a_{i,j}\right]\right) \tag{53}$$

where $\mathsf{s}_{\max_{i+\frac{1}{2},j}}$, $\mathsf{s}_{\max_{i-\frac{1}{2},j}}$, $\mathsf{s}_{\max_{i,j+\frac{1}{2}}}$, $\mathsf{s}_{\max_{i,j-\frac{1}{2}}}$ are the maximum wavespeeds of the Riemann-problems at the corresponding cell-interfaces, $V := \sqrt{u^2 + v^2}$ is the flow velocity, and a is the speed-of-sound. The cell-size is computed as the radius of the circle inscribed into the control-volume, and for the Cartesian homogeneous grids used is $\Delta\ell = \frac{1}{\sqrt{2}}\Delta x = \frac{1}{\sqrt{2}}\Delta y$.

8.3. Typical 2-D test-cases

8.3.1. Shu convection of a smooth compressible vortex

This test problem, introduced by Shu [28] and Balsara and Shu [3], studies the convection of a smooth compressible vortex, in supersonic flow. It is interesting in that an exact solution of the flow is available [28], allowing scheme order-of-accuracy testing [3,5]. Shu [28] has used the field

$$\underline{v}_{\text{VRTX}}(x, y; x_{\text{VRTX}}, y_{\text{VRTX}}) := \begin{bmatrix} \rho_0\left(\frac{T}{T_0}\right)^{\frac{1}{\gamma-1}} \\ -V_{\text{VRTX}}\frac{y}{r_c} \\ +V_{\text{VRTX}}\frac{x}{r_c} \\ p_0\left(\frac{T}{T_0}\right)^{\frac{\gamma}{\gamma-1}} \end{bmatrix} \tag{54a}$$

$$r := \sqrt{(x - x_{\text{VRTX}})^2 + (y - y_{\text{VRTX}})^2} \tag{54b}$$

$$V_{\text{VRTX}} := A_{\text{VRTX}} \exp\left(B_{\text{VRTX}}\left(1 - \frac{r^2}{r_c^2}\right)\right) \tag{54c}$$

$$T := T_0 - \frac{\gamma - 1}{\gamma R_g}\frac{A^2_{\text{VRTX}}}{4B_{\text{VRTX}}} \exp\left(2B_{\text{VRTX}}\left(1 - \frac{r^2}{r_c^2}\right)\right) \tag{54d}$$

$$r_c = \text{const}; \quad A_{\text{VRTX}} = \text{const}; \quad B_{\text{VRTX}} = \text{const}; \quad \rho_0 = \text{const}; \quad T_0 = \text{const}; \quad p_0 = \text{const} \tag{54e}$$

to describe an homentropic ($s = \text{const}\ \forall x, y, t$) vortex centered at point $(x_{\text{VRTX}}, y_{\text{VRTX}})$, and remarked that (54), is an exact solution of the steady 2-D Euler equations (50), provided $(d_t x_{\text{VRTX}} = 0, d_t y_{\text{VRTX}} = 0)$, as can be verified by substituting (54) into (50). Shu [28] also remarked that the flow with initial conditions

$$\underline{v}_{\text{IC}}(x, y) = \begin{bmatrix} 0 \\ u_0 \\ v_0 \\ 0 \end{bmatrix} + \underline{v}_{\text{VRTX}}(x, y; x_{\text{VRTX}_0}, y_{\text{VRTX}_0}); \quad u_0 = \text{const}; \quad v_0 = \text{const} \tag{55}$$

in an unbounded domain, admits as exact solution the passive advection of the vortex with velocity $\vec{V}_0 = u_0\vec{e}_x + v_0\vec{e}_y$

$$\underline{v}(x, y, t) = \begin{bmatrix} 0 \\ u_0 \\ v_0 \\ 0 \end{bmatrix} + \underline{v}_{\text{VRTX}}(x, y; x_{\text{VRTX}}(t), y_{\text{VRTX}}(t)); \quad \begin{cases} x_{\text{VRTX}}(t) = x_{\text{VRTX}_0} + u_0 t \\ y_{\text{VRTX}}(t) = y_{\text{VRTX}_0} + v_0 t \end{cases} \tag{56}$$

The values of the constants used for the accuracy studies are [28,45,3,5]

$$r_c = 1; \quad A_{\text{VRTX}} = \frac{5}{2\pi}; \quad B_{\text{VRTX}} = \frac{1}{2}; \quad \rho_0 = 1; \quad T_0 = 1; \quad p_0 = 1; \quad u_0 = 1; \quad v_0 = 1 \tag{57}$$

To avoid the use of a large computational domain (and corresponding large CPU-times), many authors [28,45,3,5] have run this problem in a small computational domain $(-5 \leqslant x \leqslant +5, -5 \leqslant y \leqslant +5)$, with periodic boundary-conditions, and have obtained quite satisfactory results for small times ($t_{\text{END}} = 10$, corresponding to the advection of the vortex once across the diagonal of the computational domain). The periodic problem corresponds to the dynamics of an infinite array of vortices located at $x_{\text{VRTX},\ell}(t) = x_{\text{VRTX}_0} + \ell L_x + u_0 t$ and $y_{\text{VRTX},m}(t) = y_{\text{VRTX}_0} + mL_y + v_0 t$ ($\forall \ell, m \in \mathbb{Z}$), where $L_x = L_y$ is the size of the square computational domain, while the velocity-field of (56) is not periodic. However, (55) is a very good approximation of the solution of the periodic problem, for small times ($t_{\text{END}} = 10$), allowing usefull comparisons for the evaluation of the accuracy

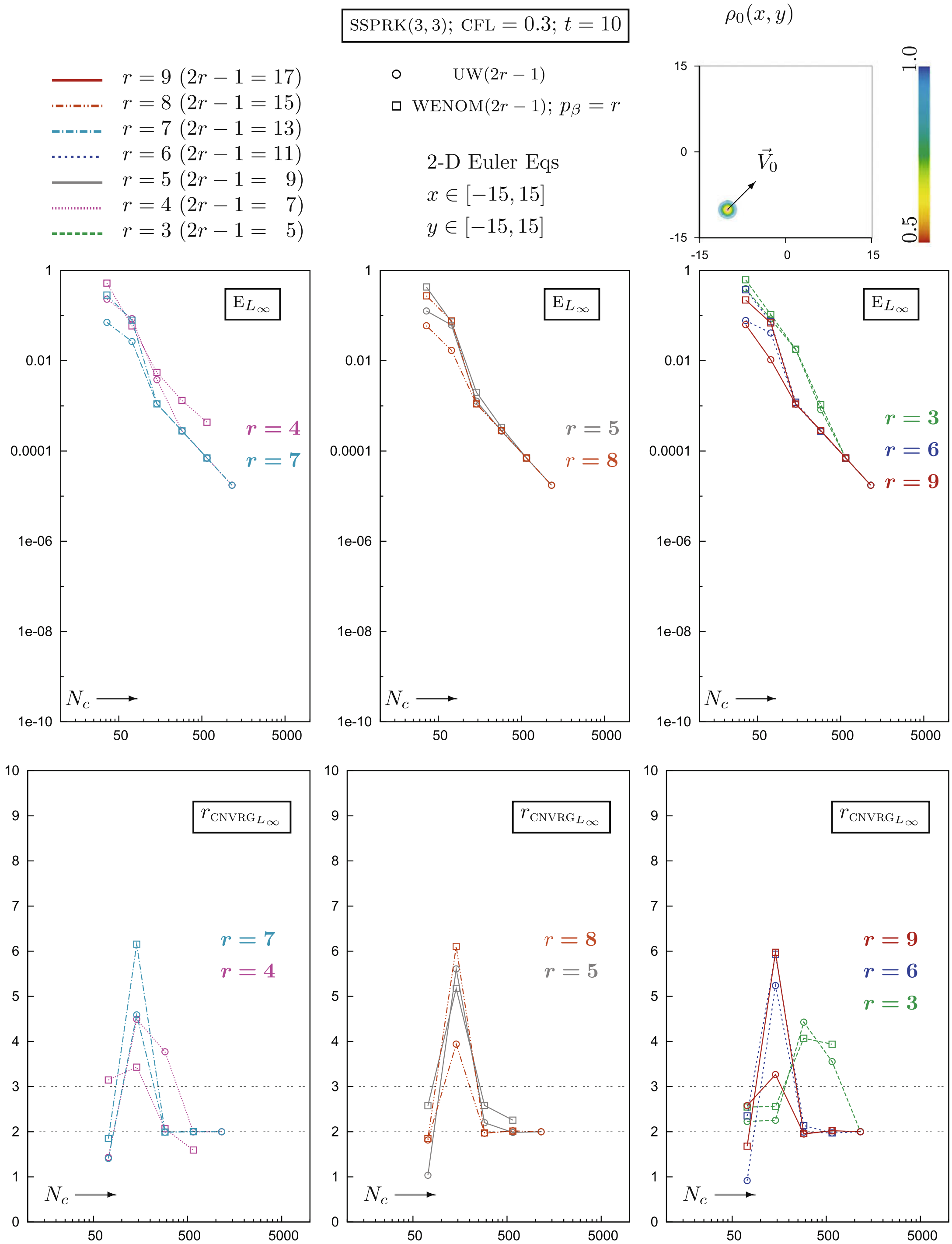

Fig. 17. L_∞-norm error E_{L_∞} and rate-of-convergence $r_{\text{CNVRG}_{L_\infty}}$, as a function of the number of grid-cells in each direction $N_c = N_x - 1 = N_y - 1$, for the UW$(2r-1)$ and WENOM$(2r-1)$ ($p_\beta = r$) reconstructions ($r = 3, \ldots, 9$), for the convection of the Shu [28] smooth vortex (56) by the 2-D Euler equations (50) ($x \in [-15, 15], y \in [-15, 15]$), at $t = 10$, with unbounded-domain BCS, using SSPRK(3,3) time-integration [23] with CFL = 0.3.

of numerical schemes [28,45,3,5]. To avoid this approximation we have run the problem of the convection of the smooth vortex (56) in a larger computational domain ($-15 \leqslant x \leqslant +15, -15 \leqslant y \leqslant +15$), with nonperiodic BCs. At $t = 0$ the vortex is located at $(x_{\text{VRTX}_0}, y_{\text{VRTX}_0}) = (-10, -10)$ and the flowfield is initialized by (55). To mimic the conditions of an unbounded domain, at the boundaries of the computational domain ($x = \pm 15$ or $y = \pm 15$) we add N_{PH} phantom nodes (Section 2.4), which are updated at each RK step by the exact solution (56).

For nonlinear equations, such as the Euler equations (50) very-high-order-accurate SSP time-integration methods (up to $O(\Delta t^{17})$) are not, at present, available [23,27,37–40]. To run order-of-accuracy studies, with the very-high-order space-accurate schemes, it would be necessary to reduce the time-step, as the computational grid is refined in space, so as to recover uniformly (in time and space) $(2r-1)$-order accuracy [3,5]. To this purpose, when using an $O(\Delta t$

$$\frac{\partial v}{\partial x} = 0; \quad x = \pm\frac{1}{2}; \quad \forall t, y \tag{59a}$$

$$\frac{\partial v}{\partial y} = 0; \quad y = \pm\frac{1}{2}; \quad \forall t, x \tag{59b}$$

The Lax–Liu [29] 2-D Riemann problem #5 (2DRP05) was computed with the RORWENOM5 ($r = 3$), the RORWENOM11 ($r = 6$), and the RORWENOM17 ($r = 9$) schemes, using SSPRK(3,3) at CFL $= 0.6$, on different grids ($N_x = N_y = 101, 201, 401, 801$ points), up to

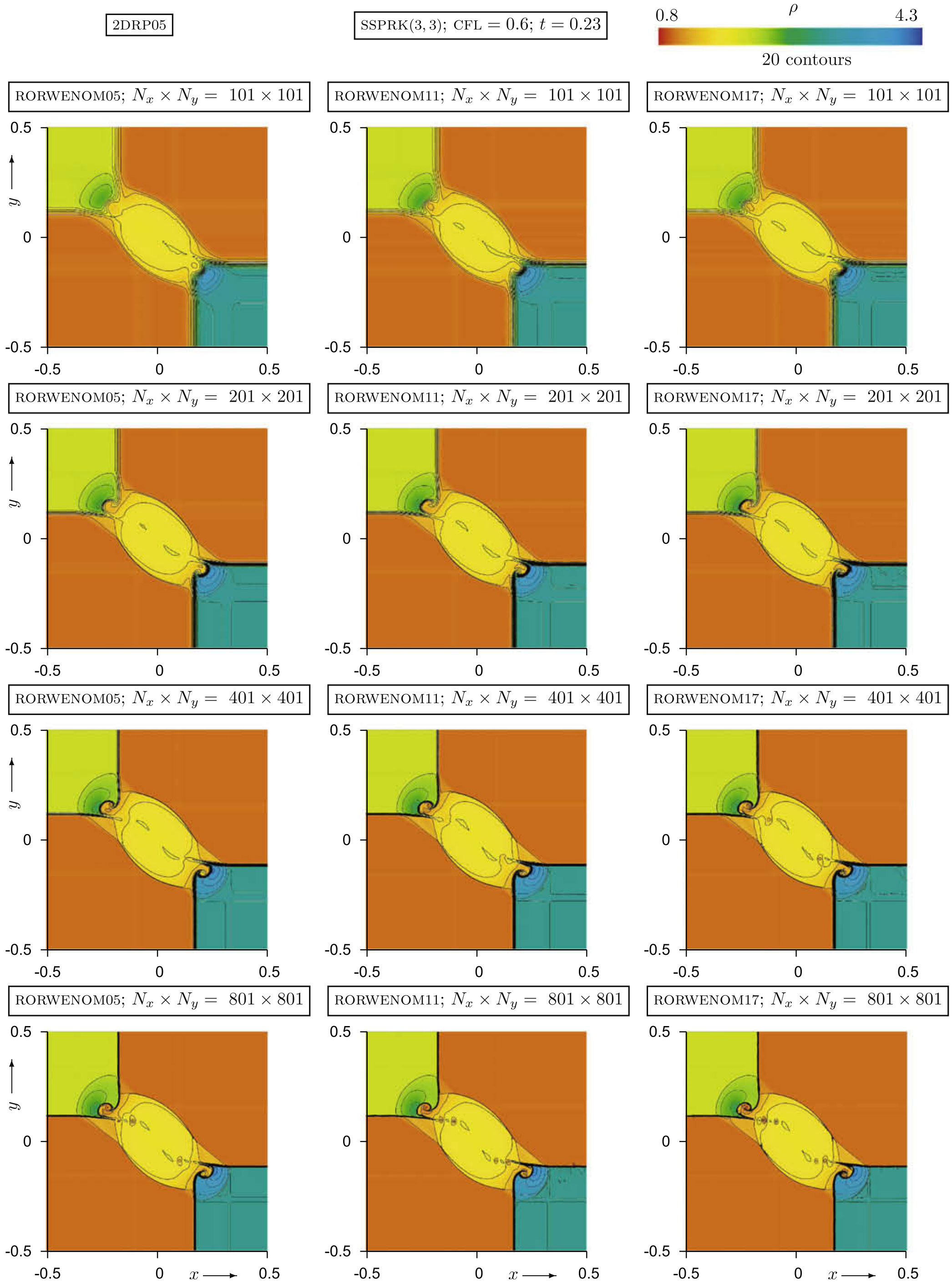

Fig. 18. Comparison, at $t = 0.23$, of the numerical solution of the 2-D Euler equations, for the Lax–Liu [29,53] Riemann problem #5 (2DRP05), obtained with the RORWENOM5, the RORWENOM11, and the RORWENOM17 schemes, using SSPRK(3,3) time-integration [23] with CFL $= 0.6$, on 4 different grids ($N_x \times N_y = 101 \times 101, 201 \times 201, 401 \times 401, 801 \times 801$).

$t_{\text{END}} = 0.23$ (Fig. 18). The corresponding selfsimilar solution only involves contact discontinuities and waves created by their interactions [50–52,29,53]. The flow features can be observed in the best-resolved simulation (RORWENOM17, grid $N_x \times N_y = 801 \times 801$; Fig. 18), which is in perfect agreement with previous results [52,29,53]. The sliplines in quadrant 4 (SE) move away from the sliplines of quadrant 2 (NW). Sliplines [29] $\text{J}_{\text{WNE}} \equiv \text{J}_{21}^{-}$ and $\text{J}_{\text{NWS}} \equiv \text{J}_{32}^{-}$ in quadrant 2 (NW) (respectively, $\text{J}_{\text{NES}} \equiv \text{J}_{41}^{-}$ and $\text{J}_{\text{WSE}} \equiv \text{J}_{34}^{-}$ in quadrant 4 (SE)) roll up at their intersection to form a vortical structure (Fig. 18). The prolongation of slipline $\text{J}_{\text{NWS}} \equiv \text{J}_{32}^{-}$ (respectively, $\text{J}_{\text{NES}} \equiv \text{J}_{41}^{-}$) towards the axis $x = 0$ breaks down to produce vortices [52,29,53]. The central region between the sliplines which have moved away toward the corners of the computational domain is delimited by 2 shockwaves moving toward the NE and SW corners (Fig. 18). In the absence of physical viscosity in the 2-D Euler equations model (50) there exists no physical lengthscale [5,31] for this selfsimilar problem [52], and the number of vortices produced will depend on resolution (order of the scheme and cell-size). Lax and Liu [29]conjecture that "*as the calculations are refined the number of vortices might well tend to infinity*".

On the coarsest $N_x \times N_y = 101 \times 101$ grid the RORWENOM17 ($r = 9$) scheme produces thinner sliplines and resolves better their rolling up than the lower-order schemes (Fig. 18). As the grid is progressively refined the rolling up of the sliplines is better resolved, and their numerical smearing diminishes (Fig. 18). On the $N_x \times N_y = 401 \times 401$ grid the RORWENOM17 ($r = 9$) scheme predicts vortices resulting from the breakdown of the sliplines, which are not yet resolved by the lower-order schemes on this grid (Fig. 18). On the finer $N_x \times N_y = 801 \times 801$ grid the RORWENOM17 ($r = 9$) scheme predicts 2–3 vortices for each breakdown (in quadrants 2 and 4), whereas the RORWENOM5 ($r = 3$) scheme only resolves 1 vortex in each quadrant (2 and 4), having resolution similar to that of the RORWENOM17 ($r = 9$) scheme on the twice coarser in each direction $N_x \times N_y = 401 \times 401$ grid (Fig. 18). Systematically, the RORWENOM11 ($r = 6$) scheme, on any given grid, has resolution intermediate between the RORWENOM5 ($r = 3$) and the RORWENOM17 ($r = 9$) schemes (Fig. 18). All of the schemes predict perfectly resolved ENO shockwaves (Fig. 18).

8.3.3. Woodward–Colella double-Mach-reflection of a strong shockwave

This test-case, introduced by Woodward and Colella [26], solves the 2-D Euler equations in the domain $x \in [0,4],\ y \in [0,1]$, with ICS corresponding to a M_{SW}=10 shockwave, inclined at 60° with respect to the x-axis, and propagating to the right, against a region of still air (state $\underline{v}_{\text{B}}$),

$$\underline{v}(x,y,t=0) = \underline{v}_0(x,y) = \begin{cases} \underline{v}_{\text{A}} := \left[8, 8.25\cos\frac{\pi}{6}, -8.25\sin\frac{\pi}{6}, 116.5\right]^{\text{T}} & x \leqslant \frac{1}{6} + \frac{y}{\tan\frac{\pi}{3}} \\ \underline{v}_{\text{B}} := [1.4, 0, 0, 1]^{\text{T}} & x > \frac{1}{6} + \frac{y}{\tan\frac{\pi}{3}} \end{cases} \tag{60}$$

where $\underline{v}_{\text{A}}$ corresponds to the state trailing behind the right-moving shockwave. The boundary-conditions correspond to the exact shockwave motion at the upper boundary ($y = 1$), fixed state $\underline{v}_{\text{B}}$ at inflow and in the region $0 \leqslant x \leqslant \frac{1}{6}$ on the lower boundary ($y = 0$), continued by a reflecting wall $\left(x > \frac{1}{6}\right)$

$$\underline{v}(x=0,y,t) = \underline{v}_{\text{A}} \quad \forall t,y \tag{61a}$$
$$\underline{v}(0 \leqslant x \leqslant x_{\text{SW}_u}(t), y=1, t) = \underline{v}_{\text{A}} \quad \forall t \tag{61b}$$
$$\underline{v}(x_{\text{SW}_u}(t) < x \leqslant 4, y=1, t) = \underline{v}_{\text{B}} \quad \forall t \tag{61c}$$
$$\underline{v}\left(0 \leqslant x \leqslant \frac{1}{6}, y=0, t\right) = \underline{v}_{\text{A}} \quad \forall t \tag{61d}$$
$$\partial_x \underline{v}(x=4,y,t) = 0 \quad \forall t,y \tag{61e}$$
$$\begin{bmatrix} \partial_y \rho \\ \partial_y u \\ v \\ \partial_y p \end{bmatrix} \left(\frac{1}{6} < x \leqslant 4,\ y=0,t\right) = \begin{bmatrix} 0 \\ 0 \\ 0 \\ 0 \end{bmatrix} \quad \forall t \tag{61f}$$

where

$$x_{\text{SW}_u}(t) = \frac{1}{6} + \frac{1}{\tan\frac{\pi}{3}} + \text{S}_{\text{SW}_x} t; \quad \text{S}_{\text{SW}_x} = \frac{\text{S}_{\text{SW}}}{\sin\frac{\pi}{3}}; \quad \text{S}_{\text{SW}} = 10 \tag{61g}$$

is the instantaneous shockwave location on the upper boundary ($y = 1$).

The Woodward–Colella [26] double-Mach-reflection test-case was computed with the RORWENOM5 ($r = 3$), the RORWENOM11 ($r = 6$), and the RORWENOM17 ($r = 9$) schemes, using SSPRK(3,3) at CFL $= 0.6$, on progressively finer grids ($N_x \times N_y = 241 \times 61$, $481 \times 121, 961 \times 241, 1921 \times 481$ points), up to $t_{\text{END}} = 0.20$ (Figs. 19 and 20). This test-case is widely used to evaluate the performance of numerical schemes [26,2,54,45,3,55,5], and is described in detail by Woodward–Colella [26]. The curved reflected shockwave attached at $(x,y) = \left(\frac{1}{6}, 0\right)$ is moving rapidly at its right end, where is observed the region of double Mach reflection [26], with 2 Mach stems and 2 contact discontinuities ($x \in [2, 2.8]$; Fig. 19), and a wall-jet forming very near the wall, below the contact discontinuity. In the absence of physical viscosity in the 2-D Euler equations model (50), the physically unstable features of the flow (sliplines and wall-jet) will exhibit more instability (wavyness, rolling up, vortices, etc.) with increasing resolution [5]. It is generally accepted [26,2,54,45,3,55,5] that the prediction of such unstable structures is a measure of increased resolution of the scheme for the convective (Euler) part of the flow equations.

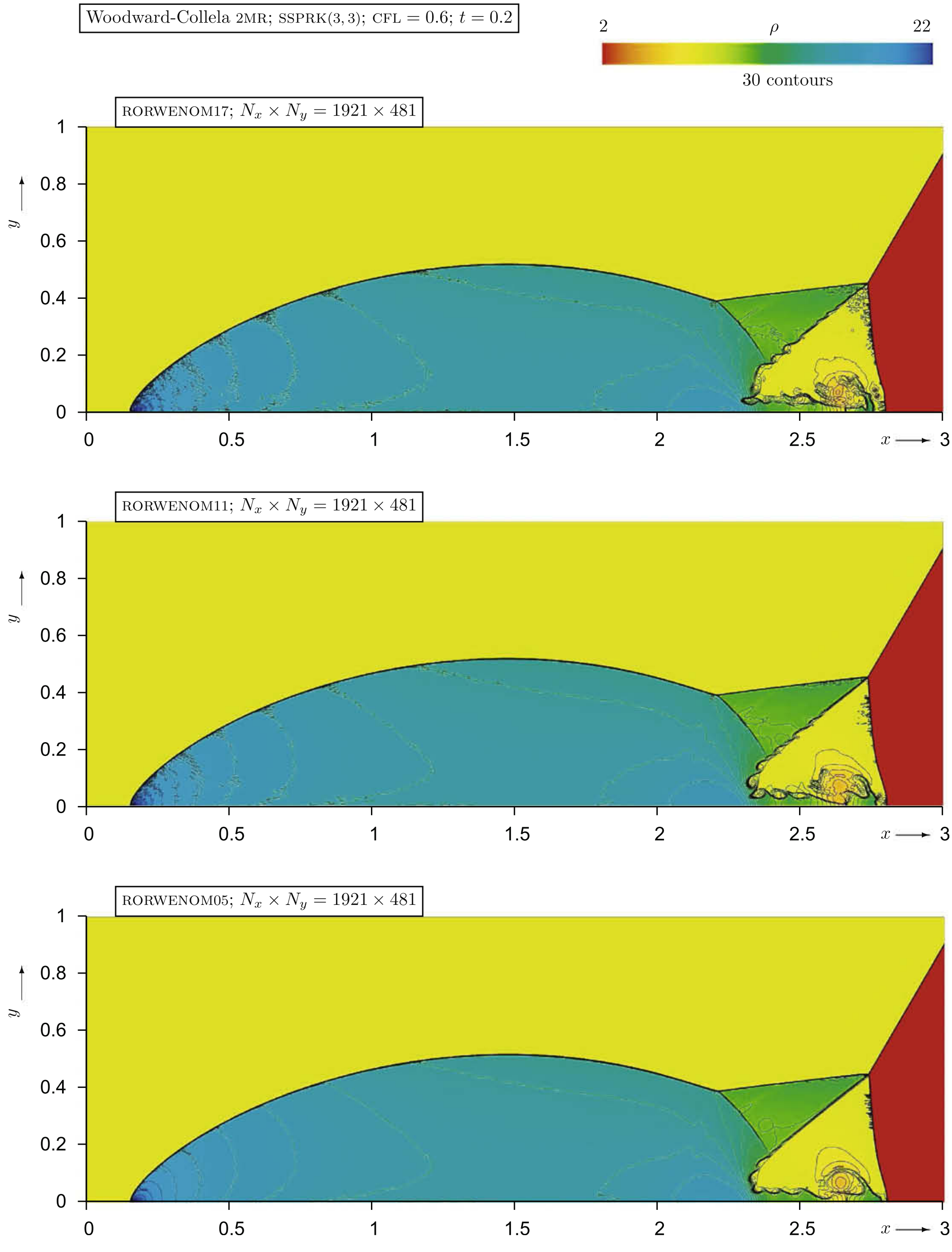

Fig. 19. Comparison, at $t = 0.2$, of the numerical solution of the 2-D Euler equations, for the Woodward–Colella double Mach-reflection (2MR) problem [26], obtained with the RORWENOM5, the RORWENOM11, and the RORWENOM17 schemes, using SSPRK(3,3) time-integration [23] with CFL $= 0.6$ ($N_x \times N_y = 1961 \times 481$; zoom in the region $x \in [0, 3]$).

On the coarsest $N_x \times N_y = 241 \times 61$ grid there is little difference in the basic flow structure predicted by the 3 schemes (Fig. 20), although the RORWENOM17 ($r = 9$) scheme introduces less numerical smearing of the contact discontinuities compared to the RORWENOM5 ($r = 3$) scheme (Fig. 20). On the $N_x \times N_y = 481 \times 121$ grid the RORWENOM17 ($r = 9$) scheme better predicts the vortical structure near the wall at $x \approxeq 2.65$, and on the $N_x \times N_y = 961 \times 241$ grid it already predicts the wavy instability of both sliplines, a clearly formed vortical structure at $x \approxeq 2.65$, and a small vortex at the end of the wall-jet near

As the vortices at the end of the wall-jet ($x \approxeq 2.75$) are better resolved these structures move upward, and they will probably, with further grid refinement, prove to be vortices associated with the wavyness of the slipline at $(x, y) \approxeq (2.75, 0.45)$ (Fig. 20).

9. Conclusions

In this paper we extended (Section 2) the family of WENO$(2r-1)$ schemes [2,3] up to WENO17 ($r = 9$), and tabulated (Tables 1–6) the coefficients of the WENO13 ($r = 7$), WENO15 ($r = 8$), and WENO17 ($r = 9$) schemes, which can also be used with the mapping procedure [4] of the nonlinear weights (WENOM$(2r-1)$ schemes).

The family of WENO$(2r-1)$ and WENOM$(2r-1)$ schemes ($r \in [3, 9]$) was investigated (Section 3) by numerically solving the 1-D linear advection equation with periodic BCs [2], using ℓSSPRK$(2r, 2r-1)$ time-integration [39] of the same order ($O(\Delta t^{2r-1})$ for linear problems), with CFL $\in [0.8, 1]$. Studies on the advection of a square wave with CFL $= 0.8$ (Section 3.3) indicate that the value of the exponent p_β in the definition of the Jiang–Shu [2] nonlinear weights has to be increased from the value $p_\beta = 2$ [2] to a value $p_\beta(r) \in [2, r]$, to obtain ENO results, as r increases. The optimal (minimal ENO) value $p_\beta(r) \in [2, r]$ may be different for the WENO$(2r-1)$ and the WENOM$(2r-1)$ schemes, and is the subject of on-going research. Numerical studies for the advection of different smooth waves at CFL $= 1$ (Section 3.4) were presented verifying that the WENOM$(2r-1)$ schemes approach the UW$(2r-1)$, asymptotically, as $\Delta x \to 0$. Results on the loss of accuracy at critical points, for the WENO$(2r-1)$ and the WENOM$(2r-1)$ schemes (Section 3.4), on the now wider range of $r \in [3, 9]$, suggest that the behaviour of the schemes with r odd or even may be different, a conjecture also supported by results obtained (Section 2.3.6) for the Taylor-expansions of the smoothness indicators. Further studies on the full asymptotic expansions of the WENO$(2r-1)$ and the WENOM$(2r-1)$ schemes are necessary to clarify this point. Computational studies of the advection of the Jiang–Shu wave [2] at CFL $= 0.8$ (Section 3.4.3) confirm the increased resolution of the WENOM$(2r-1)$ schemes with increasing r, and their ENO behaviour for $p_\beta = r$. A study (Section 4) of a test-problem for the 1-D Burgers equation with periodic BCs, using SSPRK$(8, 3)$ time-integration [40] with CFL $= 1$, suggests that the results obtained for the linear advection equation (Section 3) are applicable to nonlinear scalar hyperbolic conservation laws, although further testing, including other test-cases, as well as other hyperbolic conservation laws with nonconvex fluxes, would be useful at substantiating this proposition.

Then (Section 5.1) we studied the extension of the family of very-high-order WENOM$(2r-1)$ schemes, with $p_\beta = r$, to the Euler equations of gasdynamics (system of hyperbolic conservation laws), using local characteristic reconstruction (scalar reconstruction of the local characteristic fields [12]). Straightforward application of the local characteristic reconstruction (results not shown) fails to give ENO results, as r increases. Evenmore, at fixed r, as $\Delta x \to 0$ (increasing number of gridpoints N_x), the oscillations, associated with the nonlinear interaction between characteristic fields and the potential absence of a wide enough (large r) smooth stencil in the WENO reconstruction, grow, contaminating the solution. A way to circumvent this problem is to recursively reduce the order r of the reconstruction, at interfaces where a reconstruction-failure is detected [5]. In the present paper we introduced a new reconstruction-failure criterion, free of any adjustable parameters, and applied it in the construction of a RORWENOM$(2r-1)$ family of reconstructions for the Euler equations. Systematic numerical tests, on progressively refined grids, using SSPRK$(3, 3)$ time-integration [23] with CFL $= 0.6$ were run (Section 5.8) for standard Riemann problems [24,25], shock-wave/entropy interactions [27,5,10], and IBWS [26]. The results demonstrated the increase in accuracy with increasing reconstruction-order r (indicating that the ROR procedure is indeed local, at discontinuities, and does not unduly reduce accuracy at smooth points), and showed that the RORWENOM$(2r-1)$ local characteristic reconstruction applied to the Euler equations is ENO, not only on coarse grids but even as $\Delta x \to 0$ (N_x increases), for $r \in [3, 9]$.

A baseline linewise extension of the schemes to 2-D (Section 6) was implemented to test both accuracy and nonoscillatory performance for multidimensional problems. Accuracy tests with the 2-D advection equation (Section 7.3) suggest that the unsplit linewise extension of the schemes to 2-D has the same behaviour concerning accuracy and rate-of-convergence as the one observed for the corresponding 1-D cases (Section 3.4). Tests (Section 7.4) using different time-integration techniques demonstrate the importance of very-high-order time-discretizations in achieving high rates-of-convergence with grid refinement. Finally, tests (Section 8.3) with the unsplit linewise extension of the schemes to the 2-D Euler equations, for the advection of a smooth vortex [28], a 2-D Riemann problem [29] and the double-Mach-reflection of a strong shock-wave [26], substantiate the conclusions of the 1-D test-cases (Section 5.8), that the very-high-order RORWENOM$(2r-1)$ schemes improve resolution with increasing r while remaining nonoscillatory.

Acknowledgments

Part of the present work was conducted within the EU-funded research project ProBand (STREP-FP6 AST4-CT-2005-012222). Computer resources were made available by IDRIS–CNRS (http://www.idris.fr). The authors are listed alphabetically.

All the computer programs developed and used in the present work are open source and can be found at http://aerodynamics.sourceforge.net. The package includes all the reconstruction routines (in f90 language), and their application to the various test-cases.

References

[1] X.D. Liu, S. Osher, T. Chan, Weighted essentially nonoscillatory schemes, J. Comput. Phys. 115 (1994) 200–212.
[2] G.S. Jiang, C.W. Shu, Efficient implementation of weighted ENO schemes, J. Comput. Phys. 126 (1996) 202–228.

[3] D.S. Balsara, C.W. Shu, Monotonicity prserving WENO schemes with increasingly high-order of accuracy, J. Comput. Phys. 160 (2000) 405–452.
[4] A.K. Henrick, T.D. Aslam, J.M. Powers, Mapped weighted-essentially-non-oscillatory schemes: achieving optimal order near critical points, J. Comput. Phys. 207 (2005) 542–567.
[5] V.A. Titarev, E.F. Toro, Finite-volume WENO schemes for 3-D conservation laws, J. Comput. Phys. 201 (2004) 238–260.
[6] E.F. Toro, V. Titarev, MUSTA fluxes for systems of conservation laws, J. Comput. Phys. 216 (2006) 403–429.
[7] R. Borges, M. Carmona, B. Costa, W.S. Don, An improved WENO scheme for hyperbolic conservation laws, J. Comput. Phys. 227 (2008) 3191–3211.
[8] S. Pirozzoli, Conservative hybrid compact-WENO schemes for shock–turbulence interaction, J. Comput. Phys. 178 (2002) 81–117.
[9] D. Ponziani, S. Pirozzoli, F. Grasso, Development of optimized WENO schemes for multiscale compressible flows, Int. J. Numer. Method Fluid 42 (2003) 953–977.
[10] M.P. Martín, E.M. Taylor, M. Wu, V.G. Weirs, A bandwidth-optimized WENO scheme for effective direct numerical simulation of compressible turbulence, J. Comput. Phys. 220 (2006) 270–289.
[11] E.M. Taylor, M. Wu, M.P. Martín, Optimization of nonlinear error for weighted essentially non-oscillatory methods in direct numerical simulations of compressible turbulence, J. Comput. Phys. 223 (2007) 384–397.
[12] A. Harten, B. Engquist, S. Osher, S.R. Chakravarthy, Uniformly high-order accurate essentially nonoscillatory schemes III, J. Comput. Phys. 71 (1987) 231–303.
[13] E. Johnsen, T. Colonius, Implementation of WENO schemes in compressible multicomponent flow problems, J. Comput. Phys. 219 (2006) 715–732.
[14] A. Suresh, H.T. Huynh, Accurate monotonicity-preserving schemes with Runge–Kutta time stepping, J. Comput. Phys. 136 (1997) 83–99.
[15] J. Qiu, C. Shu, Hermite WENO schemes and their application as limiters for Runge–Kutta discontinuous Galerkin method: 1-D case, J. Comput. Phys. 193 (2003) 115–135.
[16] J. Qiu, C. Shu, Hermite WENO schemes and their application as limiters for Runge–Kutta discontinuous Galerkin method II: 2-D case, Comput. Fluid 34 (2005) 642–663.
[17] G. Capdeville, A hermite upwind WENO scheme for solving hyperbolic conservation laws, J. Comput. Phys. 227 (2008) 2430–2454.
[18] G. Capdeville, Towards a compact high-order method for nonlinear hyperbolic systems – II: The Hermite HLLC scheme, J. Comput. Phys. 227 (2008) 9428–9462.
[19] E.F. Toro, V. Titarev, ADER schemes for scalar nonlinear hyperbolic conservation laws with source-terms in 3D, J. Comput. Phys. 202 (2005) 196–215.
[20] V.A. Titarev, E.F. Toro, ADER schemes for 3D nonlinear hyperbolic systems, J. Comput. Phys. 204 (2005) 715–736.
[21] E.F. Toro, V. Titarev, Derivative Riemann solvers for systems of conservation laws and ADER methods, J. Comput. Phys. 212 (2006) 150–165.
[22] A. Harten, S. Osher, Uniformly high-order accurate nonoscillatory schemes I, SIAM J. Numer. Anal. 24 (1987) 279–309.
[23] C.W. Shu, S. Osher, Efficient implementation of essentially nonoscillatory shock-capturing schemes, J. Comput. Phys. 77 (1988) 439–471.
[24] P.D. Lax, Weak solutions of nonlinear hyperbolic equations and their numerical computation, Commun. Pure Appl. Math. 7 (1954) 159–193.
[25] G.A. Sod, A survey of several finite difference methods for systems of nonlinear hyperbolic conservation laws, J. Comput. Phys. 27 (1978) 1–31.
[26] P. Woodward, P. Colella, The numerical simulation of 2-D fluid flow with strong shocks, J. Comput. Phys. 54 (1984) 115–173.
[27] C.W. Shu, S. Osher, Efficient implementation of essentially nonoscillatory shock-capturing schemes II, J. Comput. Phys. 83 (1989) 32–78.
[28] C.W. Shu, ENO and WENO schemes for hyperbolic conservation laws, in: B. Cockburn, C. Johnson, C.W. Shu, E. Tadmor (Eds.), Advanced Numerical Approximation of Nonlinear Hyperbolic Equations, Lecture Notes in Mathematics, vol. 1697, Springer, Berlin [DEU], 1998, pp. 325–432 (also NASA CR-97-206253 and ICASE-97-65 Rep., NASA Langley Research Center, Hampton [VA, USA]).
[29] P.D. Lax, X.D. Liu, Solution of 2-D Riemann problems of gas dynamics by positive schemes, SIAM J. Sci. Comput. 19 (1998) 319–340.
[30] V.A. Zorich, Mathematical Analysis II, Springer, Heidelberg [DEU], 2004.
[31] G.A. Gerolymos, D. Sénéchal, I. Vallet, Performance of very-high-order upwind schemes for DNS of compressible wall-turbulence, Int. J. Numer. Method Fluid, in press, doi:10.1002/fld.2096. Available online 2 July 2009.
[32] B. Van Leer, Upwind and high-resolution methods for compressible flow: from donor cell to residual distribution schemes, Commun. Comput. Phys. 1 (2) (2006) 192–206 (also AIAA Paper 2003-3559).
[33] B. Van Leer, Towards the ultimate conservative difference scheme – V – a 2-order sequel to Godunov's method, J. Comput. Phys. 32 (1979) 101–136.
[34] MAXIMA, A Computer Algebra System. <http://maxima.sourceforge.net>.
[35] G.A. Gerolymos, J.P. Bréus, Computation of unsteady nozzle flow resulting from fluctuating back-pressure using Euler equations, Aerosp. Sci. Technol. 2 (2) (1998) 91–105.
[36] J.C. Butcher, General linear methods, Acta Numer. 15 (2006) 157–256.
[37] S. Gottlieb, C.W. Shu, E. Tadmor, Strong stability preserving high-order time discretization methods, SIAM Rev. 43 (1) (2001) 89–112.
[38] S. Gottlieb, L.A.J. Gottlieb, Strong stability preserving properties of Runge–Kutta time discretization methods for linear constant coefficient operators, J. Sci. Comput. 18 (1) (2003) 83–109.
[39] S. Gottlieb, On high order strong stability preserving Runge–Kutta and multistep time discretizations, J. Sci. Comput. 25 (1) (2005) 105–128.
[40] S.J. Ruuth, Global optimization of explicit strong-stability-preserving Runge–Kutta methods, Math. Comput. 75 (223) (2005) 183–207.
[41] M.L. Overton, Numerical Computing with IEEE Floating Point Arithmetic, SIAM, Philadelphia, PA, USA.
[42] R. Courant, K.O. Friedrichs, Supersonic Flow and Shock-Waves, Springer, New York, NY, USA, 1948 (corrected 5, printing 1999 edition).
[43] E.F. Toro, Riemann Solvers and Numerical Methods for Fluid Dynamics, Springer-Verlag, Berlin [D], 1997.
[44] P.L. Roe, Approximate Riemann solvers, parameter vectors, and difference schemes, J. Comput. Phys. 43 (1981) 357–372.
[45] C. Hu, C.W. Shu, Weighted essentially nonoscillatory schemes on triangular meshes, J. Comput. Phys. 150 (1999) 97–127.
[46] Y.T. Zhang, C.W. Shu, WENO3 scheme for 3-D tetrahedral meshes, Commun. Comput. Phys. 5 (2009) 836–848.
[47] M. Dumbser, D.S. Balsara, E.F. Toro, C.D. Munz, A unified fremework for the construction of 1-step finite-volume and discontinuous Galerkin schemes on unstructured meshes, J. Comput. Phys. 227 (2008) 8209–8253.
[48] A. Rohde, Eigenvalues and Eigenvectors of the Euler Equations in General Geometries, AIAA Paper 2001-2609, 2001.
[49] C.W. Shu, TVB uniformly high-order schemes for conservation laws, Math. Comput. 29 (1987) 105–121.
[50] T. Zhang, Y. Zheng, Conjecture on the structure of the solutions of the Riemann problem for 2-D gas dynamics systems, SIAM J. Math. Anal. 21 (3) (1990) 593–630.
[51] C.W. Schulz-Rinne, Classification of the Riemann problem for 2-D gas dynamics, SIAM J. Math. Anal. 24 (1) (1993) 76–88.
[52] C.W. Schulz-Rinne, J.P. Collins, H.M. Glaz, Numerical solution of the Riemann problem for 2-D gas dynamics, SIAM J. Sci. Comput. 14 (6) (1993) 1394–1414.
[53] A. Kurganov, E. Tadmor, Solution of 2-D Riemann problems of gas dynamics without Riemann solvers, Numer. Method Part. Diff. Eq. 18 (2002) 584–608.
[54] B. Cockburn, C.W. Shu, The Runge–Kutta discontinuous Galerkin method for conservation laws – V, J. Comput. Phys. 141 (1998) 199–224.
[55] J. Shi, C. Hu, C.W. Shu, A technique for treating negative weights in WENO schemes, J. Comput. Phys. 175 (2002) 108–127.